学 位 論 文

Thermal and Chemical Evolution of a Crustal Magma Chamber:

Constraints from Differential Information on Erupted Materials

マグマ溜まりの熱物質進化：火山噴出物からの微分的情報による制約

平成１１年　１２月博士（理学）申請

東京大学大学院理学系研究科
地質学専攻

栗谷　豪

Thermal and Chemical Evolution of a Crustal Magma Chamber:

Constraints from Differential Information on Erupted Materials

Geological Institute of the University of Tokyo

Takeshi Kuritani

March 2000

Abstract

Detailed investigation of an erupted magma with limited compositional diversity provides instantaneous differential information on magmatic processes in an evolving magma chamber. Kutsugata lava and Tanetomi lava, suitable targets of such study, is a Quaternary alkali basalt and a trachytic andesite, erupted sequentially from the same magma reservoir beneath Rishiri Volcano, northern Japan. The Kutsugata lava consists of North lava (51.3-51.9 wt.% in SiO_2) and South lava (52.1-53.2 wt.%), and the Tanetomi lava is composed of Lower lava (58.4-59.8 wt.%) and Upper lava (59.9-65.1 wt.%). Chemical and modal compositions of mineral phases crystallized in the magma chamber vary systematically with the whole-rock composition.

Throughout the Kutsugata lava, plagioclase crystals with extremely An-rich composition are present. They are too calcic to have crystallized from a liquid represented by any whole-rock composition at the estimated temperature of the Kutsugata magma system. The An-rich plagioclase is inferred to have formed in a mushy boundary layer along the wall of the magma chamber, where the magma was cool and rich in dissolved water because of significant olivine fractionation and addition of water expelled from the solidifying margin. In contrast to the Kutsugata lava, Ab-rich plagioclase, which is too sodic to have crystallized from the magma with the observed whole-rock composition, occurs as crystal aggregate with hornblende and titanomagnetite in the Tanetomi lava. The crystal aggregate is also considered to have derived from the crystal mush, where Ca content was depleted and the dissolved water could no longer suppress the crystallization of plagioclase with Ab-rich composition. Throughout the evolution from the Kutsugata magma to the Tanetomi magma, crystallizations were restricted to the boundary layers and the main magma was mostly free from crystals.

Chemical compositions of fractionated mineral phases during differentiation of the Kutsugata and Tanetomi magmas are estimated by utilizing the whole-rock composition trends. The estimated chemical compositions of separated crystals coincide with the observed compositions of the crystals derived from the mush zone in both lavas. This indicates that these magmas differentiated by the crystal-melt separation occurred in the mushy boundary layer. Most plausible mechanism is an extraction of a fractionated interstitial melt from the mush zone and its subsequent mixing with the main magma. The average temperature of the extracted melt was 1010 °C for the North lava and 920 °C for the Upper lava, significantly lower than the estimated temperature for the main magma of 1100 °C and 950 °C, respectively. Crustal materials assimilated to the magma chamber simultaneously with boundary layer fractionation. Though the assimilation significantly affected the concentration of trace elements and isotopic compositions of Pb and Sr during magmatic evolution, it was negligible for the variation of the major elements.

A quantitative model of magmatic differentiation, which includes thermal and compositional evolution of a basaltic magma chamber, is constructed. The model utilizes a multicomponent thermodynamic approach for relating the compositional structure with the thermal structure in a cooling magma body. The magma composition evolves by transportation of a fractionated interstitial melt from the mushy boundary layer. The model can successfully reproduce the observed composition trends of the North lava. By comparison of the estimated temperature and major element concentration of the Kutsugata lava with those calculated, the magma is suggested to have cooled principally by heat conduction without vigorous thermal convection. The primary magma composition of the Kutsugata lava is determined by utilizing the model with the constraints of the concentration of trace elements. The estimated composition is significantly different from that estimated by common procedure of olivine addition. This can cause significant errors in estimating the conditions at which the primary magma was generated.

Contents

1. Introduction

Volcanic rocks provide important information for constraining the possible evolution of the Earth, such as a large-scale fractionation and material recycling, because they could possess physicochemical information of the Earth's interior. Magmas generated in the mantle evolve in temperature and chemical composition during ascent to the Earth's surface. A crustal magma chamber is the most principal site for the magmatic evolution, and the information of the mantle source composition could be modified easily there. It is not easy to restore the primary information by evaluating the modification during residence in the magma chamber, because thermal and chemical evolution of magmas is controlled by complex density instability within the cooling magma and interaction with the surrounding crust. Therefore, quantitative understandings of magmatic processes in the crustal magma chamber are inevitable to extract precise information of the Earth's interior from erupted materials.

In the magma chamber, the magma is cooled from the surrounding crust and a mushy boundary layer is formed along the chamber walls, where the temperature is below the liquidus of the main magma (e.g., *Marsh*, 1996). Because of the density contrast among crystals, interstitial melt, and main magma, separation of residual melt from the mush zone may occur. Hence, the role of the mushy boundary layer in chemical differentiation of magma in magma reservoirs has received much attention and has been studied petrologically, theoretically, and experimentally (*Jaupart and Tait*, 1995). Previous geological information indicating how magmatic differentiation takes place by boundary-layer processes has been mainly extracted from large igneous complexes, sills, and lava lakes (*Shirley*, 1987; *Helz et al.*, 1989; *McBirney*, 1995), because they represent magma chambers that we can directly access. Petrological, geochemical, and thermal data on these intrusions have provided essential constraints on the possible model of magmatic evolution. However, the gap between field observation and theoretical models still remains large. This is partly because theoretical and experimental models are mostly restricted to simple systems due to lack of constraints concerning physical properties of multicomponent silicate melts. It is also partly because the igneous intrusions provide only integrated information about processes that occur during a long solidification time (Fig. 1-1), and liquid-state differentiation could not be inferred with high-level resolution. To remedy this drawback, investigations on erupted volcanic rocks are necessary because they are believed to have recorded instantaneous information on magmatic evolution (*Tait*, 1988).

In this paper, Kutsugata lava (alkali basalt; 51.3~53.2 wt.% in SiO_2) and Tanetomi lava (trachytic andesite; 58.4~65.1 wt.% in SiO_2), which erupted mostly contemporaneously from Rishiri Volcano, are studied. Both the Kutsugata and the Tanetomi lavas are divided into several flow units with limited compositional diversity. Thus detailed study of each unit provides a differential information on magmatic evolution, and integration of such information enables to elucidate the magmatic processes from basaltic to dacitic composition (Fig. 1-1).

For the Kutsugata lava (Chapter 2) and Tanetomi lava (Chapter 3), the origin of the crystals are examined by detailed analyses of phenocrysts with the constraints of thermodynamics, and the both lavas are shown to have sampled crystals derived from the mushy boundary layer as well as those grown in the main magma chamber. Crystal fractionation mechanism is investigated by utilizing the compositional trends, and it is demonstrated that extraction of the fractionated interstitial melt from the mush zone and its mixing with the main magma (boundary layer fractionation) played dominant role for the evolution of the magmas. Assimilation from the surrounding crust is also examined from the variations of isotopic composition and concentrations of incompatible trace elements.

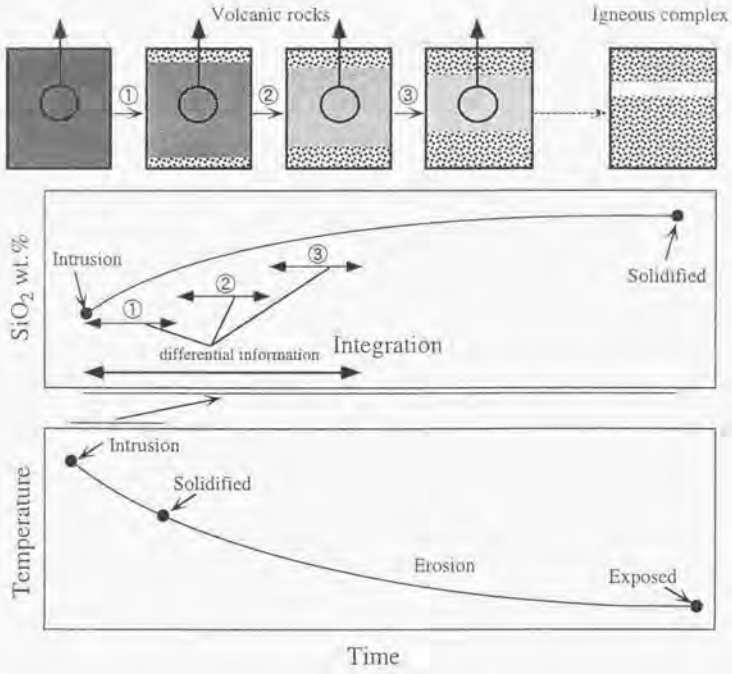

Figure 1-1. Schematic illustration of the concept of this study. Cartoon of an evolving magma chamber, evolution of the SiO_2 content of the main magma, and evolution of the temperature are shown. In this study, magmatic evolution is elucidated by integration of several differential information obtained individually from the investigations on materials with limited compositional diversity, erupted sequentially from the same magma reservoir. This is in contrast to investigations on igneous intrusions which provide only integrated information of many complex processes during solidification.

On the basis of the information obtained from the Kutsugata and Tanetomi lavas, a quantitative model of magmatic differentiation, taking account of mass and heat transport in evolving boundary, is constructed. The model is applied to the estimation of the primary magma composition of the Kutsugata lava, and it is demonstrated that elucidation of magma-chamber process is crucial to extract precise information of the Earth' interior from volcanic rocks. A role of thermal convection on the cooling of a magma body, which has been one of the most important petrological problems, is also discussed for the Kutsugata magma.

Finally, it is shown that the magmatic differentiation in a cooling magma chamber may be generalized on the basis of the concept of boundary layer fractionation. For hydrous and anhydrous basaltic magmas, efficiency of the boundary layer fractionation is discussed and possible features of their magmatic evolution are suggested.

2. Constraints from the Kutsugata Lava

The Kutsugata lava shows limited compositional diversity, but modal and chemical compositions vary systematically with the whole-rock composition. On the basis of the detailed petrological approach, evidence for boundary layer crystallization in a basaltic magma chamber is presented. Then it is discussed that how compositional variation of the lava was produced through development of the mushy boundary layer. Differential information obtained from the Kutsugata lava could constrain the possible mechanism of boundary layer fractionation. The lava is porphyritic with total phenocryst content of more than 30 vol.%, but most phenocryst is shown to have crystallized during magma ascent to the surface.

2-1. Geologic Setting

2-1-1. Rishiri Volcano

Rishiri is an island stratovolcano located to the west of Hokkaido, northern Japan (Fig. 2-1). It is a Quaternary volcano belonging to the Kurile arc and is characterized by the coexistence of alkali basalt and calc-alkaline andesite (*Kobayashi*, 1987). Previous geological and petrographical studies on Rishiri Volcano include those by *Abe* (1934), *Katsui* (1953), *Matsui et al.* (1967), *Kobayashi* (1987), *Ishizuka* (1999), and *Ishizuka and Nakagawa* (1999). The simplified geologic map in Fig. 2-1 follows the volcanic stratigraphy of *Kobayashi* (1987). *Kobayashi* (1987) divided the volcanic activity into older and younger periods, which roughly correspond to the formation stage of the stratovolcano and parasitic volcanoes, respectively. The older period is subdivided into three stages by the presence of erosion hiatuses. Volcanic products of Stages 1 and 2 are lavas and pyroclastic-flow deposits of augite olivine basalt and olivine-bearing two-pyroxene andesite. K-Ar ages of 78,000~133,000 yBP were determined for the dacitic lava domes of Stage 1 (*Ishizuka and Nakagawa*, 1994). Those of Stage 3 are lava and pyroclastic-flow deposits of two-pyroxene andesite and hornblende-bearing two-pyroxene andesite. The volcanic products of this stage were dated at 42,000 yBP by *Ishizuka* (1999). The younger period is subdivided into two stages: Stages 4 and 5. Volcanic products of Stage 4 are lava flows of augite-bearing olivine basalt (Kutsugata lava) and olivine-bearing two-pyroxene hornblende andesite (Tanetomi lava), whereas those of Stage 5 are mainly lava flows of olivine augite basalt. Ages of Stages 4 and 5 were obtained by ^{14}C dating of charcoals, at 37,320 yBP and 28,230 yBP, respectively (*Miura and Takaoka*, 1993).

2-1-2. Kutsugata lava

The Kutsugata lava investigated in the present study belongs to Stage 4. It is a high Na/K alkali basalt and is overlain by lava flows of trachytic andesite without any clear hiatus (*Kobayashi*, 1987). The Kutsugata lava is widely distributed along the northwestern coast of Rishiri Island (Fig. 2-2). The location of the vent cannot be determined because the overlying trachytic andesite lava flows and fan deposits cover most part of the Kutsugata lava. The total volume of the lava flow is estimated to be about 3 km^3. Stacked flow units of the Kutsugata lava are exposed in the sea cliffs. Flow thickness ranges from 0.2 to 5 m, and no clinker is present

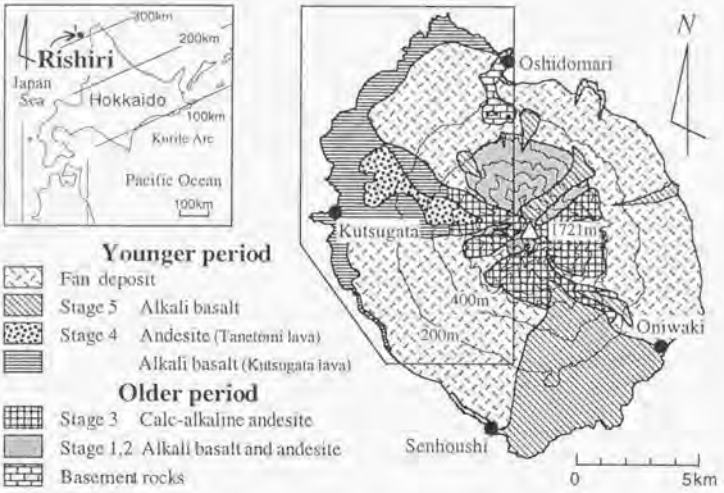

Figure 2-1. Simplified geologic map of Rishiri Volcano after *Kobayashi* (1987). The location of Fig. 2-2 is shown. Continuous lines in the index map represent depth of the Wadati-Benioff zone.

between the flow units. Pahoehoe structures and tree molds are common along the coast. Melt segregation bodies, which formed *in situ* during the consolidation process (*Yoshida et al.*, 1981), are well developed especially in thick flows. These features indicate that viscosity of the Kutsugata lava was fairly low. Pressure ridges and tumuli show that the original morphology of the lava surface is generally preserved.

The Kutsugata lava was divided petrographically into two major flows by *Abe* (1934), called North and South lavas in this paper (Fig. 2-2). As described below, his division is mostly consistent with the whole-rock chemical compositions. Although no direct contact between the North and South lavas is exposed, the boundary delineated by dense sampling is convex northward near the coast (Fig. 2-2b). The topography in the vicinity of the boundary between the North and South lavas is characterized by the gently SW-dipping surface of the North lava and by the steeply NW-dipping surface of the South lava (Fig. 2-2b). These features suggest that the South lava postdated the North lava.

2-2. Analytical Methods

Whole-rock major and trace element contents were determined by a Phillips PW-1480 XRF at the Geological Institute of the University of Tokyo. Details of the analytical method have been reported by *Kushiro* (1994). Trace element contents of seven representative samples were also analyzed by a Yokogawa PMS2000 inductively coupled plasma mass spectrometer fitted with a flow injection system at the Pheasant Memorial Laboratory (PML), Institute for Study of the Earth's Interior, Okayama University at Misasa, after the methods of *Makishima and Naka-*

mura (1997) and *Makishima et al.* (1997, 1999). B, Li, Zr, Hf were analyzed by isotopic dilution methods and other elements were analyzed by calibration curve methods. The analytical reproducibility (relative standard deviation) of trace elements is <10 %.

Isotopic compositions of Sr, Nd, and Pb were determined with a Finnigan MAT 261 instrument equipped with 5 Faraday cups using static-multi collection mode at PML. The analytical procedures for chemical separation and mass spectrometry were followed by *Yoshikawa and Nakamura* (1993) for Sr, *Shibata et al.* (1989) for Nd, and *Kuritani and Nakamura* (in preparation) for Pb. Normalizing factors for correcting isotopic fractionation are $^{86}Sr/^{88}Sr = 0.1194$ and $^{146}Nd/^{144}Nd = 0.7219$, respectively. For Pb isotope analysis, 100 ng Pb were loaded and the measured data were normalized using the recommended isotopic composition of NBS981. Measured isotopic ratios for standard materials were $^{87}Sr/^{86}Sr = 0.710240\pm20$ (2σ) for NBS987 (n=6), $^{143}Nd/^{144}Nd = 0.511853\pm09$ for La Jolla (n=4), and $^{206}Pb/^{204}Pb = 16.8839\pm17$, $^{207}Pb/^{204}Pb = 15.4187\pm23$, and $^{208}Pb/^{204}Pb = 36.4685\pm69$ for NBS981 (n=15). Analytical reproducibility for natural rock samples were 0.002 % for $^{87}Sr/^{86}Sr$, 0.002 % for $^{143}Nd/^{144}Nd$, 0.010 % for $^{206}Pb/^{204}Pb$, 0.015 % for $^{207}Pb/^{204}Pb$, and 0.019 % for $^{208}Pb/^{204}Pb$.

Mineral compositions were determined by two electron probe microanalyzers, a JEOL JCMA-733MKII and a JEOL JXA-8900L, both located at the Geological Institute of the University of Tokyo. The analytical procedures are similar to those given by *Nakamura and Kushiro* (1970) with the correction procedure of *Bence and Albee* (1968). Operating conditions were 15 kV accelerating voltage and 12 nA beam current with 10 sec counting time. MgO and FeO* (total Fe as FeO) contents of plagioclase were re-measured at 15 kV with 30 nA sample current and 30

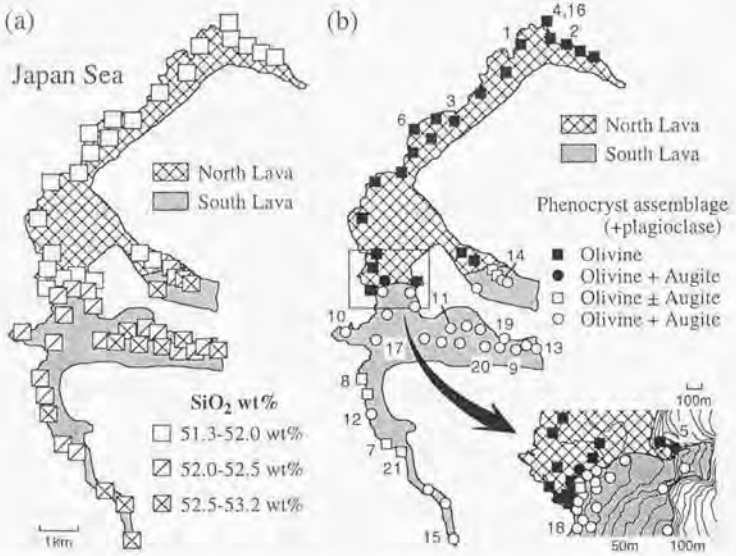

Figure 2-2. Distribution of the Kutsugata lava and representative sampling localities showing the whole-rock SiO_2 content (a) and phenocryst assemblage (b). Numbers in (b) are those listed in Table 2-1.

sec counting time for the same points as those of major-element analyses. Mg# ($100\times Mg/[Mg+Fe^{2+}]$), NiO, and CaO contents of olivine were determined at 25 kV with a 50 nA sample current and a 100 sec counting time with ZAF correction. Groundmass compositions were determined using quenched groundmass at 15 kV under 12 nA sample current and 5 sec counting time with 30 μm-broad beam, and more than 200 analyses were averaged. In map analyses, the specimen stage was automatically driven with 100-ms counting time at each point, with a 1-μm pixel size. Total amount of pixels for each map analysis ranged from 400 × 400 to 1000 × 1000.

2-3. Whole-Rock Compositions

2-3-1. Major and trace elements

Representative whole-rock major and trace element contents of the Kutsugata lava analyzed with XRF are listed in Table 2-1 for samples numbered in Fig. 2-2b. Figure 2-3 shows Harker variation diagrams for selected major element oxides (Al_2O_3, MgO, CaO, and P_2O_5) and trace elements (Cr, Ni, Sr, and Zr) plotted against SiO_2 content. Samples that were clearly affected by the segregation process after the eruption (*Yoshida et al.*, 1981) are excluded by the procedure described in the Appendix A. The Kutsugata lava is composed of two groups with a clear compositional gap (Fig. 2-3). These groups correspond with North lava (51.3~51.9 wt.% in SiO_2) and South lava (52.1~53.2 wt.%) shown in Fig. 2-2. Some of the elements plotted in Fig. 2-3 exhibit a change in slope at the gap dividing the North and South lavas. The Al_2O_3 and CaO contents are mostly constant with an increase of SiO_2 content in the North lava, but decrease in the South lava. The MgO and Ni contents decrease more significantly as the SiO_2 increases in the North lava than in the South lava.

Some composition trends among the South-lava samples exhibit a change in the slope at about 52.5 wt.% in SiO_2 (Fig. 2-3). The Al_2O_3, CaO, Cr, and Sr contents in the samples with more than 52.5 wt.% SiO_2 decrease more steeply than those with less than 52.5 wt.% as SiO_2 increases. The P_2O_5 and Zr contents are fairly constant against the SiO_2 content in the samples with less than 52.5 wt.%, but increase slightly in those with more than 52.5 wt.%. According to the inflection in the composition trends, the South lava is subdivided into South lava I (52.1–52.5 wt.%) and South lava II (52.5~53.2 wt.%). The distribution of sampling localities of the South lava I and II, which can be grouped on the map, suggests that the scale of heterogeneity of whole-rock composition in the South lava is not intra-lava flow unit, but inter-flow unit (Fig. 2-2a).

Trace element compositions of whole rocks measured with ICP-MS are listed in Table 2-2 for seven representative samples of the Kutsugata lava, and are plotted on MORB-normalized diagram in Fig. 2-4. The samples of the Kutsugata lava are enriched in highly incompatible elements compared with the N-type MORB. Significant negative Nb and Ta anomalies and positive Pb, Sr, and Li anomalies are observed. Within the compositional variation of the Kutsugata lava, the SiO_2-richer samples have higher concentrations in these trace elements.

2-3-2. Isotopic compositions

Sr, Nd, and Pb isotopic compositions of whole rocks are shown in Table 2-3 and are plotted against the SiO_2 content in Fig. 2-5. The $^{87}Sr/^{86}Sr$ ratio increases with an increase of the SiO_2 content. On the contrary, the $^{143}Nd/^{144}Nd$ ratio is mostly constant within the range of analytical reproducibility. The $^{207}Pb/^{204}Pb$ and $^{208}Pb/^{204}Pb$ ratios tend to increase with SiO_2 content, but the $^{206}Pb/^{204}Pb$ ratio is randomly scattered and is independent of the whole-rock SiO_2 content.

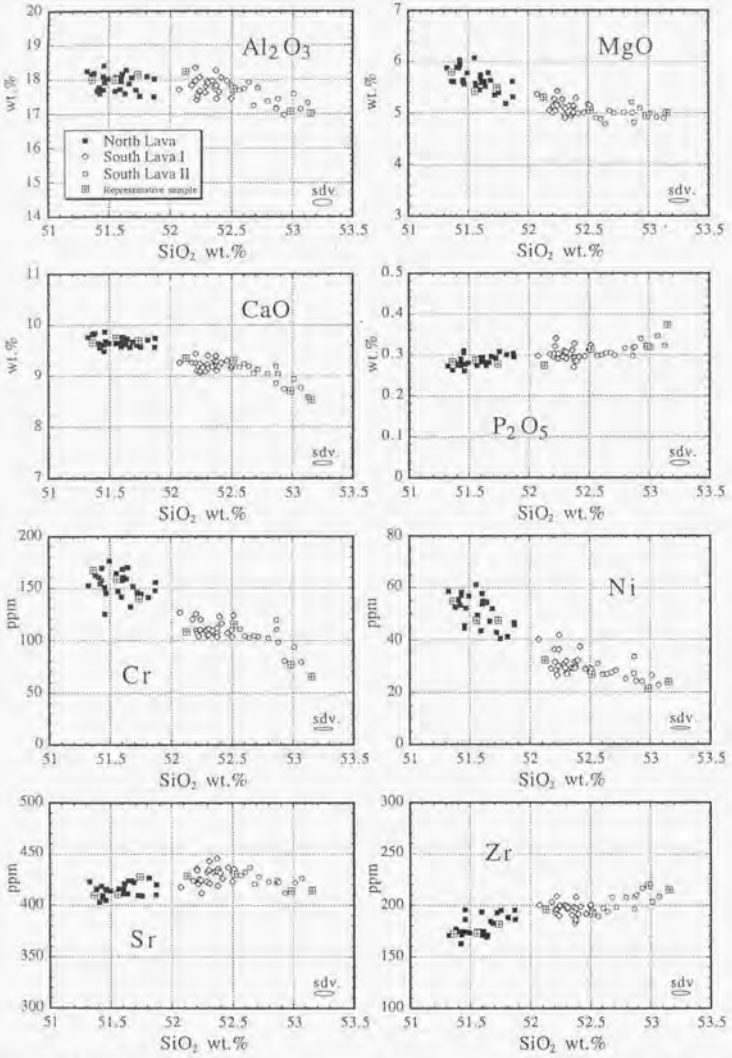

Figure 2-3. Whole-rock SiO_2 variation diagrams for some major oxides (Al_2O_3, MgO, CaO, and P_2O_5) and trace elements (Cr, Ni, Sr, and Zr) from the Kutsugata lava. Selected samples for detailed investigations are shown by different mark. Major element analyses are recalculated for total weight to be 100 %. Analytical error (1σ) for both SiO_2 and the element of the ordinate is shown by ellipse.

Table 2-1. Whole Rock Major and Trace Element Compositions of Representative Samples from the Kutsugata Lava

	North Lava						South Lava I					South Lava II			
	1	2	3	4	5	6	7	8	9	10	11	12	13	14	15
	Fm-57	Fm-17	Ku-18	Fm-15	Ta-26	Ku60	Km-8	Km-3	Kr-31	Ku-10	Kr-28	Km-9	Kr-9	Tb-8	Km-11
Whole Rock Composition, Major Elements (wt.%)															
SiO_2	50.29	50.85	50.55	50.86	51.20	50.79	51.28	51.79	51.50	51.77	52.35	51.88	52.37	51.78	52.26
TiO_2	1.30	1.34	1.44	1.37	1.31	1.38	1.41	1.29	1.39	1.39	1.39	1.36	1.47	1.39	1.48
Al_2O_3	17.86	17.81	17.38	17.74	17.97	17.64	17.44	18.11	17.55	17.77	17.65	16.85	16.87	17.18	16.72
Fe_2O_3	8.33	8.43	8.74	8.35	8.25	8.35	8.60	8.15	8.61	8.52	8.57	8.56	9.02	8.57	9.02
MnO	0.14	0.14	0.15	0.14	0.14	0.14	0.15	0.14	0.15	0.15	0.15	0.15	0.16	0.15	0.16
MgO	5.75	5.74	5.51	5.36	5.44	5.20	5.28	5.27	5.04	4.91	4.97	5.11	4.89	4.88	4.92
CaO	9.56	9.56	9.45	9.62	9.60	9.54	9.12	9.29	9.06	9.14	9.07	9.02	8.60	8.73	8.39
Na_2O	3.93	4.29	4.12	4.33	4.20	3.99	4.25	4.38	4.22	4.33	4.16	4.17	4.37	3.99	4.22
K_2O	0.54	0.57	0.59	0.60	0.57	0.59	0.65	0.67	0.66	0.72	0.71	0.75	0.77	0.70	0.77
P_2O_5	0.27	0.28	0.30	0.28	0.27	0.29	0.29	0.27	0.30	0.30	0.30	0.29	0.32	0.31	0.37
Total	97.98	99.01	98.24	98.65	98.96	97.92	98.47	99.36	98.48	98.99	99.32	98.14	98.85	97.67	98.31
Whole Rock Composition, Trace Elements (ppm)															
Ba	118	128	125	123	121	125	137	139	135	147	147	143	153	147	145
Cr	152	168	151	159	140	155	126	108	110	104	104	120	77	94	65
Nb	3.1	3.0	3.4	2.9	3.3	3.4	4.1	3.7	3.9	3.8	4.1	3.9	4.9	4.4	4.8
Ni	58	55	44	47	47	46	40	32	29	32	28	27	21	26	24
Pb	2.6	2.4	2.1	2.3	3.3	2.1	2.7	2.9	2.5	3.2	2.7	4.2	1.4	2.9	4.9
Rb	12	13	12	14	13	14	14	15	15	16	17	17	18	16	19
Sr	423	409	405	410	428	420	417	428	432	434	428	422	414	422	414
Th	1.8	2.1	3.0	2.9	3.0	2.4	2.3	3.2	2.6	2.9	3.2	3.3	3.5	3.7	3.3
Y	23	24	24	24	23	25	25	25	24	25	24	23	24	24	25
Zr	171	172	186	173	182	186	200	196	198	199	198	196	219	203	215

Sampling localities are shown in Fig. 2-2b. Fe_2O_3 is total Fe as Fe_2O_3.

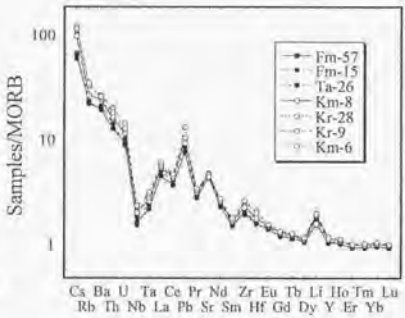

Figure 2-4. MORB-normalized trace element patterns. The trace element concentrations of the MORB are after *Sun and McDonough* (1989).

Table 2-2. Whole Rock Trace Element Composition of Representative Samples Obtained by ICP-MS

	North Lava			South Lava I		South Lava II	
	1	4	5	7	11	13	15
	Fm-57	Fm-15	Ta-26	Km-8	Kr-28	Kr-9	Km-11
	Whole Rock Composition, Trace Elements (ppm)						
Cs	0.50	0.45	0.76	0.73	0.90	0.84	0.86
Rb	13.3	14.0	13.3	16.0	20.1	19.7	20.8
Ba	132	131	141	162	170	179	175
Th	1.66	1.65	1.82	2.07	2.13	2.57	2.36
U	0.47	0.52	0.44	0.58	0.63	0.72	0.65
B	4.10	5.28	3.63	5.33	5.78	5.68	5.90
Nb	4.04	3.82	4.54	5.08	4.97	5.70	5.85
Ta	0.31	0.31	0.34	0.36	0.39	0.42	0.44
La	12.0	12.1	13.4	14.7	15.3	15.3	16.2
Ce	29.7	29.3	32.4	34.7	35.9	37.6	37.7
Pb	2.42	2.44	2.72	3.26	2.98	3.37	4.27
Pr	3.91	3.94	4.15	4.44	4.64	4.63	4.80
Sr	421	417	438	444	459	449	428
Nd	17.7	17.7	18.8	19.9	20.3	20.4	21.3
Sm	4.28	4.21	4.46	4.62	4.67	4.79	4.97
Zr	161	152	171	185	178	204	206
Hf	3.45	3.45	3.52	3.91	3.88	4.55	4.31
Eu	1.52	1.54	1.59	1.63	1.66	1.68	1.70
Gd	4.73	4.68	4.90	5.16	5.19	5.13	5.28
Tb	0.82	0.81	0.86	0.88	0.89	0.90	0.92
Dy	5.15	5.09	5.23	5.45	5.42	5.58	5.68
Li	7.04	7.62	8.29	8.72	7.24	9.10	8.93
Y	31.8	30.8	32.4	34.3	35.3	33.7	35.3
Ho	1.09	1.09	1.13	1.17	1.17	1.19	1.22
Er	2.95	2.93	2.94	3.14	3.11	3.18	3.21
Tm	0.46	0.45	0.46	0.49	0.49	0.48	0.50
Yb	3.09	3.11	3.15	3.31	3.31	3.34	3.44
Lu	0.46	0.44	0.45	0.48	0.48	0.49	0.49

Sampling localities are shown in Fig. 2-2b.

Table 2-3. Isotopic Compositions of the Representative Samples of the Kutsugata Lava

	$^{87}Sr/^{86}Sr$	$^{143}Nd/^{144}Nd$	$^{206}Pb/^{204}Pb$	$^{207}Pb/^{204}Pb$	$^{208}Pb/^{204}Pb$
Fm-57	0.702998±05	0.512994±02	18.2335±03	15.5067±01	38.1186±04
Fm-15	0.703024±06	0.512997±02	18.1838±02	15.5155±01	38.1088±04
Ta-26	0.703004±05	0.512997±01	18.2407±02	15.5066±01	38.1234±04
Km-8	0.703017±04	0.512993±01	18.2184±02	15.5167±01	38.1341±04
Kr-28	0.703037±05	0.512992±02	18.2628±01	15.5081±01	38.1409±02
Kr-9	0.703024±05	0.512996±01	18.2733±03	15.5113±01	38.1544±04
Km-11	0.703034±04	0.512991±02	18.1513±03	15.5298±01	38.1211±05

In-run analytical precision (2σ) is given for each data. Data for Pb isotope are the avarage of the duplicated analyses.

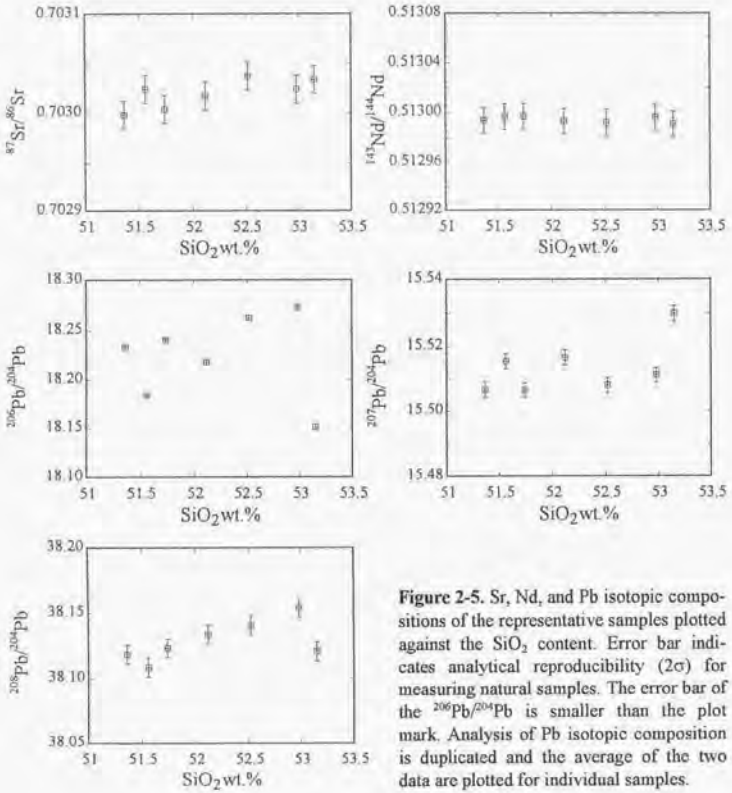

Figure 2-5. Sr, Nd, and Pb isotopic compositions of the representative samples plotted against the SiO_2 content. Error bar indicates analytical reproducibility (2σ) for measuring natural samples. The error bar of the $^{206}Pb/^{204}Pb$ is smaller than the plot mark. Analysis of Pb isotopic composition is duplicated and the average of the two data are plotted for individual samples.

2-4. Petrography and Mineralogy

The modal proportions of phenocrysts (>200 μm) of seven representative samples were measured by point counting technique with 12,000 points per sample (two thin sections) (Table 2-4). The Kutsugata lava is porphyritic with total phenocryst contents generally more than 30 vol.%. Phenocryst assemblages vary systematically in the Kutsugata lava (Fig. 2-2b). The phenocryst assemblage of the North lava is mostly olivine and plagioclase with a few exceptions at the southern end, where some augite phenocrysts are present. The South lava is characterized by common augite phenocrysts in addition to olivine and plagioclase. The abundance of augite phenocrysts tends to be low along the western coast (Fig. 2-2b). Among the North lava samples, those with augite phenocrysts are more differentiated. Similarly, among the South lava samples, those poor in augite phenocrysts are less differentiated.

As described below, all phenocryst phases, which include plagioclase, olivine, and augite, exhibit homogeneous distribution in texture and composition throughout the crystals except for the outermost rims. Rarely, phenocrysts have a central region with distinctive features. In this paper, this region is referred to as the *core* of a phenocryst. The textural and mineralogical features of the phenocryst phases are described below.

Table 2-4. Modal Compositions of Representative Samples of the Kutsugata Lava

	North Lava			South Lava I		South Lava II	
	1	4	5	7	11	13	15
	Fm-57	Fm-15	Ta-26	Km-8	Kr-28	Kr-9	Km-11
	Modal Composition (vol.%)						
Olivine	4.1	3.3	3.5	3.1	2.2	2.7	1.7
Plagioclase	31.8	29.6	30.4	27.8	36.2	27.5	30.1
Augite	0.0	0.0	Tr.	0.2	1.7	2.4	2.9
Groundmass	64.1	67.1	66.1	68.9	59.9	67.4	65.3
	Modal Composition of Cores (vol.%)						
Olivine	0.2	0.4	0.6	0.5	0.2	0.2	Tr.
[Type A]	[0.1]	[0.2]	[0.4]	[0.4]	[0.2]	[0.2]	[Tr.]
[Type B]	[0.1]	[0.2]	[0.2]	[0.1]	[Tr.]	[Tr.]	[0.0]
Plagioclase	0.3	0.3	0.3	0.6	4.7	2.7	0.6
[An-rich]	[0.3]	[0.3]	[0.3]	[0.2]	[0.3]	[0.1]	[0.1]
[Ab-rich]	[0.0]	[0.0]	[0.0]	[0.4]	[4.4]	[2.6]	[0.5]
Augite	0.0	0.0	0.0	Tr.	0.2	0.1	0.2
Total	0.5	0.7	0.9	1.1	5.1	3.0	0.8

Modal composition is based on 6000 points/slide. Phenocryst is a crystal larger than 200 μm. Procedure for determining modal composition of cores is given in the text. Abbreviations; Tr. Trace.

2-4-1. Plagioclase

Plagioclase phenocrysts are prismatic and up to 5 mm long. Olivine and augite inclusions are occasionally observed. The abundance of glass inclusions varies significantly among crystals, some free from glass inclusions (Fig. 2-6a), others with moderate amounts of inclusions (Figs. 2-6b and 2-6c), and some rich in inclusions (Fig. 2-6d). Plagioclase crystals with few glass inclusions tend to be attached together with their long axes parallel to each other (Fig. 2-6a). Plagioclase phenocrysts with many irregularly shaped glass inclusions up to 250 μm in diameter

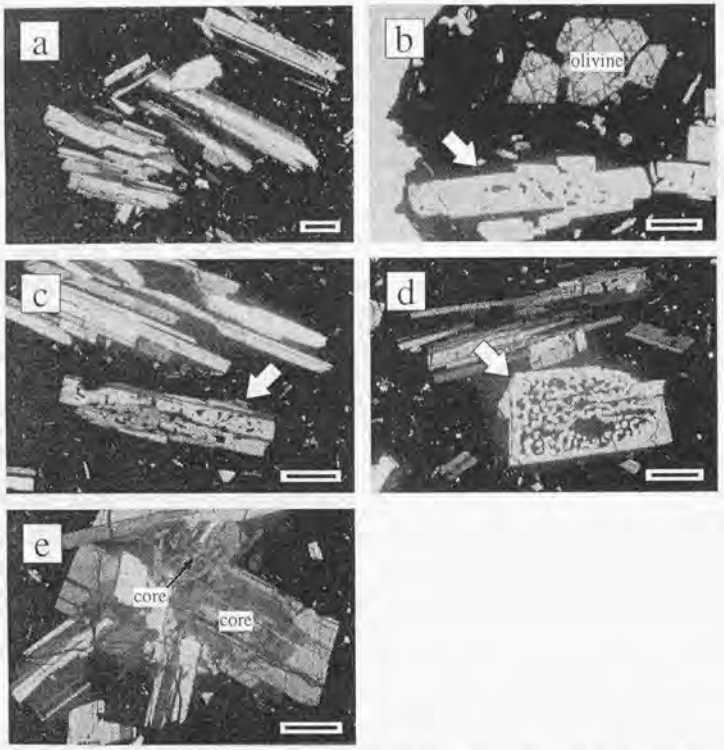

Figure 2-6. Photomicrographs of representative plagioclase phenocrysts. (a) plagioclase phenocrysts free from glass inclusions (Fm-15; locality number 4 in Fig. 2-2, crossed nichols); (b) plagioclase crystal with a few glass inclusions (indicated by arrow) and olivine with skeletal morphology (Fm-15, open nichols); (c) plagioclase phenocryst with moderate amount of glass inclusions (indicated by arrow) (Fm-15, crossed nichols); (d) plagioclase with abundant glass inclusions exhibiting typical honeycomb texture (indicated by arrow) (Fm-25; No. 16 in Fig. 2-2, crossed nichols); (e) Plagioclase phenocryst with a core (Fm-25, crossed nichols). The horizontal black scale bar is 500 μm in length.

Table 2-5. Summary of Plagioclase Phenocryst with Various Amount of Glass Inclusions

Glass inclusions	Few	Moderate	Abundant (honeycomb texture)
Modal abundance	~10 vol.%	~20 vol.%	~5 vol.%
Crystal aggregate	Common	Rare	Absent
Core	Common	Rare	Absent
Figure	Fig. 2-6a	Fig. 2-6b and c	Fig. 2-6d

(Fig. 2-6d) exhibit typical "honeycomb texture" (e.g., *Kawamoto*, 1992), and are present as isolated grains. Generally, a honeycomb plagioclase has euhedral outline. The modal abundances of plagioclase phenocrysts exhibiting typical honeycomb texture (Fig. 2-6d) and those without glass inclusions (Fig. 2-6a) are not large, and most crystals have a moderate amount of glass inclusions (Table 2-5).

Some plagioclase phenocrysts have an optically discernible core with a texture and An content (100×Ca/[Ca+Na+K]) that is distinct from the surrounding margin (Fig. 2-6e). Most (~70 %) of the inclusion-poor crystals (Fig. 2-6a) have cores. On the contrary, plagioclase with moderate amounts of inclusions (Figs. 2-6b and 2-6c) have a smaller proportion with cores (~40 %). Honeycomb plagioclase crystals never have cores. The modal abundance of plagioclase cores (Table 2-4), which is obtained by point counting technique under an optical microscope, is not large relative to the total abundance of plagioclase phenocrysts.

By the absence and presence of the core, plagioclase phenocrysts are classified into non-cored type and cored type. The cored type is further divided into four subtypes, Types 1-4, on the basis of the Na-Ca zoning patterns. Schematic illustrations of these types are shown in Fig. 2-7. The type classification is based on observation of more than 1500 back-scattered electron images of plagioclase phenocrysts in 65 samples from the North lava and 50 samples from the South lava.

The non-cored type plagioclase, with or without glass inclusions, is macroscopically homogeneous in An content throughout the crystals with oscillations of <6 %, except for the outermost sodic rim (Figs. 2-8a and 2-9a). The outer part of the honeycomb plagioclase (Fig. 2-6d) also shows oscillatory zoning, which is texturally continuous with the inner honeycomb texture. The outermost part of the plagioclase has an identical An content to quenched crystals in groundmass. In individual samples, An, FeO*, MgO, and K_2O contents of the non-cored plagioclase phenocrysts are essentially constant, and their values vary systematically with whole-rock SiO_2 content of the samples (Figs. 2-10b, 2-10f, and 2-11). The An content of plagioclase in the North lava ranges from 57 to 65, and that of the South lava from 51 to 62.

Cored-type plagioclase is composed of a core and surrounding clear margin (Figs. 2-7b~2-7f). The clear margin commonly shows oscillatory zoning with or without glass inclusions and has a similar range in An content to that of the non-cored type in each lava (Figs. 2-10a and 2-10b, 2-10c~2-10e and 2-10f), suggesting similar origin to the non-cored type plagioclase. The cores are roughly classified into An-rich core (Type 1) and Ab-rich core (Types 2-4), and these types are described below.

Type 1 is characterized by an extremely An-rich (An71-90) composition, which is surrounded by a clear margin with or without a calcic mantle between them (Figs. 2-7b and 2-7c, 2-8b and 2-8c, and 2-9b and 2-9c). The calcic mantle (An61-71) is characteristically present in the South lava (Figs. 2-7c and 2-8c). Though the An-rich cores are corroded in the central part, they preserve euhedral outlines (Figs. 2-8b and 2-8c). Embayed region is texturally continuous to the clear margin (Figs. 2-7b and 2-8b) or the calcic mantle (Figs. 2-7c and 2-8c). The maximum An content of the An-rich core, which ranges from 75 to 90, does not show a specific spatial varia-

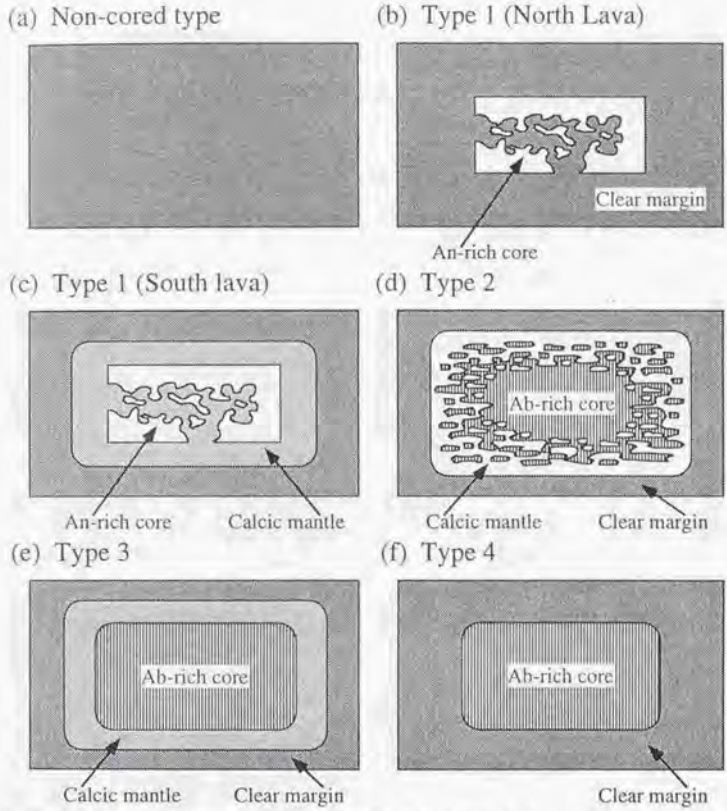

Figure 2-7. Schematic illustration of Na-Ca zoning in plagioclase of non-cored type and cored type; Types 1-4. The shading roughly corresponds with colors in BEIs. See text for details.

tion (Figs. 2-10a and 2-10c). The An content of the calcic mantle in the South lava I is also similar to that of the South lava II (An61-71; Fig. 2-10c). Judging from back-scattered electron images, the cores are suggested to have been present as isolated grains in the magma chamber.

Type 2 is characterized by an Ab-rich core (An55-65) surrounded by a calcic mantle, which is composed of relatively An-rich (An67-78) plagioclase and glass inclusions (Figs. 2-7d, 2-8d, 2-9d, and 2-10d). The Ab-rich core is sharply cut by the calcic mantle with irregular boundary (Fig. 2-8d), showing typical characteristics of partial dissolution (*Tsuchiyama,* 1985; *Nakamura and Shimakita,* 1998).

Type 3 is characterized by an Ab-rich core (An55-67), which is surrounded by a calcic mantle (An60-76) (Figs. 2-7e, 2-8e, 2-9e, and 2-10e). The calcic mantle of this type is less An-rich than that of the Type 2 (Figs. 2-10d and 2-10e) and does not show partial dissolution feature.

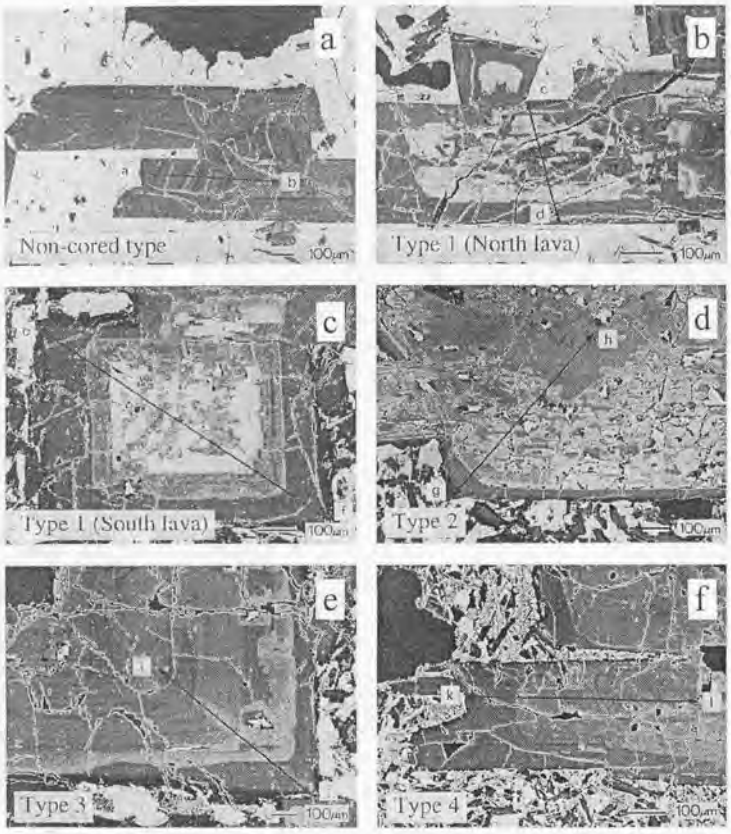

Figure 2-8. Back-scattered electron images of plagioclase phenocrysts. (a) Pl 29-Fm25 (locality No. 16 in Fig. 2-2), non-cored type plagioclase with oscillatory zoning; (b) Pl 11-Fm25, Type-1 plagioclase from the North lava, showing An-rich core filled by sodic plagioclase, which is texturally continuous to the clear margin; (c) Pl 4-Ku11 (No. 17 in Fig. 2-2), Type-1 plagioclase from the South lava, showing calcic mantle that surrounds the An-rich core, and that is continuous to the interstices of the An-rich core; (d) Pl 6-Kr33 (No. 19 in Fig. 2-2), Ab-rich core surrounded by calcic mantle, which is characteristic of partial dissolution (Type 2); (e) Pl 13-Kr27 (No. 20 in Fig. 2-2), Ab-rich core surrounded by calcic mantle, which is further surrounded by clear margin (Type 3); (f) Pl 7-Km7 (No. 21 in Fig. 2-2), Ab-rich core directly surrounded by clear margin (Type 4). Solid lines with arrow heads indicate locations of line profiles shown in Fig. 2-9.

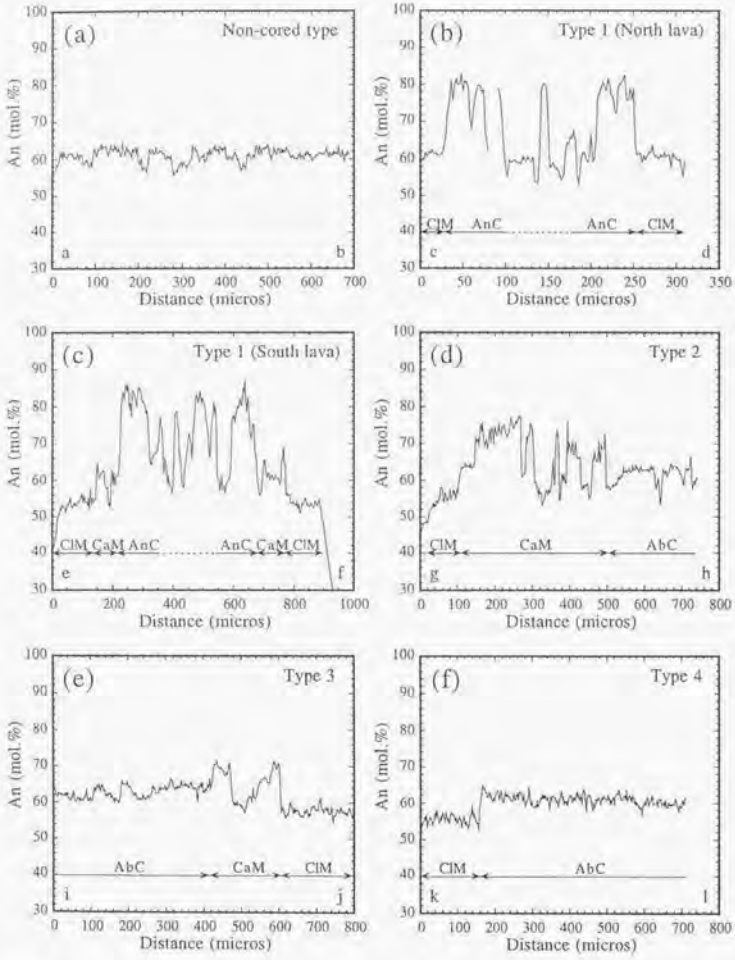

Figure 2-9. Line profiles of An content of plagioclase. Positions of each profile are shown in Fig. 2-8. Abbreviations; ClM: clear margin, CaM: calcic mantle, AnC: An-rich core, AbC: Ab-rich core.

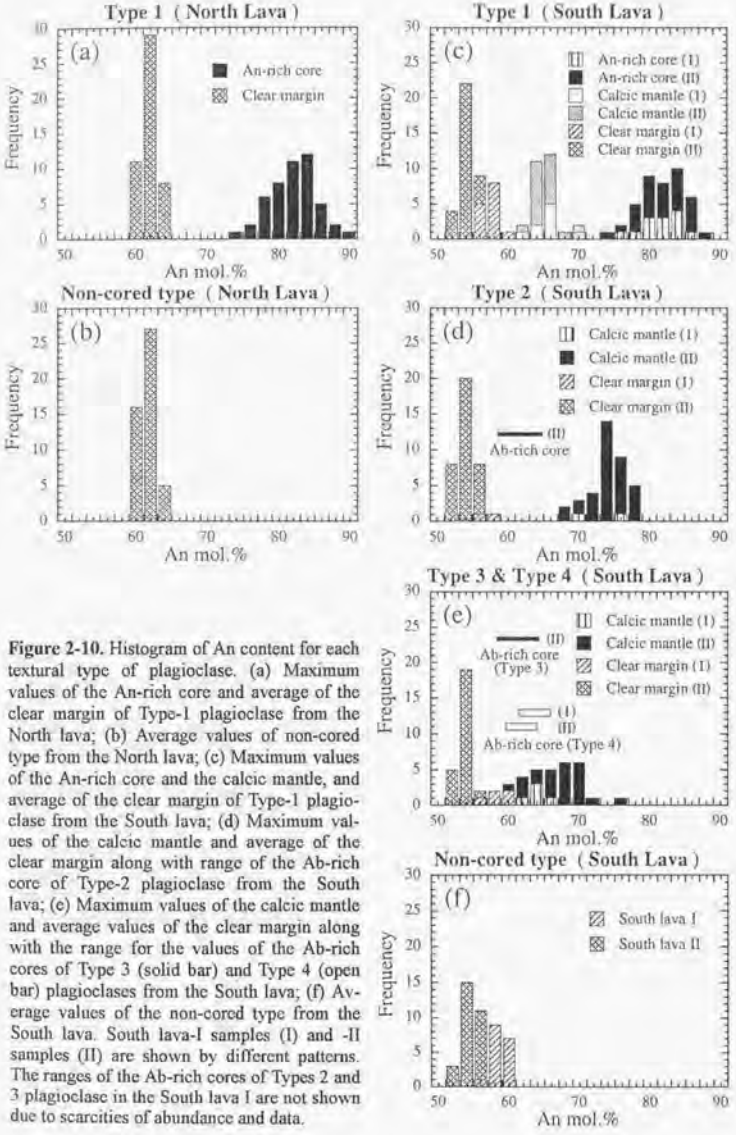

Figure 2-10. Histogram of An content for each textural type of plagioclase. (a) Maximum values of the An-rich core and average of the clear margin of Type-1 plagioclase from the North lava; (b) Average values of non-cored type from the North lava; (c) Maximum values of the An-rich core and the calcic mantle, and average of the clear margin of Type-1 plagioclase from the South lava; (d) Maximum values of the calcic mantle and average of the clear margin along with range of the Ab-rich core of Type-2 plagioclase from the South lava; (e) Maximum values of the calcic mantle and average values of the clear margin along with the range for the values of the Ab-rich cores of Type 3 (solid bar) and Type 4 (open bar) plagioclases from the South lava; (f) Average values of the non-cored type from the South lava. South lava-I samples (I) and -II samples (II) are shown by different patterns. The ranges of the Ab-rich cores of Types 2 and 3 plagioclase in the South lava I are not shown due to scarcities of abundance and data.

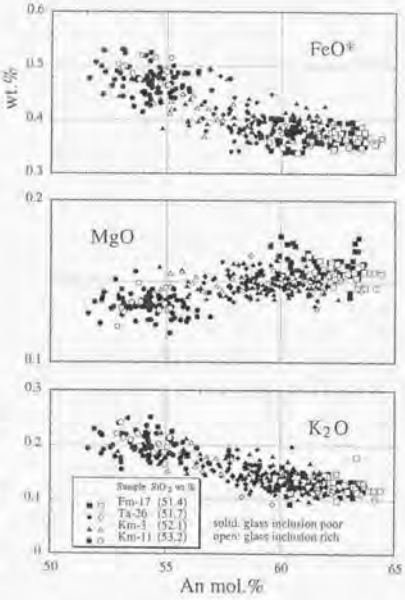

Figure 2-11. FeO*, MgO, and K_2O contents of glass inclusion-poor plagioclase (filled marks) and inclusion-rich plagioclase (open marks), excluding cores in the representative samples, plotted against the An content. Numbers in parentheses in the legend are whole-rock SiO_2 content of the samples. FeO* is total Fe as FeO.

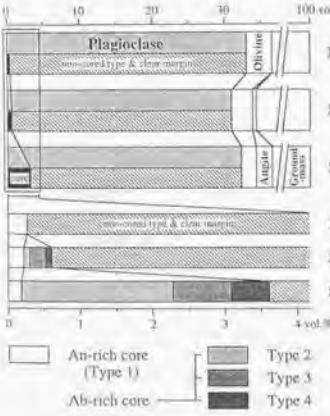

Figure 2-12. Modal abundance of each type of plagioclase for the North lava, South lava I, and South lava II. Upper three graphs are enlarged to lower graphs.

Type 4 is characterized by an Ab-rich core (An55-67) that is directly in contact with a clear margin (~An61) (Figs. 2-7f, 2-8f, 2-9f, and 2-10e). The An content abruptly decreases at the contact (Fig. 2-9f).

The Ab-rich cores of Types 2-4 plagioclase have a few glass inclusions and commonly exhibit oscillatory zoning (Figs. 2-8d~2-8f). The An content of the Ab-rich cores in Types 2, 3, and 4 have similar ranges in the South lava II (An59-65, Figs. 2-10d and 2-10e). The Type-4 core in the South lava I, on the other hand, is more An-rich than that of the South lava II (Fig. 2-10e).

The cored-type plagioclase shows systematic spatial distribution in the Kutsugata lava. The Type 1 (An-rich core) is present throughout the lava with a volume of 0.2~0.3 % (Table 2-4; Fig. 2-12). The Ab-rich cores (Types 2-4) occur only in the South lava, and they

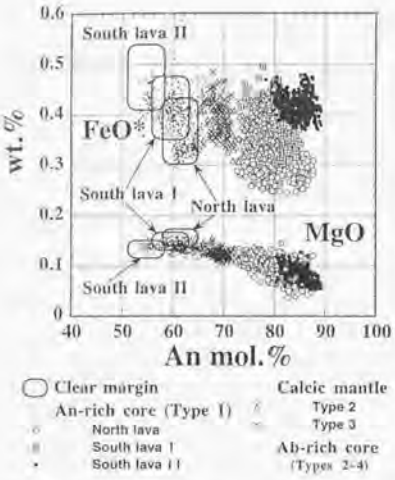

Figure 2-13. MgO and FeO* contents of plagioclase plotted against the An content. Data are from the An-rich core of Type 1, from the calcic mantles of Types 2 and 3, from the Ab-rich cores of Types 2-4, and from the clear margins of Types 1-4. FeO* is total Fe as FeO.

are rarely in direct contact with cores of olivine and augite phenocrysts. The abundance of the Ab-rich cores increases with bulk silica content in the South lava I, but decreases in the South lava II (Table 2-4).

Figure 2-13 shows MgO and FeO* contents in plagioclase cores of the Kutsugata lava plotted against An content. The FeO* content in the An-rich cores of Type-1 plagioclase systematically increases from the North lava to the South lava II. The MgO content of the An-rich cores decreases as An content increases, and the difference among lavas is indistinguishable, contrary to FeO* content. The MgO contents of the calcic mantles of Types 2 and 3 also correlate negatively with the An content and exhibit similar trends to that of the An-rich core of Type-1 plagioclase. In contrast to such negative correlation, the MgO content in the Ab-rich core is almost independent of An content. As shown in Fig. 2-11, the MgO contents of the clear margin correlate positively with An content and are distinguishable among the lavas.

2-4-2. Olivine

Olivine phenocrysts, up to 1.5 mm in diameter, are commonly euhedral and contain glass inclusions. Olivines with skeletal morphology are also present (Fig. 2-6b). As do plagioclase phenocrysts, olivine shows various morphologies ranging from euhedral crystals free of glass inclusions to skeletal crystals.

Zoning of olivine phenocrysts was examined in detail because olivine is an important phase for constraining the possible differentiation processes of the Kutsugata magma. All olivine phenocrysts within two thin sections were analyzed with EPMA and 80 to 120 line profiles with 10-20 μm steps were obtained for individual representative samples. Most olivine phenocrysts are homogeneous in terms of Mg#, CaO, and NiO contents except for the rims (Fig. 2-14a). The Mg# and NiO contents in olivine phenocrysts, excluding rims and cores described below, vary systematically with the whole-rock SiO_2 content, although these values show a limited range and are independent of crystal morphology in individual samples (Fig. 2-15). The Mg# shows systematic spatial variation in the lava; the North lava has olivine with Mg# from 78.0 to 81.0, the South lava I from 75.5 to 78.0, and the South lava II from 74.0 to 75.0. Rarely, cores with low-CaO and high-NiO compositions are present, and are divided into Types A and B (Figs. 2-14b and 2-14c). The modal compositions are obtained by multiplying the fraction of the core by the total olivine abundance for individual samples (Table 2-4).

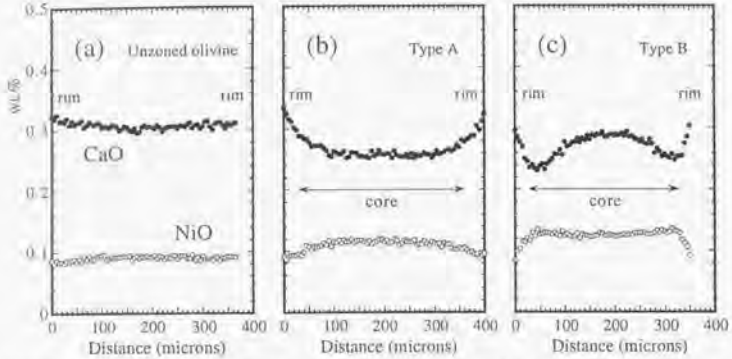

Figure 2-14. Line profiles of CaO and NiO contents of olivine phenocrysts. (a) olivine phenocryst with homogeneous CaO and NiO contents (ol 52-Ta26), (b) olivine phenocryst with low CaO and high NiO core (ol 16-Ta26). The NiO content of the core is normally zoned (Type-A core), (c) olivine phenocryst with high CaO and low NiO core (ol 2-Ta26). The NiO content of the core shows reverse zoning (Type-B core).

Type-A olivine cores are characterized by normal zonation of NiO content (Fig. 2-14b). The CaO content of the core is constant or increases toward the rim. Some cores have higher Mg# than unzoned olivine within individual samples. The Mg# of the cores ranges from 79 to 83 in the North lava, and from 75 to 81 in the South lava. In the South lava, some Type-A cores are in direct contact with the Ab rich-core plagioclase. The abundance of Type-A cores increases with an increase of whole-rock SiO_2 content, and has a peak at around the boundary between the North and South lavas (Table 2-4). The NiO and CaO contents of the cores, together with those of the unzoned olivine, are shown in Fig. 2-16. Compared with the unzoned olivine, Type-A cores are sporadically dispersed in individual samples. However, the NiO content of the cores tends to decrease as the bulk SiO_2 content of host samples increases (Fig. 2-16). The cores are always richer in NiO and poorer in CaO than the unzoned olivine crystals within the same samples.

Type-B cores are characterized by reverse zoning of NiO content (Fig. 2-14c). Therefore, the NiO content in an overall grain shows an M-shaped zoning profile. Rarely, Mg# also exhibits reverse zoning. The CaO content of the cores decreases toward the margin and then increases toward the rim (Fig. 2-14c). The degree of CaO zonation in the cores is variable and some show a flat pattern. Except for the rim, the variations of Mg#, CaO, and NiO contents in individual grains are not so large as their variations in the Kutsugata lava, and these values are mostly similar to those of the Type-A core in each sample.

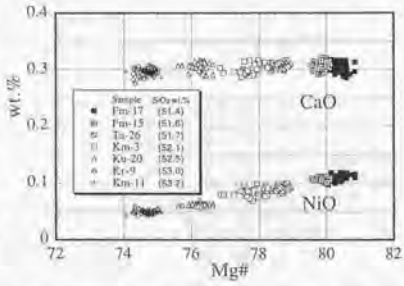

Figure 2-15. CaO and NiO contents of olivine excluding cores, in representative samples plotted against Mg#.

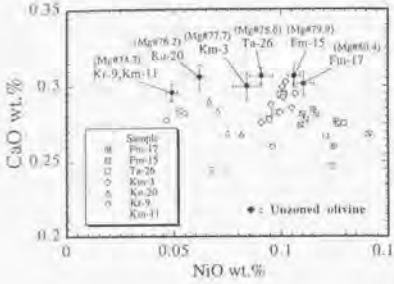

Figure 2-16. CaO and NiO contents of the Type-A olivine core. Those of the unzoned olivine phenocrysts (Fig. 2-14a) are shown by filled circle with standard deviations (1σ) for comparison. The average Mg# is also shown in parenthesis.

2-4-3. Augite

Augite phenocrysts are euhedral and have diameters ranging from 0.5 to 1.5 mm. Glass, olivine, and plagioclase inclusions are occasionally found (Fig. 2-17a), and the amount of these inclusions varies among crystals. Throughout the crystals, strong oscillatory zoning is developed, and is commonly superimposed on sector zoning (Fig. 2-17a). Although Mg# of augite is slightly affected by sector and oscillatory zonings (commonly less than 1 unit in Mg#), the variation in Mg# is not large within individual grains and samples. The Mg# of augite phenocrysts, excluding the rims and cores, decreases systematically from 83.1 to 79.2 with increase in bulk SiO_2 content

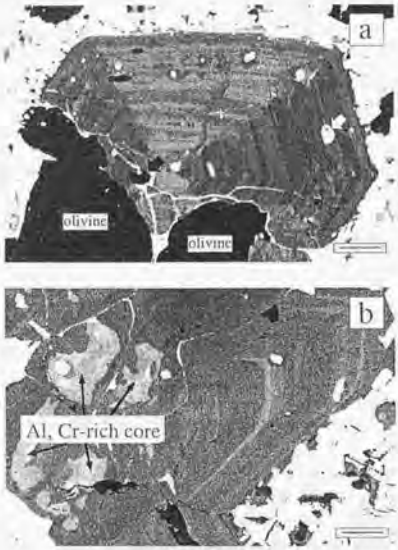

Figure 2-17. Al distribution in representative augite phenocrysts. Note that the lighter part is more concentrated in Al. (a) Commonly-observed augite phenocrysts with oscillatory zoning superimposed on sector zoning throughout the crystal (cpx 1-Kr9; locality number 13 in Fig. 2-2), (b) Augite phenocryst with Al and Cr-rich cores (cpx 19-Ku20; No. 17 in Fig. 2-2). White and black parts in augite are plagioclase and olivine inclusions, respectively (indicated by white and black arrows in (a)). The horizontal black scale bar is 100 μm in length.

(Fig. 2-18). Mg-Fe distribution coefficients calculated from the average Mg# of olivine and augite phenocrysts systematically decrease as Mg# of olivine increases (Fig. 2-18), which is suggestive of higher crystallization temperature for the magma with less differentiated composition in the Kutsugata lava (*Kawasaki and Ito*, 1994).

Augite phenocrysts have cores with distinctive Al and Cr compositions (Fig. 2-17b). The modal composition of the cores was determined by map analyses with EPMA for all augite phenocrysts within two thin sections for individual representative samples (Table 2-4). The cores are generally present in more differentiated samples in the South lava. The abundance of cores does not exceed 0.2 vol.% throughout the lava (Table 2-4). Some augite cores are in direct contact with Ab-rich plagioclase cores.

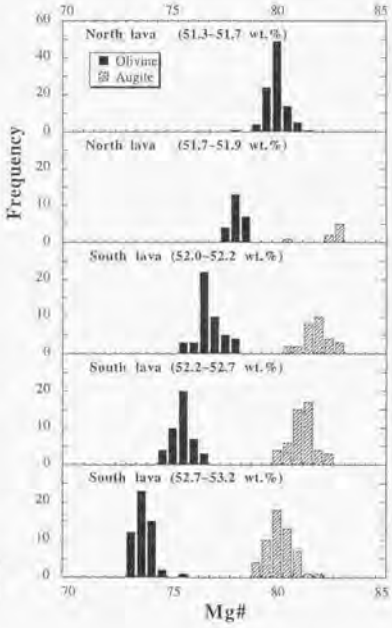

Figure 2-18. Histograms of Mg# of olivine and augite phenocrysts excluding the cores.

2-5. Pre-Eruptive Magmatic Temperature

Temperatures of the Kutsugata magmas are estimated with several geothermometers. The magmatic temperature of the samples Fm-17 and Km-11 (Table 2-1), the least and most differentiated rocks in the Kutsugata lava, are estimated by olivine-melt thermodynamic equilibria using the solution model for olivine of *Hirschmann* (1991) and for silicate melt of *Ghiorso and Sack* (1995). Both equilibrium temperature and Mg# of olivine can be calculated independently, by giving the conditions of pressure (1 atm) and melt composition (quenched groundmass with ferric-ferrous ratio after the model of *Sack et al.* 1980). In this way, a magmatic temperature of

1110 °C and an Mg# of 80.5 are obtained for the sample Fm-17. The calculated Mg# is consistent with the analyzed values (Fig. 2-15), which ensures the validity of this temperature estimation. Similarly, the temperature of 1070 °C for Km-10 magma is obtained. The minimum temperature for the Kutsugata lava can also be estimated from the composition of augite in samples that are not saturated with orthopyroxene. The estimated minimum temperature ranges from 1050 to 1120 °C in the North lava and from 950 to 1100 °C in the South lava (*Lindsley*, 1983).

2-6. Boundary Layer Crystallization

On the basis of several petrographic and chemical criteria given above, the composition and temperature of the lava varied systematically with time during the eruption. Mineral and moral compositions of phenocrysts and plagioclase and olivine zonings are also strongly correlated with chemical variation of the Kutsugata lava, though the SiO_2 contents of the lava samples exhibit only 2 wt.% variation. By analyzing zoning patterns of crystals with the constraints of phase diagram, it is documented that the Kutsugata lava sampled crystals from the low-temperature mushy boundary layer along the chamber walls, as well as those from the hot main magma in the magma chamber.

2-6-1. Origin of plagioclase cores

An-rich core

While extremely calcic plagioclase is quite common in high-alumina basalts and gabbroic nodules in island arcs (*Arculus and Wills*, 1980; *Brophy*, 1986; *Crawford et al.*, 1987; *Brophy et al.*, 1996), it is not common in high Na/K alkali basalt, probably because of the Na-rich nature of the magmas. In order to clarify the magmatic evolution of the Kutsugata magma, it is crucial to explain the origin of the An-rich cores of the Type-1 plagioclase. In this section, this problem is considered by using the experimentally determined compositional relationships between silicate melt and plagioclase.

Figure 2-19 shows the albite-anorthite binary diagram in which plagioclase-glass pairs are projected from experimental multicomponent systems (e.g., *Sisson and Grove*, 1993). The multicomponent glass compositions are projected by calculating normative 100·an/(an+ab) according to *Housh and Luhr* (1991). Plagioclase-melt equilibria are almost independent of starting compositions, oxygen fugacity, and presence of other liquidus phases (*Housh and Luhr*, 1991). Data for alkaline compositions at 1 atm pressure, 10 kbar under dry condition, and under H_2O-saturated at 2 kbar are plotted in Fig. 2-19.

In order to apply this phase diagram to the Kutsugata magma system, liquid composition needs to be provided. It is shown that the whole-rock composition of the lava represents the liquid composition. Chemical compositions of all phenocrysts, excluding the cores, vary systematically with whole-rock composition: An, FeO*, MgO, and K_2O contents in plagioclase (Fig. 2-11), Mg# and Ni content in olivine (Fig. 2-15), and Mg# of augite (Fig. 2-18). Reverse Ni zoning in some olivine phenocrysts and Na-Ca oscillatory zoning in plagioclase phenocrysts are preserved, which suggests that the original compositions of olivine and plagioclase phenocrysts were not modified, based on the slow diffusion rates of Ni (*Clark and Long*, 1971) and CaAl-NaSi in plagioclase (*Grove et al.*, 1984). If the main volume of phenocrysts crystallized before the differentiation of the Kutsugata lava, it would be expected that their compositions are nearly constant or randomly varied throughout the lava. Furthermore, the modal abundance of plagioclase phenocrysts, the dominant phase of the lava, is independent of whole-rock composition (Table 2-4), which negates the possibility that separation of these phenocrysts produced whole-

rock compositional variation. Therefore, it is reasonable to assume that the main phenocrysts crystallized *in situ* from individual magma batches with observed whole-rock compositions, and thus it is plausible to consider that the whole-rock composition represents a liquid composition before the crystallization of the main phenocryst. The crystallization sites of the main phenocryst is discussed in the later section.

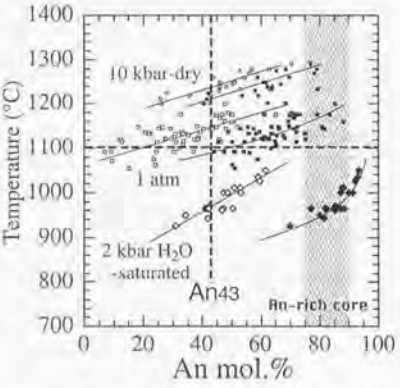

Figure 2-19. Liquid and coexisting plagioclase compositions projected on the anorthite-albite join for the different conditions (1 atm, 10 kbar-dry, and 2 kbar water-saturated). Projection scheme of glass is after *Housh and Luhr* (1991). One-atm data from *Mahood and Baker* (1986), *Sack et al.* (1987), and *Thy* (1991), 10 kbar-dry data from *Bartels et al.* (1991), *Thy* (1991), *Kinzler and Grove* (1992), *Fram and Longhi* (1992), *Grove et al.* (1992), and *Panjasawatwong et al.* (1995), and 2 kbar water-saturated data from *Sisson and Grove* (1993). Anorthite 43 represents the whole-rock composition of the least differentiated sample from the Kutsugata lava assumed to be a melt. 1100 °C is the estimated minimum temperature of the least differentiated sample in the Kutsugata lava. Dotted zone (An75-90) shows the range of An content of the An-rich core of Type-1 plagioclase.

The least differentiated Kutsugata lava projects at An43 in Fig. 2-19 (the most differentiated rock projects at An35). If the Kutsugata magma with normative An of 43 was at a temperature above 1100 °C, that melt can never have been in equilibrium with plagioclase of ~An90. Judging from the shape and position of the plagioclase saturation loops for 1 atm and 2 kbar H_2O-saturated conditions, the equilibrium An content that can coexist with this liquid was at most 80 at several hundred bars if the melt was H_2O saturated.

It is possible that the high-An plagioclase grew from a primitive parent magma of the Kutsugata lavas that was not erupted, and this conjecture is tested by estimating a more primitive composition. Because the projected positions of liquids in Fig. 2-19 are independent of degree of olivine fractionation, the effect of adding plagioclase of An83 (average An content for the An-rich core) to the least differentiated Kutsugata lava was calculated in order to investigate the effect of plagioclase fractionation. With 10 wt.% addition of the plagioclase, the melt composition reaches only An48. Addition of at least 40 wt.% of An83 plagioclase is needed to bring the melt in equilibrium with An90 plagioclase. In this case, the whole-rock Al_2O_3 content would increase to 23 wt.%, which rules out this mechanism.

If the estimated temperature above 1100 °C is correct, the An-rich cores may derive from a magma unlike the Kutsugata lavas or even from crustal materials. However, the systematic increase of the FeO* content in the An-rich cores from the North lava to the South lava II (Fig. 2-13) requires that the An-rich cores were not derived from an exotic magma or crustal materials. If they were derived from exotic origins, it is expected that FeO* content in the An-

rich cores are mostly constant or completely scattered throughout the Kutsugata lava. Moreover, the MgO contents of plagioclase in gabbros analyzed under the same conditions described above are fairly low (~0.03 wt.%) for gabbroic xenoliths from Ichinomegata (*Aoki*, 1971), which is similarly located at the back arc side in the northeastern Japan arc, and also for oceanic gabbros from Ocean Drilling Program Hole 735B (*Ozawa et al.*, 1991).

It is concluded from these considerations that the An-rich core is not exotic and therefore that the magma temperatures for crystallizing An-rich cores were below 1100 °C. If so, the liquid with An43 can equilibrate with ~An90 plagioclase under water-saturated conditions at 2 kbar and 960 °C, for example (Fig. 2-19). This estimation may not be strictly correct because appearance of augite lowers the An content of the projected liquid composition of An43. The more water-rich and low-temperature conditions relative to those of the average Kutsugata magma were, however, needed for plagioclase with An content as high as 90 to be crystallized. Such conditions must have been attained locally in the magma reservoir.

Many experimental and theoretical works concerning cooling of magma from the wall have inferred that a mushy boundary layer composed of crystals and fractionated interstitial liquid is formed between the wall and a convecting main magma body (Fig. 2-20) (e.g., *Brandeis and Jaupart*, 1986; *Turner et al.*, 1986). The localized low-temperature and water-rich environment was achieved most plausibly in a mushy layer. It is shown below that MgO content in An-rich cores is also consistent with this inference.

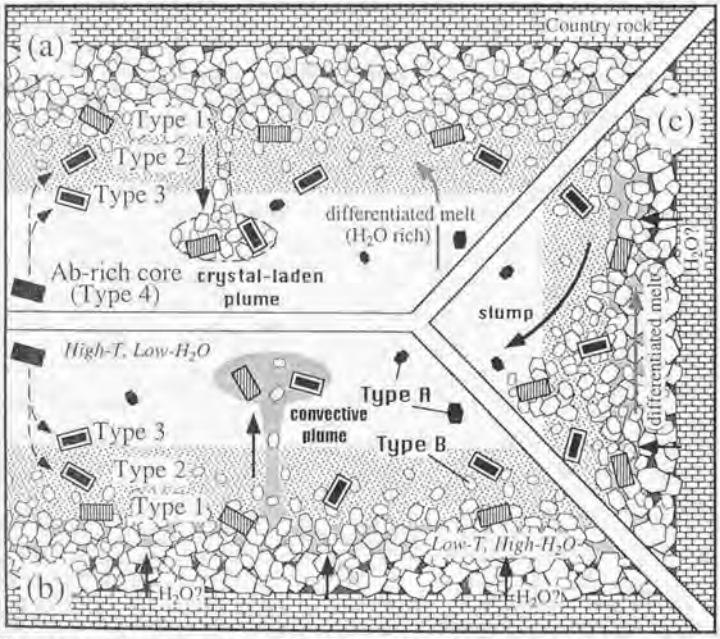

Figure 2-20. Schematic illustration of a magma chamber near the roof (a), floor (b), and sidewall (c), showing formation and transportation processes of cored-type plagioclase (rectangles) and olivine cores (hexagons). See text for details.

2. Constraints from the Kutsugata Lava

A negative correlation between MgO and An contents is observed in the An-rich core of Type-1 plagioclase (Fig. 2-13). The partition coefficient of MgO between plagioclase and silicate melt (D_{Mg}) is mostly independent of cooling rate (0.1~10 °C; *Phinney,* 1992) and oxygen fugacity (*Sato,* 1989; *Phinney,* 1992). However, compositional dependence of the D_{Mg} has been suggested. Partition coefficients of Sr and Ba between plagioclase and silicate melts are known to have strong dependence on crystal-chemistry in wide range of An content (between An 0 and 100) (*Blundy and Wood,* 1991). These elements are more compatible in more Ab-rich composition in plagioclase. *Blundy and Wood* (1994) suggested that similar variation is also expected in D_{Mg}. Therefore, it is crucial to distinguish the effect of D_{Mg} from that of melt composition variation on negative correlation observed in the An-rich core (Fig. 2-13).

Compositional dependence of the D_{Mg} is roughly estimated from the data of *Sato* (1989). The D_{Mg} at An84 plagioclase is 0.037 and that of the An77 is 0.044 (*Sato,* 1989). Assuming that the ln D_{Mg} is linearly dependent on the An content of plagioclase, the D_{Mg} at An90 is 0.032 and that of the An70 is 0.052. Therefore, nearly 50 % decrease of MgO content from An 70 to 90 of the An-rich cores (Fig. 2-13) requires that the more calcic plagioclase crystallized from less MgO melt. This accords with crystallization of the An-rich cores in a mush zone where the interstitial melt is differentiated in terms of MgO content.

Ab-rich core

Ab-rich cores are common in Types 2, 3, and 4 plagioclase. The An content of the Ab-rich cores of these types are similar in the South lava II (Figs. 2-10d and 2-10e) and oscillatory zoning is also common. These observations suggest that the Ab-rich cores underwent a similar formation process.

In the main magma body, the magma temperature was above the plagioclase liquidus when the North lava resided in the chamber. This is consistent with absence of Ab-rich cores in the North lava. By contrast, the magma temperature is estimated to have been below the plagioclase liquidus when the South lava occupied the reservoir, and the Ab-rich cores of Types 2-4 plagioclase are inferred to have crystallized in the main magma body. The normative An content of the South lava is 40, which is low enough to crystallize Ab-rich plagioclase (~An67) with a certain amount of H_2O in the melt at temperature as high as 1000~1100 °C (Fig. 2-19).

Morphology of An-rich core

The observation that the outlines of the An-rich cores of Type-1 plagioclase are well preserved though the central part of the cores are segmented (Figs. 2-7b, 2-7c, 2-8b, and 2-8c) indicates a significant change in chemical and physical conditions of the surrounding melt. The corroded morphology suggests that many melt inclusions were originally present before melting of the An-rich core. Figure 2-21 shows schematic albite-anorthite binary loops projected from a natural multicomponent system. Loops A and B correspond to the interstitial melt of the assumed mushy boundary layer (water-saturated) and the main magma body in a chamber (water-deficient), respectively (Fig. 2-21). In the mushy layer, the plagioclase of the An-rich core (S_0) is in equilibrium with melt (L_0) at a temperature T_0, representing the melt inclusion composition.

When plagioclase with the An-rich core composition is brought into the main magma body (L_{m1} at T_1 if the temperature of the main magma body is below plagioclase liquidus or L_{m2} at T_2 if the temperature above liquidus), plagioclase (S_0) with melt inclusions (L_0) is heated to S_1 and L_1 at temperature T_1 or to S_2 and L_2 at T_2. Then, the host plagioclase (S_1 or S_2) surrounding the melt inclusions (L_1 or L_2) begins to melt as far as these inclusions are closed in the host plagioclase system, because the loop for this system remains to be Loop A with a slight upward shift. The upward shift depends on the water content in the melt inclusions when host plagioclase is melted and mixed with the original melts. The surface of plagioclase crystal, on the other hand, is in the condition of Loop B. If the temperature is T_2, L_{m2} is above the liquidus and plagioclase reacts with the melt. But this reaction may be insignificant if the difference between T_2 and liq-

uidus temperature is not large. Extremely calcic nature of the plagioclase further delays the reaction. In the case of T_1, L_{m1} can crystallize plagioclase with the composition X. Thus crystallization of more sodic plagioclase takes place surrounding the An-rich core.

The high-temperature condition (T_2) corresponds to the North-lava magma, and the low-temperature condition (T_1) to the South-lava magma (Fig. 2-21). In the latter case, plagioclase (X) precipitated to form the calcic mantle of the Type-1 core (Figs. 2-7c and 2-8c), whereas the calcic mantle does not develop in the former case.

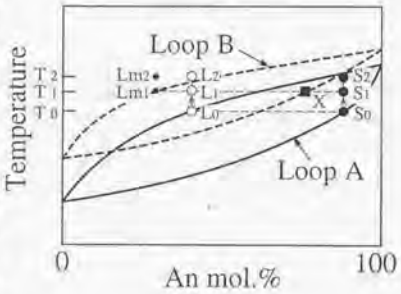

Figure 2-21. Schematic albite-anorthite diagram projected from multicomponent systems. Loop A (solid lines) is for H_2O-rich melt in the mush zone and melt inclusions totally enclosed in plagioclase. Loop B (broken lines) is for plagioclase and the surrounding melt in the main part of the magma chamber. L_0-L_2 and S_0-S_2 are assumed compositions of melt inclusions and surrounding plagioclase at each temperature, T_0, T_1, and T_2. L_{m1} and L_{m2} are compositions of melt in the main magma body at T_1 and T_2. X is the equilibrium plagioclase composition on the Loop B.

2-6-2. Origin of olivine cores

Detailed analyses of plagioclase phenocrysts suggest that the lava sampled plagioclase crystals derived from the mushy boundary layer (An-rich core), as well as those from the main magma body (Ab-rich core) of the Kutsugata magma chamber, as described above. In this section, it is demonstrated that the zoning and compositions of olivine cores have the same origin as the plagioclase cores.

The cores of olivine phenocrysts are of two types; Type A and Type B (Fig. 2-14). Some Type-A olivine cores in the South lava show evidence for simultaneous growth with the Ab-rich plagioclase which crystallized in the main part of the reservoir. Therefore, Type-A cores are suggested to have formed in the main magma chamber. Type-B cores exhibit reverse zoning in NiO content (and Mg#). This indicates that the inner part of the core crystallized from more differentiated melt in terms of Ni content and Mg# than the outer margin. Though no Type-B core in direct contact with An-rich plagioclase was found, it is plausible to consider that the Type-B cores were derived from the mush zone where the interstitial melt was differentiated (Fig. 2-20). The inner parts of the cores might have been much lower in Ni and Mg# than observed because they may have been annealed after transportation to the hotter, less differentiated main magma body.

2-6-3. Mushy boundary layer

H_2O enrichment in mushy boundary layer

The features of a crystallizing boundary layer in a natural system are excellently provided from a series of drilling of the Hawaiian lava lakes (e.g., *Helz*, 1980; *Helz and Thornber*, 1987; *Helz et al.*, 1989). One of the most important clarification of these projects is that the mineral assemblages and coexisting interstitial melt spans the whole interval between the solidus and the liquidus in the mushy boundary layer (*Marsh*, 1996; *Tait and Jaupart*, 1996), that is, the liquid line of descent in the boundary layer is principally similar to that of the main magma body.

The Ab-rich cores of Types 2-4 plagioclase are inferred to have been in equilibrium with the magma in the main magma body and to represent a phase crystallized from the main liquid line of descent of the Kutsugata magma. Therefore, crystallization of plagioclase with more calcic composition (An-rich core) than the Ab-rich cores in the boundary layer needs another factor.

A plausible mechanism to change the liquid line of descent in the mushy boundary layer is addition of H_2O expelled from the chilled margin and/or addition of groundwater from the surrounding crust. Contributions from the surrounding crust are actually suggested from the variation of isotopic compositions (Fig. 2-5). Addition of water may have expanded the liquidus field of olivine and depressed the liquidus temperature of plagioclase and augite drastically. Olivine is, hence, the sole liquidus phase during a significantly large cooling interval, preventing the depletion of anorthite component in the melt until a lower temperature. The absence of augite phenocryst in the most part of the North lava is consistent with the suppression of the augite field even in the low-temperature boundary layer. From low-temperature and H_2O-rich evolved melt, An-rich and Mg-poor plagioclase can have crystallized. When the interstitial melt was saturated with water, sodium may have selectively been partitioned into the fluid phase (*Sakuyama and Kushiro*, 1979), further promoting crystallization of An-rich plagioclase. Crystallization of plagioclase with An-rich composition in the mushy boundary layer will be further discussed and confirmed by utilizing a numerical model in the later section (Section 4-4).

The MgO content of the Ab-rich cores is mostly constant in spite of the An content variation (Fig. 2-13). Taking compositional dependence of D_{Mg} into consideration, the more sodic Ab-rich cores crystallized from less MgO melt, which is similar to the generally-expected liquid line of descent. The negative correlation in the An-rich cores, contrary to the Ab-rich cores, also implies that the liquid line of descent in the boundary layer was fairly different from that of the main magma body in the Kutsugata-magma chamber. The variation of the FeO* content in the An-rich cores from the North lava to South lava II (Fig. 2-13) may have reflected the difference of oxygen fugacity in melt (*Sato*, 1989; *Phinney*, 1991).

Transportation of Ab-rich cores into mushy boundary layer

The main difference between the Types 2 and 3 plagioclase is the presence or absence of evidence for partial dissolution (Figs. 2-7d, 2-7e, 2-8d, and 2-8e) and An content of the calcic mantle (Figs. 2-10d and 2-10e). This may reflect the degree of disequilibrium between the Ab-rich core and the surrounding melt. Taking negative correlation between the An and MgO contents in the calcic mantles of Types 2 and 3 cores into account (Fig. 2-13), it is inferred that formation of the calcic mantles of these types were related to the mush zone (Fig. 2-20) as in the case of the An-rich core of Type-1 plagioclase.

If Ab-rich plagioclase is brought from the main magma body into the deep interior of the mushy layer (Fig. 2-20), the An content in equilibrium with the surrounding melt becomes more calcic. This situation promotes dissolution of the Ab-rich plagioclase. If the Ab-rich plagioclase is not brought to the deep interior of the mushy layer, only growth of slightly calcic plagioclase takes place. This is because the difference of An content between the Ab-rich core and plagioclase in equilibrium with the surrounding melt is not large. Inferred formation site of Types 2

and 3 plagioclase is consistent with more An-rich and less-MgO compositions of the calcic mantle of Type 2 than that of the Type-3 core (Figs. 2-10d, 2-10e, and 2-13). The Ab-rich core of Type-4 plagioclase represents Ab-rich plagioclase crystallized in the main magma body without being brought to the mushy boundary layer (Fig. 2-20). Considering that most Ab-rich cores have calcic mantle (Type2 and Type 3) (Fig. 2-12), crystallization of the Ab-rich cores might have been restricted to the marginal part of the main magma body. If the Ab-rich cores crystallized throughout the main magma body, the population of the Type-4 core would be dominant.

Transportation mechanism of crystals

Plagioclase and olivine crystals in the Kutsugata-magma chamber cycled in and out of the mushy boundary layer. The Type-1 cores and the Type-B olivine cores, formed in the boundary layer, were brought to the main magma body. Some Ab-rich cores, crystallized in the main magma body, were transported to the mush zone and then brought to the main body. In this section, plausible mechanisms of these cycles are discussed as to the assumed roof, floor, and sidewall-boundary layers.

At the roof boundary layer (Fig. 2-20a), H_2O-rich and low-temperature evolved liquids may accumulate from the sidewall of the chamber (*McBirney et al.*, 1985) and even from the floor boundary layer (*Helz et al.*, 1989; *Tait and Jaupart*, 1992). If the extra water is added to the fractionated melt before segregation from sidewall and floor boundary layers, the melt takes a different liquid line of descent from that of the main magma body. The An-rich plagioclases and the Type-B olivines crystallized from the accumulated melt in the roof boundary layer is likely to have transported to the main magma body by crystal-laden plume and dispersed in the chamber (*Marsh*, 1988). However, most of the observed An-rich plagioclase and Type-B olivine may not represent crystals transported from the roof mush zone, considering that they have euhedral outline and are suggested to have been present as isolated grains in the magma.

In the deeper interior of the floor boundary layer (Fig. 2-20b), expelled water and/or groundwater is likely to exist as a vapor phase due to high crystallinity, and move upward through interstitial melt. During ascent, this vapor phase can become dissolved in the interstitial liquid if this is undersaturated with water. Then, low-temperature and high-water condition, which is never formed by the main liquid line of descent of the Kutsugata magma, is produced. Unlike the roof boundary layer, light fractionated melt is unstable in the floor boundary layer, and compositional convection sets in (*Tait and Jaupart*, 1992). The crystals grown in the boundary layer could have been transported to the main magma body by such convective currents. This view is discussed in more detail in the later section.

Along the sidewall of the chamber (Fig. 2-20c), light differentiated melt moves upward (e.g., *McBirney et al.*, 1985). If additional water is supplied from the solidified margin and crust to the differentiated melt, An-rich plagioclase may occur in the melt. Crystals in the sidewall boundary layer might be brought to the main magma body by slumping of the mush zone (Fig. 2-20e).

2-7. Boundary Layer Fractionation

It is documented in the Section 2-6 that a mushy boundary layer was developed along the wall of the Kutsugata magma chamber. The main issue of this section is that how compositional variation of the lava was produced in the magma chamber through development of the mushy boundary layer. By utilizing the whole-rock composition trends, the magmatic differentiation of the Kutsugata magma is demonstrated to have proceeded principally by mixing of fractionated melt derived from the floor mush zone with the overlying main magma.

2-7-1. Origin of composition trends

The Kutsugata lava forms a smooth compositional series, which is composed of three linear segments; for the North lava, South lava I, and South lava II (Fig. 2-3). On the other hand, the $^{87}Sr/^{86}Sr$ ratio increases with whole-rock SiO_2 content and the $^{206}Pb/^{204}Pb$ ratio varies randomly with the SiO_2 content (Fig. 2-5). These indicate that the evolution of the Kutsugata magma involved in at least two processes; (1) formational process of composition trend and (2) assimilation of materials with isotopic compositions different from the Kutsugata magma. The latter process is not significant enough to affect the composition trend of major elements. If not so, the compositional "area" would be produced rather than compositional "trend".

The linear composition trend of the magma could be produced either by a crystal fractionation or by a mixing between two end-component magmas. Zoning patterns of plagioclase and olivine cores in the Kutsugata lava can be explained solely by their transportation processes between the mushy boundary layer and the main magma body, and the crystals do not show any evidence for mixing with exotic magmas. If the magma mixing was the controlling mechanism, therefore, the crystals should have been formed *after* the compositional variation was produced. This point is the critical difference from the case of the crystal fractionation in which the crystals were grown *during* formation of the compositional variation. If the crystals would have formed after the compositional variation was produced, it is expected that the compositions of crystals show systematic variation with the whole-rock composition as observed in the main phenocrysts (Figs. 2-11, 2-15, and 2-18), because they crystallized *in situ* from the magma with compositional diversity. However, the composition of the Type-A olivine cores is sporadically dispersed within the compositional range of the North lava, for example (Fig. 2-16). From this the crystal fractionation is considered to have played dominant role for the formation of the compositional diversity of the Kutsugata magma. In addition, it might be difficult to make scattered patterns of the $^{206}Pb/^{204}Pb$ ratio (Fig. 2-5) by assimilation, after the compositional variation was established by magma mixing. On the contrary the $^{206}Pb/^{204}Pb$ ratio could have varied randomly in the case of the crystal fractionation, if the exotic materials with various $^{206}Pb/^{204}Pb$ ratio was assimilated during formation of the compositional variation of the magma.

2-7-2. Crystal fractionation of the Kutsugata magma

It is obvious from the isotopic data that the Kutsugata magma chamber was not closed, but the observed compositional variation of the Kutsugata lava (Fig. 2-3) was produced principally by fractional crystallization (separation of minerals) in a magma chamber. The amount of the exotic materials is shown to have been negligible for the composition trends of major elements in the later section (Section 2-8).

The whole-rock composition *trend* records information on amounts of separated minerals and their chemical compositions. In order to know fractionation processes of the Kutsugata-lava magma, compositions of fractionated mineral phases, as well as their weight fractions, are

Table 2-6. Parent, Daughter, and Calculated Compositions of Crystal-Fractionation Calculations

	North lava			South lava I			South lava II		
	Parent (1σ)	Daughter (1σ)	Calculated	Parent (1σ)	Daughter (1σ)	Calculated	Parent (1σ)	Daughter (1σ)	Calculated
SiO_2	51.37 (0.03)	51.81 (0.06)	51.81	52.16 (0.06)	52.50 (0.04)	52.50	52.60 (0.06)	53.07 (0.07)	53.07
TiO_2	1.37 (0.04)	1.42 (0.06)	1.44	1.39 (0.06)	1.40 (0.02)	1.45	1.41 (0.04)	1.47 (0.03)	1.51
Al_2O_3	18.01 (0.23)	17.86 (0.32)	17.81	18.02 (0.27)	17.72 (0.25)	17.72	17.67 (0.25)	17.23 (0.23)	17.04
Fe_2O_3	8.59 (0.18)	8.62 (0.24)	8.58	8.55 (0.29)	8.67 (0.12)	8.63	8.67 (0.17)	8.98 (0.17)	9.05
MnO	0.14 (0.00)	0.15 (0.00)	0.15	0.15 (0.00)	0.15 (0.01)	0.15	0.15 (0.00)	0.16 (0.00)	0.16
MgO	5.79 (0.14)	5.40 (0.17)	5.34	5.17 (0.16)	5.08 (0.08)	4.93	4.94 (0.11)	4.96 (0.04)	4.89
CaO	9.72 (0.09)	9.65 (0.08)	9.63	9.31 (0.08)	9.24 (0.06)	9.18	9.19 (0.10)	8.70 (0.16)	8.73
Na_2O	4.15 (0.20)	4.18 (0.12)	4.28	4.31 (0.06)	4.21 (0.11)	4.39	4.33 (0.11)	4.33 (0.15)	4.42
K_2O	0.58 (0.02)	0.62 (0.03)	0.61	0.65 (0.02)	0.72 (0.01)	0.68	0.75 (0.02)	0.77 (0.03)	0.80
P_2O_5	0.28 (0.01)	0.30 (0.01)	0.30	0.29 (0.01)	0.31 (0.01)	0.31	0.30 (0.01)	0.34 (0.02)	0.33
Ni, ppm	55 (3)	44 (3)	44	34 (4)	28 (4)	28	28 (2)	24 (2)	24
Sr, ppm	415 (8)	419 (9)	416	428 (8)	432 (6)	428	430 (6)	419 (6)	422

Numbers in parantheses indicate standard deviations of the average compositions of 5 samples.

estimated with a least-squares method modified from the method of *Bryan et al.* (1969). The estimation of fractionated mineral composition is possible because major-element compositions of, for example, plagioclase, vary significantly not only in CaO and Na_2O contents, but also in SiO_2 and Al_2O_3 contents. The method was applied to the three linear composition trends in the Kutsugata lava, corresponding to that of the North lava, South lava I, and South lava II (Fig. 2-3).

Parent and daughter magmas are represented by the average compositions of the 5 least and most differentiated samples in each lava, respectively (Table 2-6). Compositional trends of the individual lavas are modeled by using whole-rock major elements, and Ni and Sr. Significance of all composition trends in individual lavas is not rejected by 10 % two-sided test, though that of some composition trends in the South lava I, such as Fe_2O_3 and Na_2O, is somewhat doubtful because of the narrow range in the compositional variation. Olivine, plagioclase, and augite are selected as fractionated crystal phases, because they are the major phases of the Kutsugata magma system over a wide range of possible temperature variation. The unknown variables of the modeling are Mg# of olivine, An content of plagioclase, and weight fractions of removed olivine, plagioclase, and augite. The Mg# of augite is expressed as a function of the Mg# of olivine. Details of the fractionation modeling are described in the Appendix B.

The results of the calculation are shown in Table 2-7, and the calculated daughter composition is listed in Table 2-6. The composition trend of the North lava requires fractionation of a significant amount of plagioclase, together with olivine. The degree of olivine fractionation decreases from the North lava to the South lava II, and augite fractionation is significant in the South lava II. The Mg# of fractionated olivine is as low as 77, which does not vary significantly with the lavas. Though the estimated anorthite content of plagioclase has a relatively large uncertainty, it exceeds An80 throughout the Kutsugata lava. The Mg# of separated olivine is successfully estimated in the North-lava magma, in contrast to the relatively large uncertainty in the South lavas. This is also indicated by the lower χ^2 value and higher probability Q (*Press et al.*, 1992) of the North lava than the South lava I and II (Table 2-7). The slope of the MgO-SiO_2 variation diagram (Fig. 2-3) strongly constrains the estimation of the Mg# in the North lava, resulting in a small error. In the North lava and South lava I, the residual contours are elongated to the ordinate direction (Figs. B-1a and B-1b), indicating that the estimated Mg# is independent of the uncertainty of An content.

Table 2-7. Result of the Least-Squares Optimization of Crystal-Fractionation Modeling

	North lava				South lava I				South lava II			
	wt.%	(1σ)	composition	(1σ)	wt.%	(1σ)	composition	(1σ)	wt.%	(1σ)	composition	(1σ)
Olivine	1.77	(0.17)	Mg#77.1	(1.1)	1.16	(0.18)	Mg#75.9	(1.6)	0.72	(0.17)	Mg#77.1	(2.6)
Plagioclase	3.08	(0.41)	An89.1	(4.9)	3.23	(0.46)	An81.6	(4.4)	5.60	(0.41)	An83.2	(2.5)
Augite	0.00	(0.40)	-	(-)	0.00	(0.39)	-	(-)	0.54	(0.37)	Mg#82.5	(1.7)
χ^2	1.85				7.55				6.01			
Probability Q	0.967				0.375				0.540			

Probability Q represents a quantitative measure for the goodness-of-fit and is calculated from the χ^2 value at its minimum and the number of degrees of freedom (7) in least-squares optimization (*Press et al.*, 1992).

2-7-3. Boundary layer fractionation

As described above, the compositional diversity of the Kutsugata lava was suggested to have formed by crystal fractionation. In this section, the fractionation mechanism is considered on the basis of the results of least-squares fractionation modeling. One plausible mechanism is a homogeneous fractionation such that crystals formed homogeneously throughout the cooling magma chamber are separated from the magma by gravitational settling. In the case of the North-lava magma, only the Type-A olivine was stable at the estimated temperature of the main magma body. The compositional variations of the North lava, however, require separation of 3.1 wt.% plagioclase as well as 1.8 wt.% olivine. Therefore, separation of crystals from the main part of the reservoir was not the controlling mechanism of crystal fractionation during differentiation of the North-lava magma.

Another possibility is that the magma was differentiated by separation of crystals grown in the mushy boundary layer along the chamber walls. In the mushy layer of the magma chamber when the North-lava magma was present, plagioclase crystals (An-rich core) could grow because of lower temperature condition than in the main part of the reservoir in which only olivine was crystallizing. This conjecture is consistent with the estimated high An content of 89.1±4.9 of the removed plagioclase, which coincides with that of the An-rich core (~An90). Furthermore, the estimated Mg# of fractionated olivine (Mg#77.1) is significantly lower than the Mg# of the Type-A olivine (Mg#79-83), which is in accordance with the differentiated nature of the low-temperature

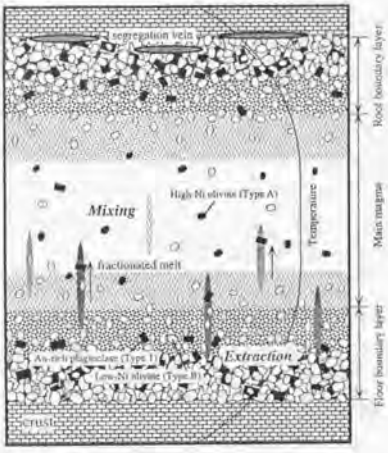

Figure2-22. Schematic illustration of the magma chamber during residence of the North-lava magma. The differentiation of the main magma is proceeded by mixing of fractionated interstitial melt extracted from the floor mush zone.

mush zone. The most plausible fractionation mechanism is extraction of a fractionated interstitial melt from the mush zone and its subsequent mixing with the main magma (Fig. 2-22). The interstitial melt was in equilibrium with the lower-temperature phases, such as low-Mg# olivine and plagioclase, than that of the main magma. Mixing of the melt with the main magma is therefore equivalent to the fractionation of sub-liquidus phases from the main magma (boundary layer fractionation; e.g., *Langmuir,* 1989). In the later section, it is shown that this view is supported by a numerical simulation of magmatic differentiation including boundary layer fractionation. Though the magma with whole-rock composition of the North-lava samples can coexist with Mg#85-86 olivine (after *Roeder and Emslie,* 1970), the magma was actually differentiated by fractionation of olivine with a much lower Mg# of 77.

During chamber residence of the South-lava magma, Ab-rich core plagioclase was present in the main magma body, together with An-rich core plagioclase in the mushy boundary layer. The anorthite content of more albitic cores in the South lava I ranges from An57 to An67, and that of the South lava II from An55 to An61 (Fig. 2-10), which are significantly lower than that of the anorthitic cores (An70-90). The estimated anorthite content of the separated plagioclase is An81.6±4.4 in the South lava I and An83.2±2.5 in the South lava II. Even if the uncertainty is taken into account, these results suggest more significant fractionation of the An-rich core than the Ab-rich core during differentiation of the South-lava magma. Thus, the compositional variation of the South lava is also suggested to have been produced principally by boundary layer fractionation rather than settling of crystals grown in the main magma body.

2-7-4. Differential information of boundary layer processes

The boundary-layer processes are constrained better from the differential information extracted from the North lava, in which crystal fractionation modeling is more successful. The composition trend of the North lava can be explained by separation of plagioclase and olivine. The compositional variation of the North-lava magma was established by two-component mixing between the parent magma and the averaged differentiated melt. The latter was in equilibrium with the fractionated olivine and plagioclase, because the composition of the residual melt (and average composition of the fractionated phases) was on the linear extrapolation from the whole-rock composition trends. The averaged differentiated melt in the boundary layer should have been in equilibrium with Mg#77.1±1.1 olivine, therefore, its composition can be specified by assuming the Fe-Mg exchange coefficient of 0.3 (*Roeder and Emslie,* 1970) and by using the ferric-ferrous ratio after *Kobayashi et al.* (1987).

Estimated chemical and physical parameters of the averaged differentiated melt (ADM) are shown in Table 2-8 compared with those of the least and most differentiated samples in the North lava (Fm-17 and Ta-26, respectively). The average temperature of the melt is obtained by

Table 2-8. Chemical and Physical Paramaters of the Differentiated Melt Comparing with Those of the Least and Most Differentiated Samples in the North Lava

Sample	Fm-17	Ta-26	ADM	(1σ)
SiO_2 wt.%	51.4	51.7	54.3	(0.2)
MgO wt.%	5.80	5.49	3.2	(0.2)
K_2O wt.%	0.57	0.58	0.9	(0.02)
Mg# of olivine	86.3	84.8	77.1	(1.1)
Density (kg/m^3)	2470	2460	2360	
Temperature (°C)	1110	1100	1010	

ADM denotes the averaged differentiated melt. Mg# of olivine indicates the equilibrium value with the melt composition. Temperature for the sample Fm-17 and Ta26 is obtained in the later section.

using olivine-silicate melt thermodynamic equilibria as described above, and the density is calculated after *Lange and Carmichael* (1990). The average temperature of 1010 °C is significantly lower than the temperature of the main magma of 1100-1110 °C (Table 2-8), supporting the view that the differentiated melt was derived from the low-temperature boundary layer of the reservoir. The calculated density of 2360 kg/m^3 is less than that of the equilibrium crystal phases (olivine and plagioclase) and the main magma.

A mushy boundary layer can develop along marginal parts of the reservoir, such as the roof, floor, and sidewall, however, it is not likely that the roof boundary layer is the main source of the differentiated melt. This is because the low-density differentiated melt may not mix effectively with the underlying denser main magma. The light interstitial melt in the roof mush zone may accumulate and form segregation veins (Fig. 2-22), as observed in the Hawaiian lava lakes (*Helz,* 1980). Fractionated melt is also produced in the sidewall boundary layer. It may ascend along the vertical walls and collect at the roof of the reservoir, forming a separate magma layer from the underlying main magma (*McBirney et al.,* 1985). This stable compositional stratification again prevents from effective mixing of the main magma with the differentiated melt in the magma chamber. These magmas would mix during eruption and compositional variation could be formed. However, this is against the observation that the abundance of crystals originated from the main magma (Type-A olivine) tends to increase with bulk SiO_2 content, though the abundances of crystals derived from differentiated melt (An-rich plagioclase and Type-B olivine) are fairly uniform throughout the North lava (Table 2-4). From this, it is concluded that the main site of formation of the differentiated melt is a floor boundary layer. The low-density fractionated melt from the floor mush zone would mix effectively with the overlying main magma, causing differentiation of the main magma (Fig. 2-22). In Kilauea Iki lava lake, Hawaii, light differentiated melt was suggested to have transported from the floor mush zone as diapirs (*Helz et al.,* 1989). Such melt transport is also observed in analogue experiments using aqueous solutions (*Tait and Jaupart,* 1992; *Chen,* 1995).

Interstitial melt is extracted from the floor boundary layer by mechanisms such as compaction (e.g., *Shirley,* 1987; *McBirney,* 1995) and compositional convection (e.g., *Chen and Turner,* 1980; *Tait and Jaupart,* 1992), due to the large density contrast among the residual melt, crystals, and the main magma. The average crystallinity of the mush zone from which the residual melt was derived can be constrained. Because the whole-rock composition of the overall mush zone was similar to or less differentiated than that of the parent magma by releasing evolved melt, the averaged differentiated melt should have coexisted with >31±2 wt.% crystals by mass balance calculation, namely more than about 30 vol.% (after *Berman,* 1988; *Lange and Carmichael,* 1990). This crystallinity compares to 33 vol.% for the Holyoke flood-basalt flow (*Philpotts et al.,* 1996) and 28 vol.% for the Watchung flows of New Jersey (*Puffer and Horter,* 1993), which were estimated from composition of the segregated melt from the floor mush zone during solidification of thick lava flows.

In the main magma body, minor amounts (< 0.5 vol.%) of crystals originating from the mush zone were present (plagioclase of the An-rich core, olivine of the Type-B core). Most of the crystals may have been transported by convective plumes from the floor boundary layer, as discussed above. Crystals could be settled from the roof boundary layer because of the density contrast with the melt. However, they are likely to have been captured by the solidification front encroaching from above (*Mangan and Marsh,* 1992). Minimum upward velocity of the convective current from the floor mush zone is calculated according to Stokes' law. Given the viscosity of the differentiated melt of $10^{1.2}$ Pa s (*Bottinga and Weill,* 1972; *Shaw,* 1972) and the density contrast between the melt and olivine, spherical olivine crystals with a diameter of 0.5 mm can be transported by a plume if the upward velocity is more than 4 cm/h.

2-8. Assimilation of Crustal Materials

The evolution of the Kutsugata magma was proceeded by minor mixing processes with exotic materials, as well as by crystal fractionation, as suggested from the variation of isotopic ratios such as $^{87}Sr/^{86}Sr$ and $^{206}Pb/^{204}Pb$ with the whole-rock SiO_2 content (Fig. 2-5). Any evidence for mixing with exotic magmas, such as newly injection of magmas, is not observed in the lava, and thus the materials with different isotopic compositions are considered to have derived from the surrounding crust. The nature of the exotic materials and its contribution to the evolution of the Kutsugata magma system is discussed.

2-8-1. Assimilation of partial melt from the crust

The features of the exotic materials are well constrained from the concentration of incompatible trace elements. Figure 2-23a shows the concentration of the sample Km-11 (the most differentiated sample in the Kutsugata lava) normalized by the value of the sample Fm-57 (the least differentiated sample) (with filled circles). The concentration of the trace elements of the daughter magma, which is expected from the crystal fractionation from the Fm-57 magma, is also calculated (with open circles in Fig. 2-23a) on the basis of the result of the crystal fractionation modeling (Table 2-7). Mineral-melt partition coefficients determined in basaltic systems were used for the calculation, and are listed in Table 2-9. Figure 2-23b shows the difference of the normalized concentration of the Km-6 from that modeled by crystal fractionation. The Km-11 is enriched in highly incompatible trace elements including light rare earth elements (LREE) compared with the daughter concentration calculated by the crystal-fractionation model. The positive spike of Pb is remarkable. These enrichments are explained by assimilation of exotic materials from outside the magma chamber. The addition of highly incompatible elements is consistent with the fact that LREE are preferentially partitioned into aqueous fluid or melt phase in comparison with heavy rare earth elements (HREE) (*Tatsumi et al.*, 1986; *Bau*, 1991). The negative spike of Sr is well explained by crystal fractionation, mainly by separation of plagioclase. The depletion of HREE is considered to reflect the boundary layer fractionation of hornblende, which was not included in the separated crystal phases for the crystal-fractionation modeling discussed in the Section 2-7. Additional fractionation of 2~3 wt.% of hornblende can account for the depletion of HREE according to the partition coefficients of e.g. *Sisson* (1994).

Li, B, and Pb have been considered to be more partitioned in aqueous fluid than the elements of similar incompatibility such as Y, Nb, and Ce, respectively, during magmatic processes (e.g., *Ishikawa and Nakamura*, 1994; *Kogiso et al.*, 1997; *Moriguti and Nakamura*, 1998). Significant enrichment of Pb and Li relative to Ce and Y indicates that the materials derived from the surrounding crust was strongly related to the fluid phase. This is also suggested from the variation of the isotopic compositions. The isotopic compositions of Sr and Pb vary with the whole-rock composition, whereas the $^{143}Nd/^{144}Nd$ ratio is mostly homogeneous throughout the lava within the analytical uncertainty. Sr is likely to be partitioned in aqueous fluid, similar to Pb (e.g., *Shibata and Nakamura*, 1997), on the contrary Nd is not soluble in the fluid phase. In addition to the fluid phase, melt phase is also required to be involved in the exotic materials. This is because the concentration of Nb is increased as well as that of B (Fig. 2-23), which cannot be explained only by the assimilation of the fluid phase. Most plausible form of assimilated materials is, therefore, a melt phase in which H_2O-rich fluid is significantly dissolved.

Temperature profiles of the magma chamber and the surrounding crust by heat conduction are roughly calculated for the Kutsugata magma system. It is assumed that initial temperature of the magma is 1110 °C (temperature of the Fm-57 magma) and that of the surrounding crust is uniform at 200 °C (typical geotherm at 2 kbar), and the thickness of the magma chamber is 1 km (Fig. 2-24). The thermal diffusivity of 8×10^{-3} cm^2s^{-1} is used (*Huppert and Sparks*, 1988).

The solidus of the crust is about 600 °C for granite, 700 °C for granodiorite, 750 °C for tonalite, and 800 °C for gabbro (e.g., *Naney*, 1983; *Kaneko and Koyaguchi*, 1996). If the assumption of initial crust temperature of 200 °C is correct, the crust surrounding the magma chamber must be granitic because partial melting of the crust might not occur in other compositions than the granite at 2 kbar. Even if the initial crust temperature of 300 °C is assumed, the temperature at the crust-magma interface could not reach 750 °C.

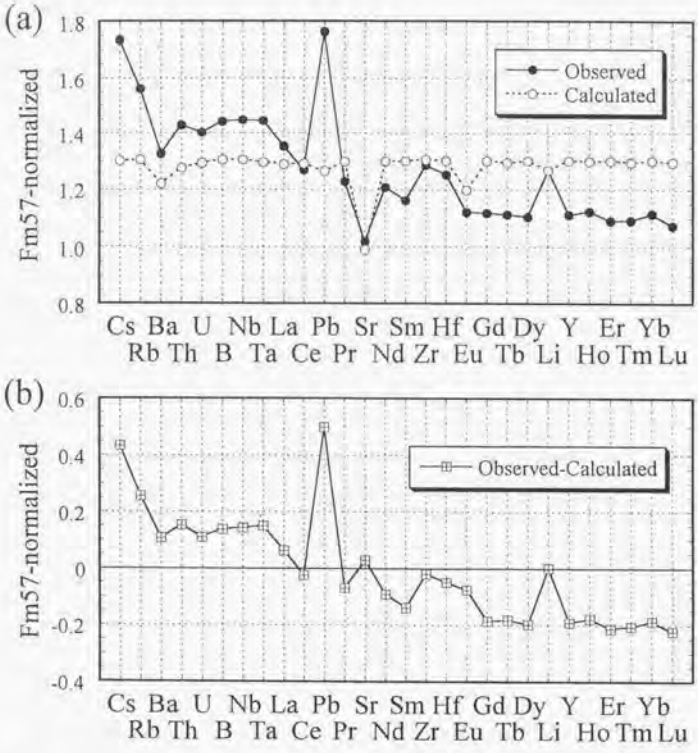

Figure 2-23. (a) Normalized concentration of the incompatible trace elements of the Km-11 as well as the daughter magma calculated on the basis of crystal-fractionation model and crystal/melt partition coefficient listed in Table 2-9. The difference of the normalized concentration between the Km-11 and the daughter magma is shown in (b).

Table 2-9. Mineral/Melt Partition Coefficients along with Parent Composition (Fm-57), Actual Dauter Composition (Km-11), and Calculated Daughter Composition

	Partition Coefficients						Parent	Daughter	
	olivine	ref	augite	ref	plagioclase	ref	Fm-57	Km-11	Calculated
Cs	0.01	1	0.02	1	0.022	2	0.50	0.86	0.65
Rb	0.001	2	0.05	1	0.008	2	13.3	20.8	17.4
Ba	0.01	1	0.02	1	0.38	2	132	175	161
Th	0.022	2	0.02	1	0.13	2	1.66	2.36	2.11
U	0.04	2	0.02	1	0.051	2	0.47	0.65	0.60
B	0.0016	*	0.036	4	0.008	*	4.10	5.90	5.35
Nb	0.0016	2	0.001	5	0.008	2	4.04	5.85	5.28
Ta	0.065	2	0.004	5	0.027	2	0.31	0.44	0.40
La	0.01	1	0.03	5	0.075	2	12.0	16.2	15.5
Ce	0.0038	2	0.041	5	0.062	2	29.7	37.7	38.4
Pb	0.0076	2	0.072	4	0.18	2	2.42	4.27	3.06
Pr	0.002	2	0.04	6	0.035	2	3.91	4.80	5.07
Sr	0.008	2	0.052	5	1.4	2	421	428	416
Nd	0.0093	2	0.112	5	0.026	2	17.7	21.3	23.0
Sm	0.0065	2	0.201	5	0.017	2	4.28	4.97	5.57
Zr	0.01	1	0.059	5	0.0009	2	161	206	210
Hf	0.01	1	0.006	5	0.02	1	3.45	4.31	4.49
Eu	0.0057	2	0.2	6	0.48	2	1.52	1.70	1.82
Gd	0.005	2	0.2	6	0.016	2	4.73	5.28	6.16
Tb	0.008	2	0.3	6	0.04	2	0.82	0.92	1.07
Dy	0.014	2	0.28	5	0.011	2	5.15	5.68	6.70
Li	0.41	2	0.59	4	0.023	2	7.04	8.93	8.93
Y	0.018	2	0.29	5	0.01	2	31.8	35.3	41.4
Ho	0.018	2	0.3	6	0.01	2	1.09	1.22	1.41
Er	0.026	2	0.3	6	0.005	2	2.95	3.21	3.84
Tm	0.009	3	0.2	6	0.036	7	0.46	0.50	0.59
Yb	0.038	2	0.255	5	0.004	2	3.09	3.44	4.02
Lu	0.11	2	0.1	6	0.0069	8	0.46	0.49	0.59

Ref. source are: 1, *Villemant* (1988); 2, *Dunn and Sen* (1994); 3, *Frey* (1969); 4, *Hart and Dunn* (1993); 5, *Skulski et al.* (1994); 6, *Irving and Frey* (1984); 7, *McKenzie and O'Nions* (1991); 8, *Bindeman et al.* (1998); *, estimation from partition coefficients of similarly incompatible elements.

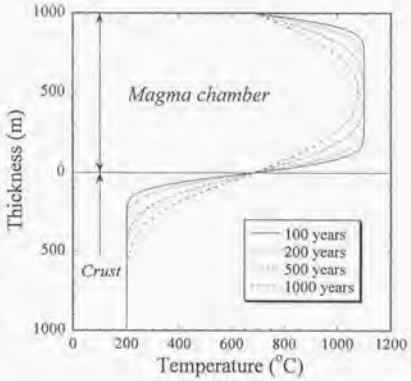

Figure 2-24. Temperature profiles of the magma chamber and the surrounding crust by assuming heat conduction model. The temperature of the crust cannot be high enough to cause partial melting unless the crust is granitic composition.

2-8-2. Degree of assimilation

The contribution of the assimilation of the crustal materials to the evolution of the Kutsugata magma is evaluated. The crust surrounding the magma chamber is assumed to have a composition of representative granite given by *Johannes and Holtz* (1996). The highly incompatible trace elements might be present in the grain boundaries of the granite, judging from the very low crystal/melt partition coefficients except for Rb, Ba, and Nb in biotite and Ba in K-feldspar (Table 2-10). The concentrations in partial melt of granite are calculated for some degrees of melting (1, 5, and 10 %; Table 2-10).

The amount of the partial melt transported to the magma chamber during differentiation of the Kutsugata magma (51.3~53.2 wt.% in SiO_2) can be calculated for each element (Table 2-10) by using the discrepancy of the concentration in the Km-6 from that expected from the crystal fractionation (Fig. 2-23b). If the degree of melting is 1 %, assimilation of 0.01~0.04 wt.% of the partial melt can account for the enrichment of the incompatible elements in the Km-11 magma. Similarly, assimilation of 0.1~0.2 wt.% and 0.1~0.4 wt.% is obtained for the degree of melting of 5 % and 10 %, respectively (Note that the amount of crystals fractionated from the Fm-57 magma to the Km-11 magma is about 30 wt.%.). Considering that the temperature of the crust could not rise much from the solidus temperature (Fig. 2-24), the degree of melting of the crust must have been fairly low. Therefore, it is concluded that the amount of the melt assimilated

Table 2-10. Parameters and Results of the Modeling for Estimating the Degree of Assimilation

	Rb	Ba	Th	U	Nb	Pb
			Observed and Calculated (ppm)			
Km-11	20.8	175	2.4	0.7	5.8	4.3
Calculated	17.4	161	2.1	0.6	5.3	3.1
			Representative Granite (ppm)			
Granite*	245	440	19	5	13	27
			Partial Melt in Granite (ppm)			
Degree of melting						
1%	24500	44000	1900	500	1300	2700
5%	4900	8800	380	100	260	540
10%	2450	4400	190	50	130	270
			Amounts of Assimilation (wt.%)			
Degree of melting						
1%	0.01	0.03	0.01	0.02	0.04	0.04
5%	0.07	0.16	0.07	0.10	0.21	0.22
10%	0.14	0.33	0.14	0.20	0.42	0.43
			Partition Coefficient			
K-feldspar	0.21	1.70	0.02	0.04	0.01	0.12
(ref)	(9)	(9)	(10)	(10)	(9)	(9)
Plagioclase	0.02	0.28	0.05	0.05	0.26	0.35
(ref)	(9)	(9)	(11)	(11)	(9)	(9)
Biotite	2.46	6.40	0.27	0.46	4.60	0.21
(ref)	(9)	(9)	(11)	(11)	(9)	(9)

*Composition of representative granite is after *Johannes and Holtz* (1996). Ref. Source are: 9, *Ewart and Griffin* (1994); 10, *Stix and Gorton* (1990); 11, *Nash and Crecraft* (1985); 12, *Schnetzler and Philpotts* (1970).

to the Kutsugata magma was not significant, and the assimilation did not affect the evolution of the major elements in the Kutsugata magma.

The $^{206}Pb/^{204}Pb$ ratio varies randomly, and the $^{207}Pb/^{204}Pb$ and $^{208}Pb/^{204}Pb$ ratios tend to increase with an increase of the whole-rock SiO_2 content (Fig. 2-5). The variation of the lead isotope composition may have resulted from its heterogeneity in the crust. The excess Pb in the assimilated melt was originated partly from the dissolved fluid phase and partly from Pb present in the grain boundaries, which could also have derived from original solidification process and from metasomatism by the fluid phase. Therefore the isotopic composition of lead could vary significantly even in the small length scale within the crust. The variation of the $^{87}Sr/^{86}Sr$ ratio may also have reflected this mechanism. On the other hand the $^{143}Nd/^{144}Nd$ ratio, which was not affected by the metasomatism, was mostly homogeneous in the crust.

2-9. Origin of Phenocryst of the Kutsugata Lava

Volcanic rocks commonly contain various amounts of coarse-grained minerals, *phenocrysts*, and magma chambers are widely recognized as a principal formation sites for phenocrysts. Magmatic temperature within the chamber is commonly estimated from phenocryst compositions (e.g., *Druitt and Bacon,* 1989; *Feeley and Dungan,* 1996), and pressure conditions are constrained from crystallization experiments by reproducing observed phenocryst assemblages and their compositions (e.g., *Bartels et al.*, 1991; *Grove et al.,* 1992). It is also recognized, however, that crystallization occurs during ascent and eruption. Vesiculation during magma ascent leads to supersaturation of solid phases, which induces crystallization (e.g., *Anderson,* 1984; *Geschwind and Rutherford,* 1995). Though crystallization during ascent has been discussed in relation to eruption dynamics (*Lipman et al.*, 1985; *Geschwind and Rutherford,* 1995), such crystallization is commonly regarded as a minor process. In this section, it is shown that the main volume of phenocryst excluding the cores in the Kutsugata lava (>30 vol.%) crystallized during magma ascent. Factors responsible for the phenocryst formation of the Kutsugata magma are discussed, and crystallization styles of represented magma types during their ascent are inferred.

2-9-1. Temperature and water content conditions

The magmatic temperature of the Fm-17 magma was estimated to be 1110 °C by using olivine-silicate melt thermodynamic equilibria in the Section 2-5. This corresponds to the temperature just after eruption of the Fm-17 magma. In this section, magmatic temperature and water-content conditions of the Fm-17 magma during residence in the magma chamber are estimated.

Figure 2-25a shows the calculated liquidus phase diagram in pressure-water content space (*Ghiorso and Sack,* 1995) for the Ta-26 magma (Table 2-1) on the basis that the whole-rock compositions represent pre-eruption magma composition as discussed above. Because the sample Km-8 (Table 2-1), which has a slightly more differentiated composition than Ta-26, has a core of augite (Table 2-4), it can be inferred that the Ta-26 magma was in the olivine field near the boundary with the augite field in Fig. 2-25a (shaded area). The constraint that the pressure was more than 2 kbar is derived from the plagioclase-melt equilibria (Fig. 2-19). Though pressure and water content of the magma in the reservoir can not be specified independently, the magmatic temperature of Ta-26 is estimated to have been about 1100 °C.

A similar diagram for Fm-17 is displayed in Fig. 2-25b. The potential pre-eruption H_2O-P conditions of the Fm-17 magma, shown as a shaded area, was obtained from the shaded area of Ta-26 (Fig. 2-25a) multiplied by 0.96, which is the effect of crystal fractionation of 4

wt.% between Fm-17 and Ta-26. The magma with composition of Fm-17 was hydrous, with H_2O more than 4 wt.%, and had a temperature of about 1115 °C (Fig. 2-25b) at a pressure above 2 kbar.

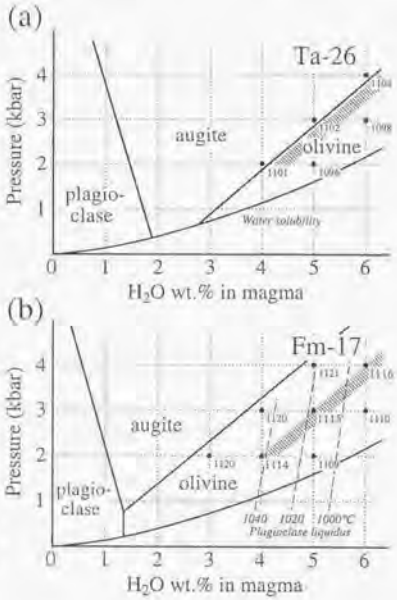

Figure 2-25. Calculated liquidus surfaces in pressure-H_2O space for the samples Ta-26 (a) and Fm-17 (b) after *Ghiorso and Sack* (1995). Shaded areas indicate plausible pressure-H_2O conditions of the magma in the magma chamber located at depth of more than 2 kbar. Numbers in (a) and (b) show the liquidus temperatures of individual conditions. Projected liquidus temperatures of plagioclase are shown with dashed lines.

2-9-2. Crystallization mechanism of phenocrysts

Cooling of magma chambers

One plausible mechanism to cause crystallization of a magma is reduction in temperature. In a magma reservoir, the magma is cooled through formation of a mushy boundary layer along the chamber wall, in which temperatures are below the liquidus temperature of the crystal-free interior liquid (e.g., *Marsh*, 1996). Porphyritic magmas are produced there (e.g., *Brophy*, 1991), because large crystals can grow over relatively long periods of time.

The Kutsugata magma chamber was inferred to have been located at a pressure more than 2 kbar. At 2 kbar, the liquidus temperature of plagioclase, which is projected on the H_2O-P diagram in Fig. 2-25b, is about 1040 °C. If the chamber was located at a pressure higher than 2 kbar, the inferred water content of the magma should also increase in order to satisfy the condition shown in Fig. 2-25b. The increase of water drastically depresses the plagioclase liquidus, which offsets the increase of liquidus due to pressure increase, and the liquidus temperature of plagioclase in the Kutsugata magma chamber is below 1040 °C at any pressure condition above 2

kbar (Fig. 2-25b). When the magma was tapped from the Kutsugata magma chamber and moved upward, the plagioclase liquidus gradually decreased until water saturation. The liquidus temperature of plagioclase, however, remained less than 1040 °C because of the effect of pressure reduction.

The magma might have been stored in a shallower reservoir during ascent. Crystallization of the main phenocrysts may have taken place by cooling of magma in such a chamber. However, this conjecture is shown to be disproved. Plagioclase could not appear in the main part of such a reservoir, if it is located below the level where vesiculation initiated, because the average temperature of the Fm-17 magma was more than 1110 °C and the plagioclase liquidus did not exceed 1040 °C. Therefore, the main phenocrysts should have been formed as cumulate piles along the chamber walls in which the temperature was below 1040 °C, and the observed rocks are the mixtures of the hot crystal-poor main magma and the cool cumulate piles. Though some phenocrysts form crystal aggregates, many phenocrysts are present as isolated grains, suggesting that they should have been derived from a mush zone where crystallinity was below ~50 vol.%. In this case, temperature of the erupted Fm-17 magma with >30 vol.% crystallinity should have been below 1070 °C, much lower than the estimated temperature of 1110 °C. Further, if the observed rocks are the mixtures, there should not be a systematic relationship between whole-rock and phenocryst compositions.

Decompression during magma ascent

Crystallization of phenocrysts in the Kutsugata lava requires another driving force. The most plausible one is decompression above the water-saturation condition during magma ascent. When a hydrous magma moves upward through a conduit, decrease of water solubility in the melt leads to water saturation of the magma. Further ascent causes vapor exsolution and the magma is successively supersaturated with solid phases due to increase in liquidus temperatures. This process explains well the following points: (1) the small difference of the estimated temperatures between magma residing in the chamber and after eruption (1115 vs. 1110 °C), suggesting nearly adiabatic ascent; and (2) the systematic relationship between phenocryst and whole-rock composition (Figs. 2-11 and 2-18), suggesting *in situ* growth of phenocrysts within magma batches with individual bulk compositions. In the following section, it is shown that morphologies and textures of phenocrysts are consistent with this inference as well.

2-9-3. Rapid growth of phenocrysts

Plagioclase

The most remarkable textural feature of plagioclase phenocrysts is that crystals have various amount of glass inclusions, from those free from glass inclusions to those exhibiting honeycomb texture, although the chemical compositions of these crystals fall in a narrow range within individual samples (Fig. 2-11). This implies that these plagioclases grew in the same environment during the same interval of time. The characteristics of honeycomb texture are similar to those described by *Kawamoto* (1992), who concluded that such texture was formed by skeletal growth under a supersaturated condition rather than by a dissolution process. In fact, the size and distribution of glass inclusions are quite different from those of plagioclase formed by partial dissolution experiments, which is characterized by very fine (~10 μm) glass inclusions (e.g., *Tsuchiyama,* 1985).

Although oscillatory zoning, one of the characteristics of the glass inclusion-poor plagioclase, has not been successfully reproduced by crystallization experiments, it has been commonly thought to reflect diffusion-controlled processes during growth (*Pearce and Kolisnik,* 1990; *L'Heureux and Fowler,* 1994; *Brophy et al.,* 1996). This is consistent with formation of oscillatory zoning by rapid growth (*Anderson,* 1984; *Singer et al.,* 1993).

Plagioclase phenocrysts with various amount of glass inclusions, excluding cores, are inferred to have grown at a relatively high rate. In the cooling experiments by *Lofgren* (1980), tabular plagioclase with few glass inclusions was gradually changed into skeletal crystals with abundant inclusions as the degree of supersaturation increased. Therefore, plagioclase phenocrysts in the Kutsugata lava may reflect various degrees of supersaturation during their growth, and those richer in glass inclusions are suggested to have crystallized under higher degrees of supersaturation.

Olivine

Olivine phenocrysts also show various crystal morphologies. Skeletal olivine has been thought to grow rapidly under supersaturated conditions. Mg#, Ni, and Ca contents in skeletal olivine are identical to those of euhedral crystal within the same samples, which negates the possibility that skeletal morphology was formed by dissolution process. *Donaldson* (1976) conducted cooling experiments and showed that skeletal olivine similar to that found in the Kutsugata lava (Fig. 2-15) was reproduced at a higher cooling rate than olivine with euhedral outline. Skeletal olivine crystals were also found in pillows of ocean floor basalt, and they were interpreted to have grown during eruption (e.g., *Dungan and Rhodes*, 1978). Therefore, olivine phenocrysts with various amounts of glass inclusions in the Kutsugata lava may reflect different degrees of supersaturation during their growth, similar to plagioclase phenocrysts.

Augite

Augite phenocrysts in the Kutsugata lava commonly develop strong oscillatory zoning. Sector zoning is also occasionally superimposed on the oscillatory zoning (Fig. 2-17). Although zoning is a relatively common feature of augite in volcanic rocks, sector zoning may be favored by rapid growth, in which structural control and growth rate vary between different growing surfaces (*Smith and Lofgren*, 1983; *Deer et al.*, 1978). The presence of abundant glass, olivine, and plagioclase inclusions also supports a high growth rate for augite phenocrysts.

2-9-4. Crystallization history of phenocrysts during magma ascent

Figure 2-26 shows the inferred crystallization history for the Fm-17 magma during ascent, assuming an initial Kutsugata magma chamber at 2 kbar. Equilibrium liquidus temperatures of phenocryst phases and the water content of the magma after *Ghiorso and Sack* (1995) are also shown (Fig. 2-26c). Because the Fm-17 magma is suggested to have had 4 wt.% water at 2 kbar (Fig. 2-25b), water saturation is achieved at a pressure of about 1 kbar (Fig. 2-26b). If the inferred pressure condition of the reservoir is more than 2 kbar, the magma is saturated with water at deeper levels than 1 kbar. Furthermore, it is well known that a fair amount of CO_2 may dissolve in basaltic magma, and this may also cause vapor-saturation at deeper levels. However, this may not drastically affect the phase relations under water-saturated condition shown in Fig. 2-26c.

When the magma ascends from the reservoir to the surface adiabatically, the temperature decreases by about 5 °C (*Berman*, 1988; *Lange and Carmichael*, 1990). Ignoring the latent heat of crystallization, the P-T path is linearly approximated from 1115 °C at 2 kbar to 1110 °C at 1 bar in Fig. 2-26c. In the equilibrium case, the liquidus temperature of olivine decreases slightly until water saturation at about 1 kbar, and olivine crystallization is suppressed or insignificant. Whether crystallization takes place or not depends on the slope of magmatic temperature and liquidus temperature (Fig. 2-26c). Once the magma is saturated with water, olivine starts to grow due to an increase in its liquidus temperature caused by water exsolution. When the magma ascends to a shallower level, augite and plagioclase appear as liquidus phases (Fig. 2-26c).

A potential drawback to this equilibrium model is that phenocrysts of augite are absent

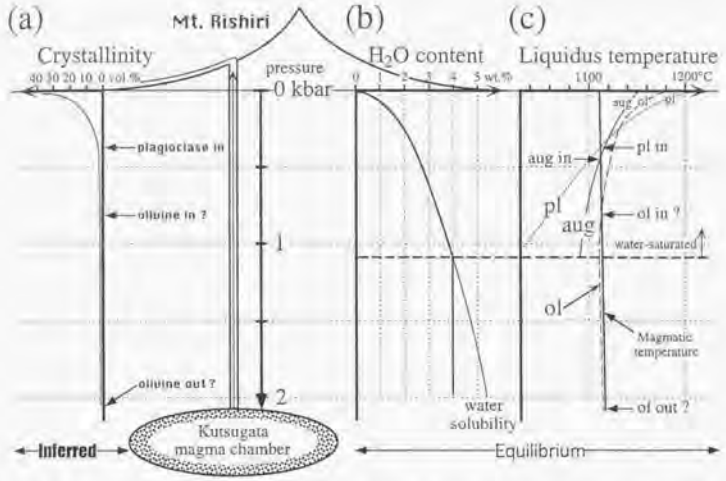

Figure 2-26. Crystallization history of the Kutsugata magma (sample; Fm-17). (a) Inferred variation of crystallinity during ascent. (b), (c); Water solubility (b) and liquidus phase diagram (c), showing equilibrium case after *Ghiorso and Sack* (1995). In (c), P-T path is linearly approximated from 1115 to 1110 °C. Liquidus temperature of each phase is shown by different pattern. Abbreviations; ol: olivine; pl: plagioclase; aug: augite.

in the Fm-17 sample (Table 2-4). Assuming the calculated phase relations are accurate, this can be explained by nucleation delay. In cooling experiments at an isobaric condition, it has been shown that initial superheating prior to supercooling significantly lowers the temperature at which nucleation first takes place in a supercooled melt, due to an increase in the activation energy for structural ordering of the complex mineral components in silicate melts (*Donaldson,* 1979; *Corrigan,* 1982). A similar phenomena might be expected to occur during ascent of a water-saturated magma, in which successive supersaturation is induced at a nearly isothermal condition. Unlike augite, plagioclase crystallization occurred during ascent, probably because of the presence of plagioclase cores (Table 2-4) as nuclei for crystallization. Furthermore, the equilibrium liquidus temperature of plagioclase rose significantly at a very shallow level compared with that of augite (Fig. 2-26c) and the driving force for crystallization was much greater. Although plagioclase phenocrysts are abundant, they crystallized at a very shallow level, less than 300 bar (~1 km). Because the An content of the outermost thin rim of the plagioclase phenocryst is similar to that of the quenched crystals in groundmass, insignificant growth of phenocrysts also took place during quenching after eruption.

The inference of the formation site of phenocrysts discussed above is based on the assumption that the magma ascended from the Kutsugata magma chamber to the surface at an appropriate rate. As will be discussed below, no crystallization should have taken place if the ascent velocity was too large. On the contrary, if the magma moved upward very slowly, or was stored in another reservoir at a shallower level than 1 kbar for a long time, equilibrium conditions would be nearly attained and augite crystallization should occur in the Fm-17 magma. Successive ascent of the Kutsugata magma may be supported by the homogeneous distribution of oscillatory

zoning throughout the inclusion-poor plagioclase (Fig. 2-8a) and augite phenocrysts (Fig. 2-17a). However, a detailed pressure-time path of the Kutsugata magma during ascent cannot be specified from only the observations and estimations described above.

2-9-5. Morphological diversity of phenocrysts

The observed diversity of the phenocrysts in the Kutsugata lava is suggested to have resulted from significant nucleation delay after the magma was saturated with phenocryst phases. The case of plagioclase is considered as an example. After saturation with plagioclase during magma ascent, crystal growth would selectively take place from the cores of plagioclase, and even those of other crystal phases (heterogeneous nucleation). As the magma ascended further and crystallization proceeded, the growth on the preexisting cores was not sufficient enough to decrease the degree of supersaturation. Due to the nucleation delay (*Corrigan*, 1982), however, homogeneous nucleation did not occur instantly. When the degree of supersaturation was further increased, homogeneous nucleation was initiated and plagioclase crystals with more abundant glass inclusions than those grown heterogeneously from the cores are inferred to have been formed. This inference explains well the following observations that the plagioclase cores are much less frequently observed in the glass inclusion-rich plagioclase crystals (Figs. 2-6c and 2-6d) than in the inclusion-poor ones (Figs. 2-6a and 2-6b), and that the inclusion-rich plagioclase rarely forms crystal aggregates, in contrast to the inclusion-poor ones (Table 2-5).

2-9-6. Controlling factors of phenocryst crystallization

The Kutsugata magma was nearly aphyric in the magma chamber, and its porphyritic feature was formed during ascent, as discussed in the previous sections. However, aphyric volcanic rocks are commonly present as well as porphyritic rocks, suggesting that some magmas were not subjected to effective crystallization during ascent. It is suggested below that (1) the degree of undercooling during ascent, (2) the magma ascent rate, and (3) the degree of superheating in the magma chamber, control phenocryst crystallization during magma ascent.

Degree of undercooling during magma ascent

The Kutsugata magma was hydrous with more than 4 wt.% in H_2O in the magma chamber (Fig. 2-25b). The liquidus temperatures of phenocryst phases, especially plagioclase and pyroxene, are significantly depressed by addition of water under isobaric conditions. Furthermore, vesiculation of water-richer magma initiates at a deeper level. These factors increase the degree of undercooling during ascent, that is, the difference between the equilibrium liquidus temperature and the actual one (*Kirkpatrick*, 1981), and lead to larger degree of supersaturation of solid phases in a magma. Thus, a higher water content of a magma in a relatively deep reservoir produce a larger driving force for crystallization during ascent to the surface.

Magma ascent rate

The effusion rate of the Kutsugata lava is suggested to have been low. The lava shows typical pahoehoe morphology, without evidence for explosive eruption. Low melt viscosity due to basaltic composition with high bulk-Na and H_2O contents allowed a vapor phase to segregate easily, which may result in non-explosive, slow ascent of the magma. *Geschwind and Rutherford* (1995) conducted isothermal decompression experiments and showed that crystallization is enhanced at lower decompression rates. Therefore, extensive crystallization may have occurred during ascent of the Kutsugata magma. The growth rate of crystals is also suggested to have been high because of low-melt viscosity.

Degree of superheating in the magma chamber

Although more than 20 vol.% of plagioclase was formed during ascent in the 1980 eruption of Mount St. Helens, as in the case of the Kutsugata lava, crystallization was characterized by a high population density of plagioclase microlites up to 30 μm in size (*Geschwind and Rutherford,* 1995). The Kutsugata lava is characterized by large plagioclase phenocrysts up to 5 mm long with low population density, though some phenocrysts overgrew preexisting cores. This may have resulted from the difference in the degree of superheating of plagioclase before ascent, apart from the large difference in melt composition. In the case of Mount St. Helens, equilibrium plagioclase was already present (*Geschwind and Rutherford,* 1995) and the degree of superheating was zero or even negative throughout the magma chamber. In the Kutsugata lava, in contrast, the equilibrium plagioclase liquidus temperature of the Fm-17 magma in the magma chamber was less than 1040 °C, much lower than the estimated magmatic temperature of 1115 °C, i.e. more than 70 °C of superheating.

Figure 2-27 shows the result of crystallization experiments at 1 atm to examine the effect of initial superheating on nucleation of plagioclase, as was done by *Sato* (1995). Starting materials are the powdered sample of the Km-8 (Table 2-1) and that of the Kk-5 (SiO_2 58.4 wt.%; Table 3-1 in the Chapter 3). Temperature was set at the degree of superheating of 30 °C (1240 °C for Km-8 and 1210 °C for Kk-5) and 5 °C (1215 °C for Km-8 and 1185 °C for Kk-5) for 5 hours, and was decreased rapidly (~1 hour) below the liquidus value (1180 °C for Km-8 and 1150 °C for

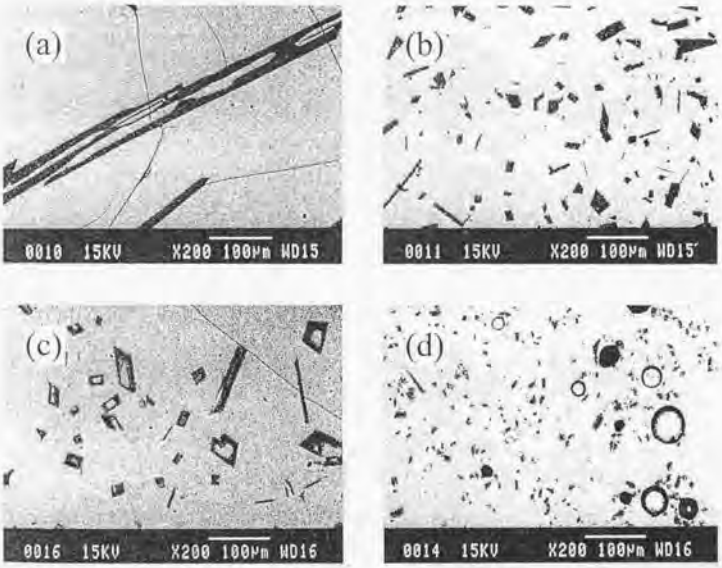

Figure 2-27. Back-scattered electron images showing the result of the crystallization experiments to examine the effect of initial superheating on the population density and size distributions of crystals. (a) initial superheating of 30 °C for the sample Km-8; (b) initial superheating of 5 °C for the sample Km-8; (c) initial superheating of 30 °C for the sample Kk-5 (Tanetomi lava); and (d) initial superheating of 5 °C for the sample Kk-5.

Kk-5), in which crystallization was induced at isothermal condition (~ 3 days). In both the basaltic (Figs. 2-28a and 2-28b) and andesitic (Figs. 2-28c and 2-28d) compositions, a larger degree of superheating results in a lower population density of crystals with larger size, and *vice versa*. As demonstrated by *Sato* (1995), therefore, the degree of initial superheating mostly determines the population density and size distribution of crystals of the succeeding crystallization. A similar mechanism is considered to have operated during decompression of the magma, and limited numbers of large crystals were formed instead of abundant fine-grained microlites.

2-9-7. Crystallization styles during ascent of magmas

The main factors responsible for phenocryst formation during ascent of the Kutsugata magma are suggested to have been ascent rate, degree of undercooling during ascent, and degree of superheating in the magma chamber before ascent. These conditions can vary with magma types, such as tholeiitic basalt and alkali basalt. Possible crystallization styles of representative magma types during ascent are considered, assuming that the three factors listed above principally govern the crystallization styles.

Figure 2-28 compares schematic phase diagrams of low-H_2O basaltic magma, such as a tholeiitic basalt (a), high-H_2O basaltic magma, such as an alkali basalt of the Kutsugata lava (b),

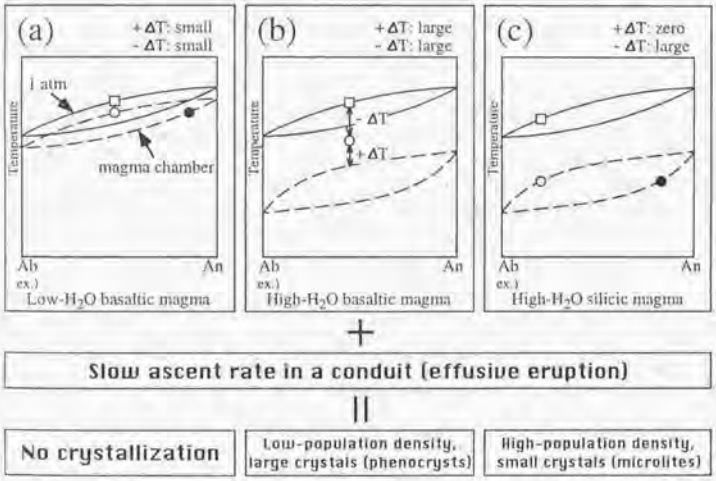

Figure 2-28. Schematic albite-anorthite diagrams for low-H_2O basaltic magma (a), high-H_2O basaltic magma (b), and high-H_2O silicic magma (c), showing inferred crystallization styles of plagioclase during ascent. Conditions of the degree of undercooling at 1 atm ($-\Delta T$) and superheating in a chamber ($+\Delta T$) for each magma type are also shown. Loop with solid lines is for 1-atm condition and that with broken lines is for condition in the magma chamber before ascent. Open squares indicate 1-atm plagioclase liquidus of magmas. Open and solid circles in (a) and (c) are liquidus and solidus, respectively, of magmas in the reservoir. Open circle in (b) shows temperature and composition of a magma which is not saturated with plagioclase. Expected crystallization styles of magmas which ascend at proper rate are shown below.

and high-H_2O silicic magma, such as a dacite of Mount St. Helens (c). A crystallizing phase during ascent is represented by plagioclase. Of the three factors, the magma ascent rate is treated independently. This is because no crystallization may take place during ascent of any magma types if the ascent velocity is too fast.

The degree of undercooling, the difference between the actual temperature and the equilibrium liquidus temperature, is represented by the value at 1 atm because this is the maximum degree during ascent. Variation of liquidus temperature of plagioclase at 1 atm is limited for basalt to dacite, commonly between 1150~1250 °C. Therefore, the degree of undercooling at 1 atm is primarily determined by the temperature in the magma chamber, assuming that the temperature is essentially constant during ascent.

Contrary to the equilibrium liquidus temperatures at 1 atm, those of magmas in magma chambers vary significantly with magma types, especially depending on their water contents. Hence the degree of superheating depends on both magmatic temperature and liquidus temperature in the magma chamber.

In the case of the low-H_2O basaltic magma (Fig. 2-28a), the position of the plagioclase loop in a chamber is close to that of 1 atm, because of the low-H_2O content and high magmatic temperature. If the water content is fairly low, the loop is placed above the loop at 1 atm due to the pressure effect. In any case, however, the magma is not saturated with water until a very shallow level is reached during ascent. Furthermore, the degree of undercooling, that is, the driving force of crystallization, is not large (Fig. 2-28a). If the effect of nucleation delay is taken into account, no crystallization may take place unless the ascent rate is quite low.

In the case of the high-H_2O basaltic magma (Fig. 2-28b), the plagioclase loop for the magma chamber is significantly suppressed to lower temperature due to the high water content. The liquidus temperatures of any other phases are also lowered to some extent. Because a magma superheated above its liquidus tends to decrease in temperature rapidly until saturation of one phase (e.g., *Brandeis and Marsh,* 1989), the high-H_2O basaltic magma is likely to be saturated with one or more phase(s) at relatively low temperature (olivine; in the case of the Kutsugata lava). Therefore, the magmatic temperature is placed between the plagioclase loop at 1 atm and the loop for the higher-pressure magma chamber (Fig. 2-28b), and the magma satisfies the condition of a high degree of undercooling and high degree of superheating. If this magma rises at a relatively slow rate, these conditions induce crystallization with low-population density and large-crystal size (phenocrysts).

In the case of the high-H_2O silicic magma (Fig. 2-28c), the plagioclase loop for the chamber is at low temperature because of the high water content. The magmatic temperature is also low due to the magma's evolved nature, and the magma is saturated with plagioclase throughout the magma chamber (degree of superheating is zero). Because of the low magmatic temperature, the degree of undercooling is large when H_2O exsolves and is lost. If the magma ascends slowly, crystallization with high-population density and small-crystal size (microlites) is expected to occur.

3. Constraints from the Tanetomi Lava

The Tanetomi lava forms fairly smooth composition trend, and mineral assemblage and chemical composition vary systematically with the whole-rock composition. Unlike the Kutsugata lava, the Tanetomi lava shows evidence for replenishment of a basaltic magma. In this chapter, mechanism of magma mixing and its relevant to the trigger of eruption is discussed in detail, in addition to the mechanism of crystal fractionation during differentiation of the Tanetomi magma.

3-1. Geologic Setting

The Tanetomi lava is a trachytic andesite erupted from the western flank of the volcano (Fig. 2-1), with a volume of about 0.1 km^3. It overlies directly the Kutsugata lava dated at 37,000 years B.P. (*Miura and Takaoka*, 1993), without any clear hiatus. The lava consists of two main flow units with several tens of meters in thickness (*Ishizuka*, 1999), called Lower and Upper lavas in this paper (Fig. 3-1). The Upper lava directly overlies the Lower lava. No air-fall and pyroclastic-flow deposits are found throughout the Tanetomi lava.

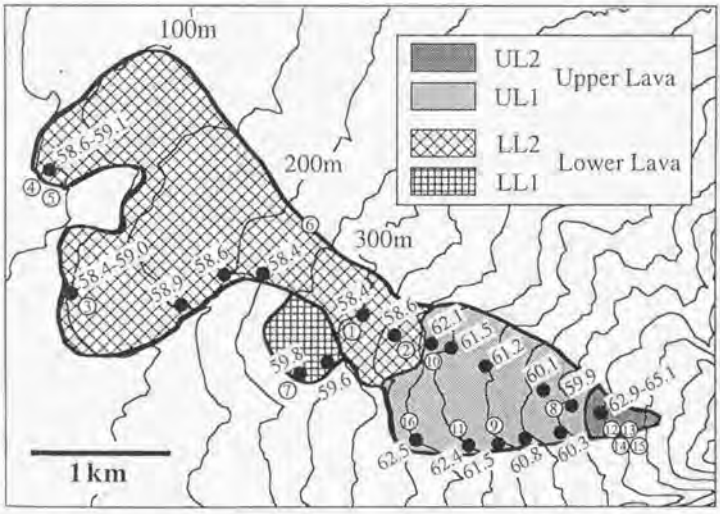

Figure 3-1. Geologic map of the Tanetomi lava showing representative sampling localities. Numbers by the localities indicate whole-rock SiO_2 content of the samples. SiO_2 content is recalculated for the total weight to be 100 %. Numbers with circle are those listed in Table 3-1.

3-2. Whole-Rock Compositions

3-2-1. Major and trace elements

Representative whole-rock major and trace element contents are listed in Table 3-1 for samples numbered in Fig. 3-1. Figure 3-2 shows Harker variation diagrams for selected major element oxides (TiO_2, MgO, CaO, Na_2O, K_2O, and P_2O_5) and trace elements (Ba and Sr) plotted against SiO_2 content. The division of the Tanetomi lava into Lower and Upper lavas is consistent with their whole-rock compositions: the SiO_2 content of the Lower-lava samples is less than 59.8 wt.% and that of the Upper-lava samples is more than 59.9 wt.% (Fig. 3-2). The variation diagrams of some oxides such as TiO_2 and MgO allow us to subdivide the Lower lava into more and less differentiated groups. These are referred to as LL1 (Lower Lava 1; SiO_2 >59.1 wt.%) and LL2 (Lower Lava 2; SiO_2 <59.1 wt.%), respectively. The small lava flow, budding out from beneath the main flow at 300 m above the sea level, corresponds to the LL1 (Fig. 3-1). Field relations suggest that the LL1 is overlain by the LL2.

Table 3-1. Whole Rock Major and Trace Element Compositions of Representative Samples from the Tanetomi Lava

	Lower Lava							Upper Lava							
	LL2					LL1		UL1				UL2			
	1	2	3	4	5	6	7	8	9	10	11	12	13	14	15
	Kk-5	Kk-8	Ta-21	Ta-12	Ta-14	Bi-8	Kr-74	Kk-22	Kr-72	Kk-11	Kr-56	Kr-64	Kr-51	Kr-47	Kk-31
Whole Rock Composition, Major Elements (wt.%)															
SiO_2	57.86	57.72	58.24	58.59	58.21	58.02	58.64	58.26	60.23	60.95	61.29	61.64	61.90	62.61	63.60
TiO_2	1.07	1.09	1.07	1.07	1.05	0.99	0.94	0.88	0.79	0.75	0.72	0.70	0.68	0.63	0.57
Al_2O_3	17.94	17.58	17.72	17.69	17.64	17.59	17.60	17.72	17.60	17.54	17.40	17.35	17.37	17.28	17.04
Fe_2O_3	7.12	7.04	6.96	7.08	6.87	6.73	6.39	6.17	5.60	5.42	5.19	5.06	4.92	4.50	4.04
MnO	0.15	0.15	0.15	0.15	0.14	0.15	0.14	0.14	0.14	0.14	0.13	0.13	0.13	0.13	0.13
MgO	2.38	2.39	2.37	2.39	2.29	2.13	2.04	1.92	1.65	1.57	1.51	1.46	1.40	1.26	1.09
CaO	5.42	5.46	5.47	5.49	5.41	5.26	5.10	4.99	4.57	4.42	4.36	4.24	4.16	3.83	3.48
Na_2O	5.47	5.34	5.50	5.43	5.46	5.42	5.36	5.40	5.49	5.51	5.55	5.48	5.58	5.59	5.72
K_2O	1.25	1.28	1.27	1.29	1.30	1.32	1.36	1.34	1.49	1.54	1.57	1.60	1.63	1.72	1.82
P_2O_5	0.48	0.47	0.47	0.46	0.47	0.47	0.45	0.45	0.41	0.39	0.37	0.35	0.33	0.30	0.25
Total	99.14	98.51	99.21	99.63	98.84	98.07	98.01	97.28	97.96	98.22	98.09	98.02	98.10	97.85	97.74
Whole Rock Composition, Trace Elements (ppm)															
Ba	233	249	231	241	229	239	248	255	266	285	278	294	292	316	325
Cr	3.3	5.0	3.6	3.1	6.0	0.5	1.6	2.8	0.0	2.4	0.0	0.0	0.0	0.0	0.0
Nb	7.5	7.5	7.3	7.4	7.3	7.5	8.1	8.0	8.2	8.4	8.5	8.5	8.5	8.9	9.1
Ni	0.1	0.5	0.5	0.0	1.0	0.0	0.0	0.3	0.0	0.9	0.0	0.0	0.0	0.1	1.1
Pb	6.5	4.2	5.2	3.6	5.7	4.6	6.1	6.0	5.4	5.1	6.0	6.4	6.6	7.6	7.5
Rb	28.6	30.0	30.0	29.9	29.6	29.8	32.2	30.8	36.2	37.0	39.2	40.0	41.0	43.8	46.6
Sr	454	450	462	458	457	450	456	457	442	438	441	439	432	422	398
Th	5.3	4.8	5.2	3.2	4.8	3.7	4.6	4.3	5.3	5.7	5.7	5.5	5.7	6.0	5.1
Y	26.1	25.9	27.0	26.6	26.8	24.9	26.0	24.9	24.3	23.0	23.8	23.5	22.7	22.3	21.3
Zr	306	301	306	306	305	315	322	328	338	339	344	348	350	361	368

Sampling localities are shown in Fig. 3-1. Fe_2O_3 is total Fe as Fe_2O_3.

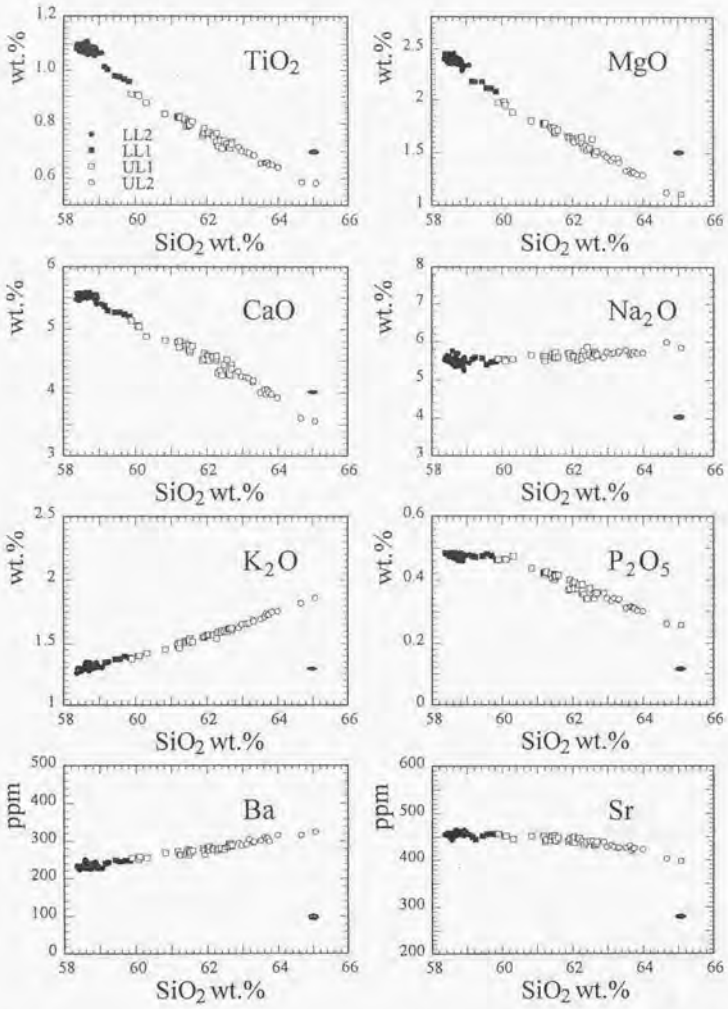

Figure 3-2. SiO_2 variation diagrams for some major oxides (TiO_2, MgO, CaO, Na_2O, K_2O, and P_2O_5) and trace elements (Ba and Sr) from the Tanetomi lava. Major element analyses are normalized to 100 wt.%. Analytical error (2σ) for both SiO_2 and the element of the ordinate is shown by ellipse filled with gray pattern.

Table 3-2. Whole Rock Trace Element Composition of Representative Samples Obtained by ICP-MS

	Lower Lava				Upper Lava					
	LL2		LL1		UL1			UL2		
	1	4	6	7	8	9	11	12	14	15
	Kk-5	Ta-12	Bi-8	Kr-74	Kk-22	Kr-72	Kr-56	Kr-64	Kr-47	Kk-31
	Whole Rock Composition, Trace Elements (ppm)									
Cs	0.48	0.78	1.48	1.39	1.48	1.83	1.94	1.97	2.11	2.32
Rb	31.7	33.0	33.8	36.0	34.5	43.1	44.2	45.0	48.7	52.1
Ba	290	293	311	307	310	345	355	365	382	430
Th	3.65	3.75	3.90	4.15	4.22	4.62	4.91	5.17	5.18	5.51
U	1.06	1.12	1.15	1.20	1.22	1.38	1.42	1.44	1.53	1.68
B	5.93	7.97	9.74	9.98	9.70	11.1	11.6	11.4	12.1	12.8
Nb	7.69	8.15	8.36	7.89	8.31	8.69	9.15	9.33	9.33	9.75
Ta	0.60	0.61	0.64	0.61	0.66	0.67	0.73	0.75	0.76	0.76
La	24.9	25.7	25.9	26.7	27.3	28.1	28.7	29.4	29.9	30.7
Ce	55.0	56.2	57.4	59.2	59.9	60.3	61.0	60.8	62.2	63.6
Pb	4.92	5.32	5.52	5.87	6.01	6.30	6.66	6.83	6.99	7.68
Pr	6.68	6.96	6.92	6.81	7.43	6.98	6.96	7.15	6.92	6.87
Sr	479	492	478	481	487	474	467	455	456	434
Nd	27.2	28.5	28.1	28.5	28.8	27.4	28.0	27.6	27.7	27.3
Sm	5.98	5.94	5.75	5.90	5.44	5.07	5.39	5.46	5.34	5.05
Zr	314	302	293	303	325	294	322	335	325	341
Hf	5.43	5.73	5.54	5.56	5.71	6.17	6.27	6.05	6.29	6.55
Eu	1.85	1.86	1.87	1.84	1.78	1.69	1.81	1.81	1.68	1.63
Gd	5.62	5.78	6.04	5.77	5.56	5.21	5.05	5.05	4.77	4.40
Tb	0.95	0.96	0.94	0.93	0.89	0.83	0.84	0.83	0.79	0.70
Dy	5.59	5.78	5.38	5.34	5.39	4.69	4.88	5.11	4.62	4.49
Li	12.2	10.7	14.2	14.1	14.6	17.0	17.3	17.7	18.6	19.8
Y	35.7	37.5	35.2	34.3	34.9	31.6	31.9	31.2	30.2	29.4
Ho	1.20	1.23	1.15	1.15	1.12	1.07	1.08	1.06	0.96	0.95
Er	3.19	3.37	3.23	3.17	3.10	2.91	2.96	2.86	2.66	2.76
Tm	0.51	0.52	0.50	0.47	0.49	0.47	0.49	0.47	0.44	0.44
Yb	3.62	3.68	3.33	3.47	3.56	3.61	3.56	3.39	3.31	3.19
Lu	0.54	0.54	0.52	0.54	0.53	0.50	0.51	0.51	0.51	0.50

Sampling localities are shown in Fig. 3-1.

The Upper-lava samples are also divided into two groups by the spatial distribution of whole-rock compositions. As the altitude of sampling locality increases, the SiO_2 content of the samples tends to decrease from 62.1 to 59.9 wt.%, and it abruptly increases to > 62.9 wt.% (Fig. 3-1). The less and more differentiated groups are referred to as UL1 (Upper Lava 1; SiO_2 <62.7 wt.%) and UL2 (Upper Lava 2; SiO_2 >62.9 wt.%), respectively. The order of eruption of the UL1 and UL2 is not clear. From these, the activity of the Tanetomi lava started with the eruption of the LL1, continued with the LL2, and ended with the eruption of the Upper lava.

The compositional trends of the overall Tanetomi lava are principally smooth, but those of the LL2 differ slightly from the main trends. For example, the Na_2O content of the LL2-samples decreases with an increase of SiO_2 content, though that of the overall Tanetomi lava

slightly increases with SiO_2 content. Some composition trends among the Upper lava samples exhibit a change in the slope at the boundary between the UL1 and UL2. The CaO and Sr contents of the UL1 decrease more gently than those of the UL2 as SiO_2 content increases.

Trace element compositions of whole rocks measured with ICP-MS are listed in Table 3-2 for representative samples of the Tanetomi lava. MORB-normalized diagram is shown in Fig. 3-3 wherein concentrations for the Kutsugata lava are compared. The concentration pattern of the Tanetomi lava is principally similar to that of the Kutsugata lava. The samples of the Tanetomi lava are enriched in highly incompatible trace elements compared with the N-type MORB. Significant negative Nb and Ta anomalies and positive Pb and Li anomalies are observed. A Sr anomaly is not significant in the Tanetomi lava in contrast to the Kutsugata lava. The HREE is slightly depleted compared with that of the Kutsugata lava.

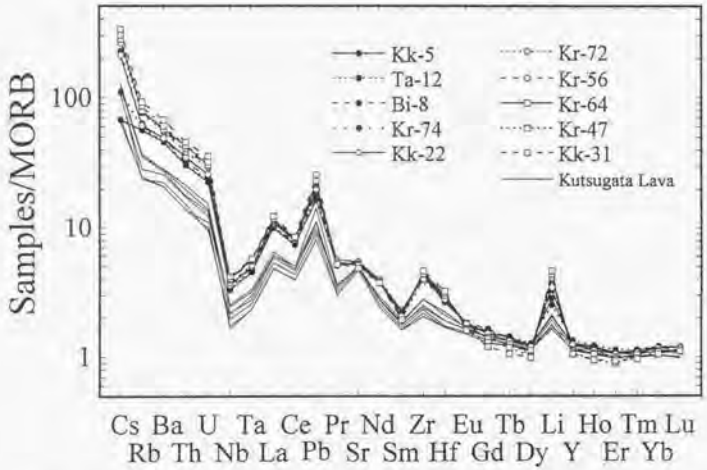

Figure 3-3. Concentration of incompatible trace elements of the Tanetomi lava, normalized by the values of MORB. That of the Kutsugata lava is also show for comparison.

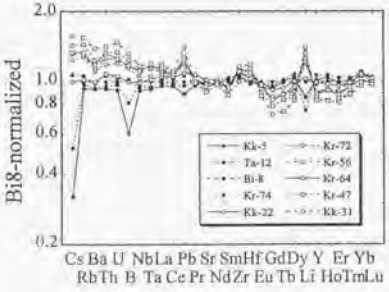

Figure 3-4. Concentration of incompatible trace elements of the Tanetomi lava, normalized by the values of the sample Bi-8. The Bi-8 is used for the normalization, because the LL2 shows evidence for mixing with replenished basalt magma.

Figure 3-4 shows the concentration of the incompatible trace elements normalized to the value of the sample Bi-8. Cs, B, Pb, and Li are highly enriched in the more differentiated samples. The LREE are slightly enriched in the more differentiated samples, but the HREE are depleted compared with the sample Bi-8.

3-2-2. Isotopic compositions

Sr, Nd, and Pb isotopic compositions of whole rocks are plotted against the SiO_2 content in Fig. 3-5, and are listed in Table 3-3. The $^{87}Sr/^{86}Sr$ ratio of the Upper lava is higher than that of the Lower lava. Among the Upper-lava samples, the UL1 has high $^{87}Sr/^{86}Sr$ ratio compared with the UL2. The $^{143}Nd/^{144}Nd$ ratio seems to decrease with an increase of the SiO_2 content, though the difference of the ratio between the most and least differentiated samples is below the range of the analytical reproducibility. The $^{206}Pb/^{204}Pb$, $^{207}Pb/^{204}Pb$, and $^{208}Pb/^{204}Pb$ ratios increase progressively with the whole-rock SiO_2 content.

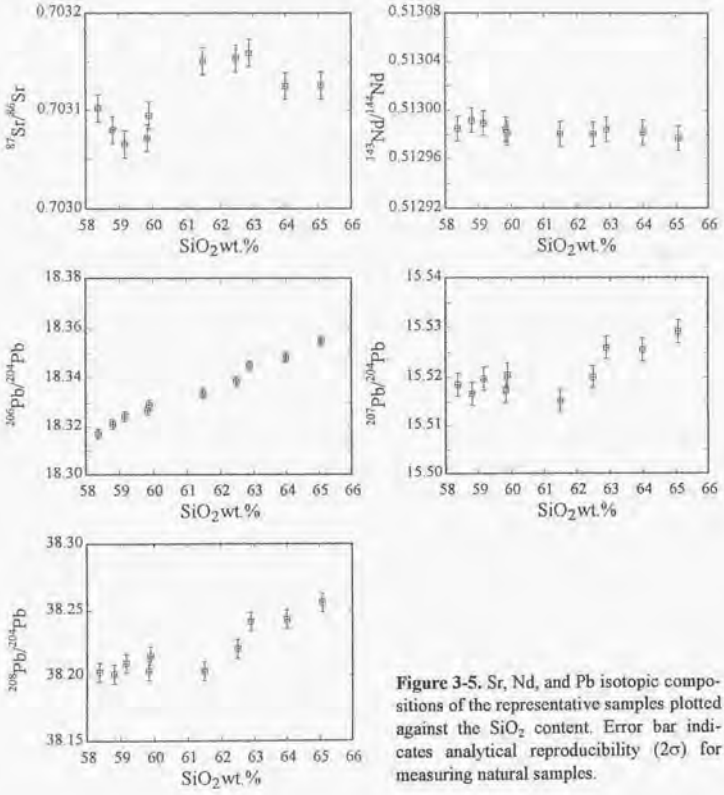

Figure 3-5. Sr, Nd, and Pb isotopic compositions of the representative samples plotted against the SiO_2 content. Error bar indicates analytical reproducibility (2σ) for measuring natural samples.

Table 3-3. Isotopic Compositions of the Representative Samples of the Tanetomi Lava

	$^{87}Sr/^{86}Sr$	$^{143}Nd/^{144}Nd$	$^{206}Pb/^{204}Pb$	$^{207}Pb/^{204}Pb$	$^{208}Pb/^{204}Pb$
Kk-5	0.703102±15	0.512985±02	18.3171±02	15.5185±01	38.2027±03
Ta-12	0.703080±16	0.512992±03	18.3211±02	15.5167±01	38.2012±03
Bi-8	0.703065±34	0.512989±02	18.3244±01	15.5197±01	38.2094±02
Kr-74	0.703071±23	0.512984±01	18.3271±01	15.5173±01	38.2039±03
kk-22	0.703095±17	0.512981±02	18.3292±02	15.5205±01	38.2152±03
Kr-72	0.703151±20	0.512981±01	18.3338±02	15.5152±01	38.2035±02
Kr-56	0.703154±12	0.512980±02	18.3388±03	15.5200±01	38.2205±05
Kr-64	0.703159±16	0.512984±02	18.3449±01	15.5260±01	38.2414±02
Kr-47	0.703125±19	0.512982±02	18.3484±02	15.5256±01	38.2432±03
Kk-31	0.703126±18	0.512977±01	18.3548±02	15.5292±01	38.2563±03

In-run analytical precision (2σ) is given for each data.

3-3. Petrography and Mineralogy

The Tanetomi lava is aphyric with total phenocryst contents generally less than 3 vol.% (Table 3-4). The phenocryst assemblage of the Lower lava is olivine, augite, orthopyroxene, pigeonite, hornblende, plagioclase, and titanomagnetite, and that of the Upper lava is hornblende, plagioclase, and titanomagnetite. These crystals are clearly divided into two groups by their sizes, and larger crystals are referred to as phenocryst and smaller crystals are as microphenocryst. The size of the crystals dividing phenocryst from microphenocryst is 0.5 mm for plagioclase and 0.2 mm for the other mineral phases. All orthopyroxene, pigeonite, and magnetite crystals occur as microphenocryst. Petrographic and mineralogical features of each mineral phase are described below.

Table 3-4. Modal Compositions of Representative Samples of the Tanetomi Lava

	Lower Lava					Upper Lava				
	LL2				LL1	UL1			UL2	
	1	2	3	5	7	8	9	10	13	15
	Kk-5	Kk-8	Ta-21	Ta-14	Kr-74	Kk-22	Kr-72	Kk-11	Kr-51	Kk-31
Modal Composition, Phenocryst (vol.%)										
Olivine	Tr.	Tr.	Tr.	Tr.	0.0	0.0	0.0	0.0	0.0	0.0
Plagioclase	0.3	Tr.	0.2	0.2	Tr.	Tr.	Tr.	0.0	Tr.	1.0
Augite	0.1	Tr.	0.1	0.1	0.0	0.0	0.0	0.0	0.0	0.0
Hornblende	Tr.	Tr.	Tr.	Tr.	Tr.	Tr.	0.1	Tr.	Tr.	Tr.
Modal Composition, Microphenocryst (vol.%)										
Olivine	Tr.	Tr.	Tr.	Tr.	0.0	0.0	0.0	0.0	0.0	0.0
Plagioclase	0.9	1.5	1.7	1.5	0.2	Tr.	Tr.	0.1	0.1	0.5
Augite	0.4	0.7	0.4	Tr.	Tr.	0.0	0.0	0.0	0.0	0.0
Orthopyroxene	Tr.	Tr.	Tr.	Tr.	Tr.	0.0	0.0	0.0	0.0	0.0
Pigeonite	Tr.	Tr.	Tr.	Tr.	0.0	0.0	0.0	0.0	0.0	0.0
Hornblende	Tr.	0.1	Tr.	Tr.	Tr.	Tr.	Tr.	0.1	0.1	0.3
Titanomagnetite	0.3	0.2	Tr.	0.1	Tr.	Tr.	Tr.	Tr.	Tr.	0.1
Groundmass	98.0	97.5	97.6	98.1	99.8	100.0	99.9	99.8	99.8	98.1

Modal composition is based on 2000 points/slide. Abbreviations: Tr., trace.

3-3-1. Plagioclase

All plagioclase phenocrysts and microphenocrysts have euhedral shape. Plagioclase microphenocrysts are commonly elongated. They are present abundantly in the Lower lava, especially in the LL2, but scarce in the Upper lava.

Microphenocryst shows clear feature under optical microscope and is composed of a clear region and surrounding sodic rim (Fig. 3-6a). Back-scattered electron image is shown in Fig. 3-7a. The clear region of the plagioclase microphenocrysts in the LL2 exhibits reverse zoning in An content (Fig. 3-8) and rarely shows sector zoning, whereas that of the LL1 and Upper lava is homogeneous. The An content of the clear region shows systematic spatial variation in the Tanetomi lava; from 54 to 64 in the LL2, from 55 to 61 in the LL1, from 50 to 58 in the UL1, and from 49 to 52 in the UL2 (Fig. 3-8). The An content of the sodic rim is equivalent to that of the groundmass plagioclase in each sample.

Plagioclase phenocryst can be divided into clear type (Fig. 3-6b), dissolved cored type (Fig. 3-6c), An-rich cored type (Fig. 3-6d), and Ab-rich cored type (Fig. 3-6e) on the basis of zoning patterns in An content. The clear-type plagioclase phenocryst shows clear feature under an optical microscope. It is composed of clear core, clear margin, and surrounding sodic rim (Figs. 3-6b and 3-7b), which can be discriminated by BEI (Fig. 3-7b). The clear type is very scar-

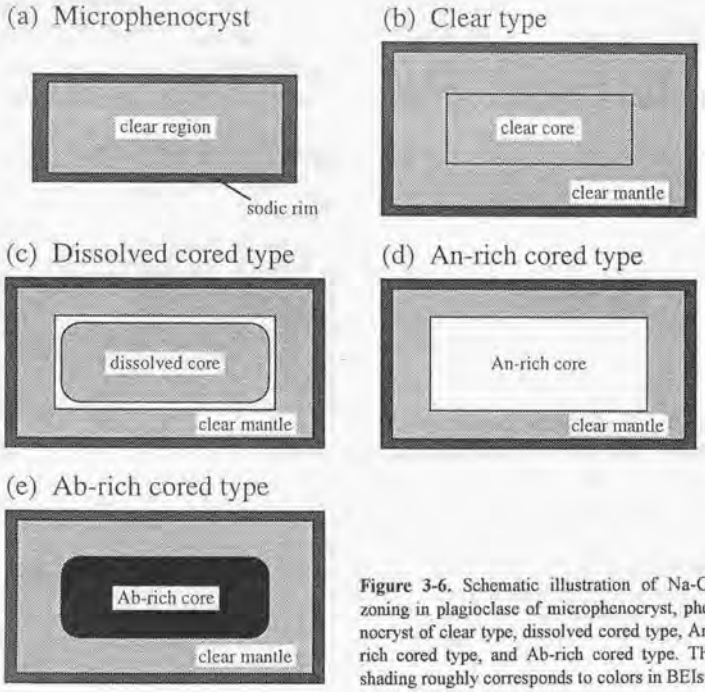

Figure 3-6. Schematic illustration of Na-Ca zoning in plagioclase of microphenocryst, phenocryst of clear type, dissolved cored type, An-rich cored type, and Ab-rich cored type. The shading roughly corresponds to colors in BEIs.

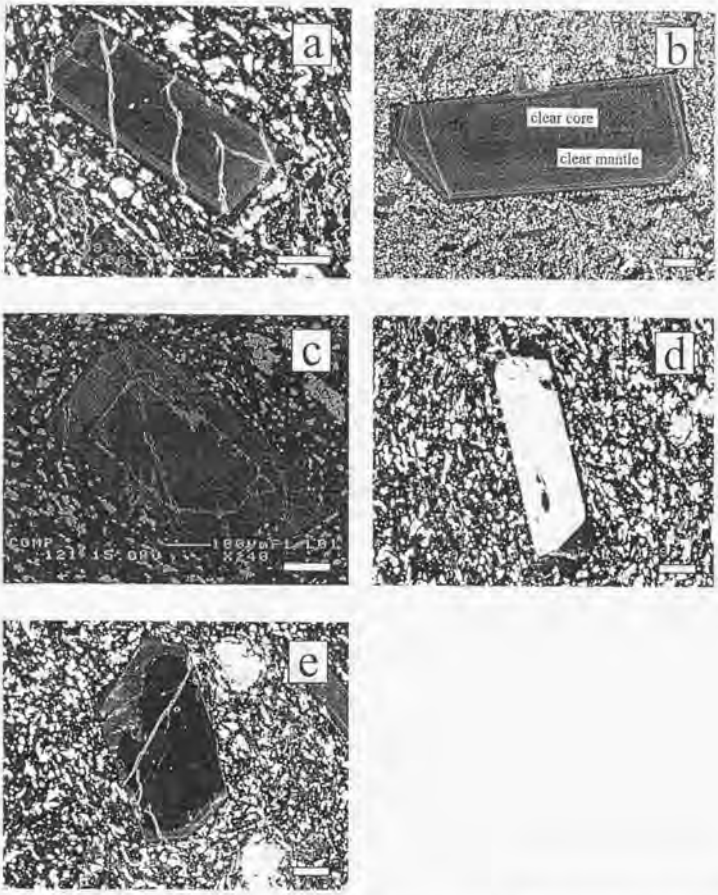

Figure 3-7. Back-scattered electron images of plagioclase crystals. (a) Pl 126-Ta14 (LL2; locality No. 4 in Fig. 3-1), microphenocryst plagioclase with oscillatory and sector zonings; (b) Pl 10-Kr10 (UL2; locality No. 12 in Fig. 3-1), clear-type plagioclase with homogeneous clear core and oscillatory-zoned clear mantle, which is surrounded by a sodic rim; (c) Pl 55-Ta14 (LL2; locality No. 4 in Fig. 3-1), dissolved cored type plagioclase, composed of a core with partial dissolution texture, surrounded by a clear mantle and further by a sodic rim; (d) Pl 15-Kk2 (LL2; locality No. 1 in Fig. 3-1), An-rich cored plagioclase, showing An-rich core surrounded by a clear mantle; (e) Pl 3-Kk2 (LL2; locality No. 1 in Fig. 3-1), Ab-rich cored plagioclase, which consists of a partially-dissolved Ab-rich core, surrounded by a clear mantle and further by a sodic rim. The horizontal black scale bar is 100 μm in length.

ce in the Lower lava, on the other hand it is common in the Upper lava (Table 3-5). The clear core is apparently homogeneous and is mostly free from oscillatory zoning, in contrast to the clear mantle which commonly exhibits strong oscillatory zoning as in the case of the clear region in the plagioclase microphenocryst. In spite of the difference of textural features, the An content of the clear mantle and clear core is mostly similar. In individual samples, the An content of the clear-type plagioclase coincides with that of the microphenocryst, showing spatial variation in the Tanetomi lava. No clear-type plagioclase phenocryst forms crystal aggregates with other phenocryst phases.

The dissolved cored type is characterized by the presence of a core with partial dissolution texture (e.g., *Tsuchiyama,* 1985; *Nakamura and Shimakita,* 1998), which is surrounded by a clear mantle and sodic rim (Figs. 3-6c and 3-7c). It occurs only in the Lower lava, especially in the LL2 (Table 3-5). The An content of the partial dissolution texture ranges from 65 to 70. The width of the texture is commonly less than 20 μm. The core inside the dissolution texture is homogeneous in composition. Its An content is similar to that of the clear mantle, which is also identical to the An content of the microphenocryst in the same samples. The clear mantle of this type in the LL2 samples shows reverse zoning.

The An-rich cored type has an An-rich core which is surrounded by a clear mantle, and further by a sodic rim (Figs. 3-6d and 3-7d). This type of plagioclase is present in the LL2. It scarcely occurs in the less differentiated samples in the LL1, and very rarely in the least differentiated samples in the UL1 (sample Kk-22 in Table 3-1) (Table 3-5). In the LL2, the An-rich cored types are frequently present in the SiO_2-rich sample than in the SiO_2-poor ones. The An content of the An-rich core ranges from 60 to 85, and does not show any spatial variation in the lava (Fig. 3-9). The An content of the clear mantle is similar to that of the clear region of the microphenocryst in each sample. The An-rich core is rarely in direct contact with Mg-rich olivine and augite phenocrysts.

The Ab-rich cored type is characterized by the presence of an Ab-rich core (Figs. 3-6e and 3-7e). This type occurs throughout the Tanetomi lava, and the abundance does not change spatially (Table 3-5). The Ab-rich core is rounded and has a texture characteristic of partial dissolution, but the width of the dissolution differs from crystal to crystal. The core commonly shows normal zoning in An content. The range of the An content of the core is from 20 to 50, which does not show specific spatial variation throughout the Tanetomi lava (Fig. 3-9). The Ab-rich core is directly surrounded by a clear mantle, whose An content is identical to that of the clear region in microphenocryst. The Ab-rich core commonly forms crystal aggregate with hornblende phenocryst and titanomagnetite, showing evidence for contemporaneous growth with them.

Table 3-5. Summary of the Abundance of Various Plagioclase Types along with That of the Other Phenocryst Phases

	LL2	LL1	UL1	UL2
		Plagioclase		
Clear type	Rare	Rare	Rare	Common
Dissolved cored type	Common	Rare	Absent	Absent
An-rich cored type	Common	Rare	Absent*	Absent
Ab-rich cored type	Common	Common	Common	Common
		Other phenocryst phases		
Olivine	Common	Rare	Absent	Absent
Augite	Common	Rare	Absent	Absent
Hornblende	Common	Common	Common	Common

*Note that the An-rich core is very rarely present in the least differentiated samples in the UL1

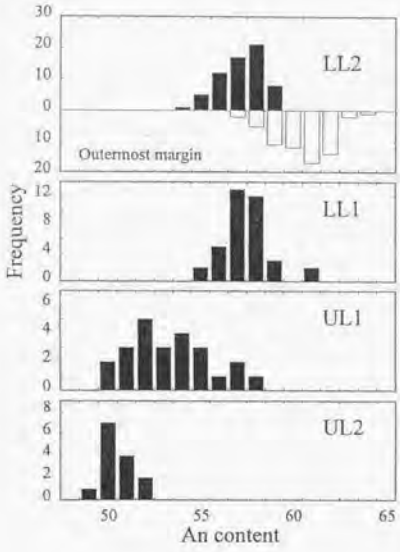

Figure 3-8. The histogram of An content of the clear region in plagioclase microphenocryst for individual lava flow units. The clear region of the microphenocrysts in the LL2 commonly shows reverse zoning, and therefore the An content at the outermost margin of the clear region is also shown.

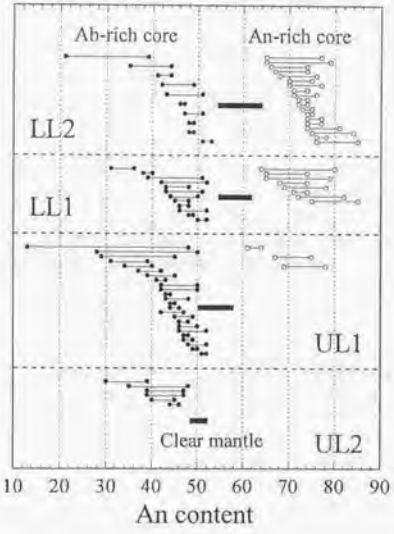

Figure 3-9. The range of the zonation of An content in both the individual Ab-rich and An-rich cores for each lava flow unit. That of the clear mantle in the Ab-rich and An-rich cored plagioclase is also shown with heavy line.

3-3-2. Olivine

Olivine phenocrysts, up to 2 mm in diameter, are commonly rounded. They rarely form crystal clots with augite phenocrysts. Olivine phenocrysts are common in the LL2 (Table 3-4), and are rarely present in the SiO_2-poor samples in the LL1. The olivine phenocrysts are more abundantly present in the SiO_2-rich samples than in the SiO_2-poor samples in the LL, as plagioclase of the An-rich cores. For example, 0.15 grains/cm^2 of olivine phenocrysts are observed (average of 10 thin sections) in the least differentiated sample in the LL2 (Kk-5 in Table 3-1), significantly lower than 0.35 grains/cm^2 in the most differentiated sample (Ta-14 in Table 3-1).

Olivine microphenocrysts are euhedral, up to 0.3 mm in size. They commonly form crystal aggregate with microphenocrysts of augite and titanomagnetite. The abundance of such crystal aggregates tends to decrease with the increase of SiO_2 content of the sample in the Lower lava. Crystal clots composed of olivine, plagioclase, and hornblende are rarely present.

Olivine phenocryst is discriminated clearly from olivine microphenocryst by their Mg# and NiO content at the core. The Mg# of the core of the olivine phenocrysts ranges from 81 to 84, on the other hand, that of microphenocrysts ranges from 64 to 75 (Fig. 3-10a). The NiO content in phenocrysts commonly exceeds 0.1 wt.%, in contrast to <0.08 wt.% in microphenocrysts. The phenocrysts are principally homogeneous in terms of Mg# and NiO content, but are strongly zoned at the margin of the crystals (Fig. 3-10b). Microphenocryst shows normal zoning in Mg# and NiO content, and the degree of zonation varies from crystals to crystals. Any significant correlation of the mineral compositions with the whole-rock composition of the host rocks is not found.

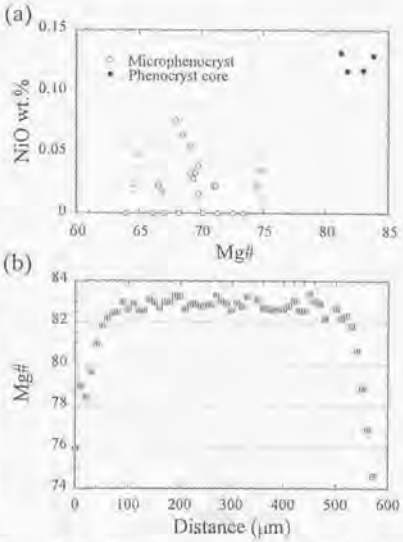

Figure 3-10. (a) NiO content of olivine crystals at the core plotted against the Mg#. The cores of olivine phenocrysts (filled circle) have higher Mg# and NiO content than microphenocrysts (open circle). (b) Line profile of Mg# in olivine phenocryst (ol 1-Ta19).

3-3-3. Pyroxenes

Augite phenocrysts are up to 2.5 mm in diameter. They are commonly rounded and rimmed with pigeonite. Augite microphenocrysts are euhedral, up to 0.3 mm in size. Microphenocrysts of orthopyroxene and pigeonite are rarely present only in the Lower lava (Table 3-4). They are euhedral and are up to 0.3 mm in size.

Augite crystals are also clearly divided into phenocrysts and microphenocrysts by their Cr_2O_3 content. Augite phenocrysts have relatively high (> 0.2 wt.%) Cr_2O_3 content, whereas that of microphenocryst is negligible (~ 0 wt.%). The Mg# of the phenocrysts ranges from 78 to 85, and that of the microphenocrysts is from 75 to 81. Both the augite phenocryst and microphenocryst show sector zoning, which is superimposed on oscillatory zoning. The degree of zonation in

the phenocryst is weak relative to that of the microphenocryst.

3-3-4. Hornblende

Hornblende phenocrysts, up to 2 mm across, are present more dominantly in the Upper lava than in the Lower lava. They are partially opacitized from the margin. Apatite and vapor inclusions are found in hornblende occurred in the Upper lava. Hornblende phenocrysts commonly form crystal clots with plagioclase phenocryst. Hornblende microphenocrysts, abundantly present in the Lower lava, are completely opacitized. They form crystal clots with plagioclase and titanomagnetite microphenocrysts.

Hornblende phenocrysts are principally homogeneous in composition except for opacitized margins of the crystals. The Mg# of the phenocrysts ranges from 63 to 67 throughout the Tanetomi lava, and any significant difference in chemical composition is not found between Lower and Upper lavas though the data from the Lower lava are very scarce because they are opacitized. Hornblende microphenocrysts in the Lower lava are also completely opacitized, and their compositions can not be obtained.

3-3-5. Titanomagnetite

Titanomagnetite crystals are euhedral and are up to 0.3 mm in size. Both the abundance and size of the crystals are larger in the Lower lava than in the Upper lava. The chemical composition of titanomagnetite varies significantly with whole-rock composition throughout the Tanetomi lava, though it is apparently homogeneous within the crystal. The XFe^{3+} ($100 \times Fe^{3+}/(Fe^{2+}+Fe^{3+})$) of the titanomagnetite varies from 0.35 in the LL2 to 0.55 in the UL2 (Fig. 3-11).

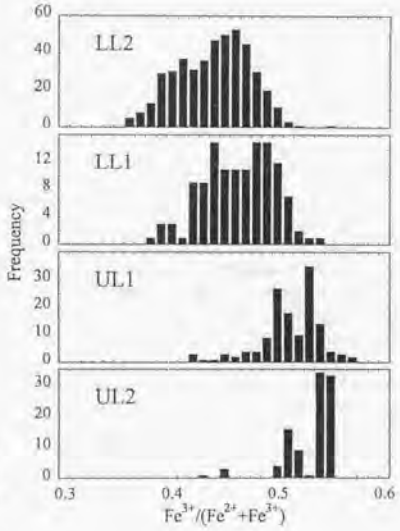

Figure 3-11. The histogram of the $Fe^{3+}/(Fe^{2+}+Fe^{3+})$ of titanomagnetite crystals for each lava flow unit of the Tanetomi lava.

3-4. Crystallization of Microphenocrysts

Microphenocrysts are common throughout the Tanetomi lava, which occupy the main volume of crystals observed in the lava (Table 3-4). They commonly form crystal clots composed of different crystal phases. Crystal clots composed of plagioclase, hornblende, and titanomagnetite are frequently present throughout the Tanetomi lava, and those composed of olivine, augite, plagioclase, and titanomagnetite are commonly found in the Lower lava. These crystal clots show evidence for simultaneous growth, suggesting that all microphenocryst phases in individual samples formed at the same crystallization stage. It is shown below that these microphenocrysts might have crystallized during and/or after eruption.

The magmatic temperature for the Lower lava (Kk-5 in Table 3-1) is estimated to be about 980~1030 °C by using the pyroxene microphenocrysts after Lindsley (1983). Equilibrium liquidus temperatures for the Kk-5 magma at 1 bar are calculated to be about 1180 °C for plagioclase, 1100 °C for olivine, and 1090 °C for augite after *Ghiorso and Sack* (1995). The calculated liquidus temperatures at 1 bar are significantly higher than the magmatic temperature, suggesting that the magma should have been supersaturated with these crystal phases when it erupted to the surface. The microphenocrysts of the Tanetomi magma might have formed under the supersaturated conditions. The Tanetomi magma was rich in dissolved water, which is suggested by the presence of hornblende phenocryst. When the hydrous magma moves upward through a conduit, decrease of water solubility in the melt leads to water saturation of the magma. Further ascent causes vapor exsolution and the magma is successively supersaturated with crystal phases due to increase in liquidus temperatures (e.g., *Geschwind and Rutherford*, 1995). Effusive eruption of the Tanetomi lava also gave enough time for microphenocryst crystallization.

This conjecture is consistent with the systematic variation of mineral compositions with whole-rock composition (Fig. 3-8 for plagioclase and Fig. 3-11 for titanomagnetite) suggesting *in situ* growth from individual magma batches with observed whole-rock compositions. Texture of some microphenocryst phases also consistent with the crystallization under the supersaturated condition. Sector zoning is observed in augite and in plagioclase microphenocrysts (Fig. 3-7a), which is considered to be formed by crystallization at relatively large growth rate (*Deer et al.*, 1978; *Smith and Lofgren*, 1983). Plagioclase microphenocrysts in the Lower lava commonly show reverse zoning in An content, which is also explained by rapid growth (e.g., *Lofgren*, 1974). The rapid growth of crystals could occur in a magma which is supersaturated with them during magma ascent.

All the plagioclase phenocrysts consist of cores and the surrounding clear mantles. The clear mantle has identical An content and textural feature to the clear region of the plagioclase microphenocryst, and thus the clear mantle is suggested to have grown at the same crystallization stage as that of the microphenocryst during magma ascent. There is no remarkable compositional difference between the clear mantle and the clear core in the clear-type plagioclase, though the clear mantle shows oscillatory zoning (Fig. 3-7b). The An content of plagioclase is very sensitive to changes in the physical and chemical conditions of the magma from which it crystallized. The similarity in An content might, therefore, suggest that the crystallization of the clear mantle started at the similar pressure condition to the crystallization of the clear core. The clear core is apparently homogeneous in composition, and thus it formed at nearly equilibrium condition, most plausibly in a magma chamber. From these the vapor exsolution in the magma was initiated soon after the discharge from the magma chamber. This indicates that water saturation was nearly attained in the magma chamber. The presence of vapor inclusion in hornblende phenocrysts also supports the water saturation of the Upper-lava magma during residence in the magma chamber.

3-5. Pressure at the Depth of the Magma Chamber

The An content of the clear core in the clear-type plagioclase ranges from 49 to 50 in the sample Kk-31. Given that the clear core was crystallized in equilibrium from the Kk-31 magma, the pressure condition is estimated by utilizing plagioclase-melt thermodynamic equilibria with the constraints that water saturation was achieved and that the temperature of the Kk-31 magma was close to the liquidus because of aphyric nature (Table 3-4). The thermodynamic solution models for plagioclase of *Elkins and Grove* (1990) and for silicate melt of *Ghiorso and Sack* (1995) are used. Water solubility as a function of pressure, temperature, and the melt composition is calculated from the model of *Moore et al.* (1998).

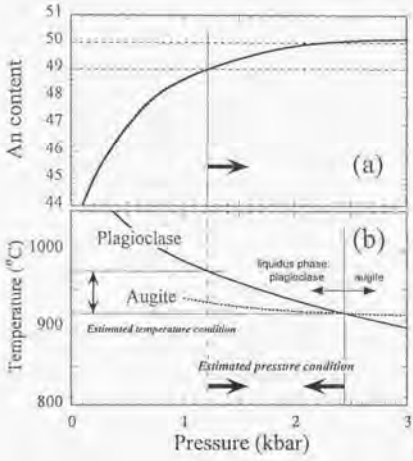

Figure 3-12. The equilibrium An content of plagioclase with the magma of the sample Kk-31 at the liquidus (a), along with the liquidus temperatures of plagioclase (continuous line) and augite (broken line) as a function of pressure, which are obtained from thermodynamic calculation (b). The range of the observed An content is shown with dotted lines (An49-50) in 12a. In 12b, the estimated range of pressure condition for the magma chamber and that of the magmatic temperature are shown.

Figure 3-12a shows the calculated An content of plagioclase in equilibrium with the composition of the water-saturated Kk-31 magma at the liquidus, as a function of a pressure. Calculated equilibrium liquidus temperatures of plagioclase (heavy continuous line) and augite (heavy broken line) which is obtained from the thermodynamic solution model of *Sack and Ghiorso* (1994a and b) are also shown in Fig. 3-12b. The equilibrium An content of plagioclase increases with an increase of pressure up to 3 kbar. The observed An content (An49-50) coincides with the calculated value if the pressure condition is higher than 1.2 kbar. At the pressure condition of >2.4 kbar, however, liquidus temperature of augite exceeds that of plagioclase, and augite would appear as a crystallizing phase contrary to the observation. From these, the pressure at the depth of the magma reservoir is estimated to be 1.2~2.4 kbar. This estimated condition is in accordance with >2 kbars estimated for the magma chamber of the Kutsugata lava. The magmatic temperature of the Kk-31, which is the most differentiated composition in the Tanetomi lava, is obtained simultaneously to be about 920~970 °C on the basis that the magma was close to the liquidus temperature of plagioclase.

3-6. Magma Mixing and Eruption

Many felsic eruptive materials show evidence for magma mixing with mafic magma just before eruption, and it has been demonstrated that injection of a mafic magma into a felsic magma chamber could trigger the eruption (*Sparks et al.*, 1977; *Eichelberger*, 1980; *Pallister et al.*, 1992). Though a proportion of effusive eruptions is significant in felsic volcanism, investigation on the trigger of such eruption is scarce (e.g., *Watts et al.*, 1999), in contrast to plenty of works on explosive eruptions. In the case of explosive eruptions, there is a consensus that supersaturation of the melt with respect to volatiles after injection of the mafic magma is important, and several possible mechanisms to lead supersaturation have been proposed. But there may be a difference in trigger of eruptions between explosive and effusive, though they arise partly from degassing process during magma ascent to the surface (*Eichelberger et al.*, 1986). In this section, mixing mechanism of an injected basaltic magma with a felsic magma is considered for the Tanetomi lava, and possible mechanisms for triggering eruptions are quantitatively evaluated.

3-6-1. Mixing with a basaltic magma

In the LL2, high-Mg# olivine and augite phenocrysts and An-rich plagioclase core are present, which rarely form crystal clots. Some olivine phenocrysts have rounded outline and thus are not in equilibrium with the observed whole-rock composition of the lava (mostly equivalent to the melt composition because of aphyric nature). The An content of the An-rich core with up to 85 is also much higher than that of the clear-type plagioclase with up to An62 which is considered to have crystallized in equilibrium from the Lower-lava magma. Therefore it is plausible to consider that these crystals brought from a less differentiated magma than the present whole-rock composition by magma mixing. The high Mg# of olivine phenocrysts with more than 83 suggests that the mafic end-member magma might have been basaltic composition.

Throughout the LL2, partial dissolution texture is present surrounding the plagioclase core which has a similar An content to that of the clear type (dissolved cored type; Figs. 3-6c and 3-7c). Because the clear region inside the dissolution texture is suggested to have crystallized in equilibrium from the original felsic magma, the dissolution texture might have formed by heating and/or compositional change of the melt surrounding the plagioclase, resulting from the magma mixing. The An content inside the partial dissolution texture is similar to that outside the dissolution texture corresponding to the clear mantle (Fig. 3-7c). This is explained by the following process. The plagioclase core becomes out of equilibrium by heating and changing the surrounding melt composition, and it decomposed to more calcic plagioclase and melt (partial dissolution). During ascent of the magma from the magma chamber, the liquidus temperature of plagioclase increases by vapor exsolution and plagioclase again start to grow. The An content of this plagioclase is similar to that of the plagioclase grow before the magma mixing if the melt composition was not modified significantly by the magma mixing. It is shown later that this condition is satisfied in the Tanetomi lava.

Mixing of a homogeneous basaltic magma and a homogeneous felsic magma could produce linear composition trend. The composition trends of the LL2 are, however, not likely to have formed by mixing of two end-component magmas. This is because the crystals derived from the basaltic magma are more frequently present in the SiO_2-rich samples in the LL2. Furthermore the Na_2O and P_2O_5 of the LL2 decrease with an increase of SiO_2 content (Fig. 3-2), which requires that the basaltic end-component magma would contain more Na_2O and P_2O_5 contents than the felsic end-component magma (Fig. 3-13). The Na_2O content of the fictive "basalt magma", which is calculated by the linear extrapolation from the composition trend of the LL2, would be about 9 wt.% if its SiO_2 content is 50 wt.% (open circle in Fig. 3-13c). The MgO and CaO contents of the "basalt magma" is also as low as about 4 wt.% and 7 wt.%, respectively, which are

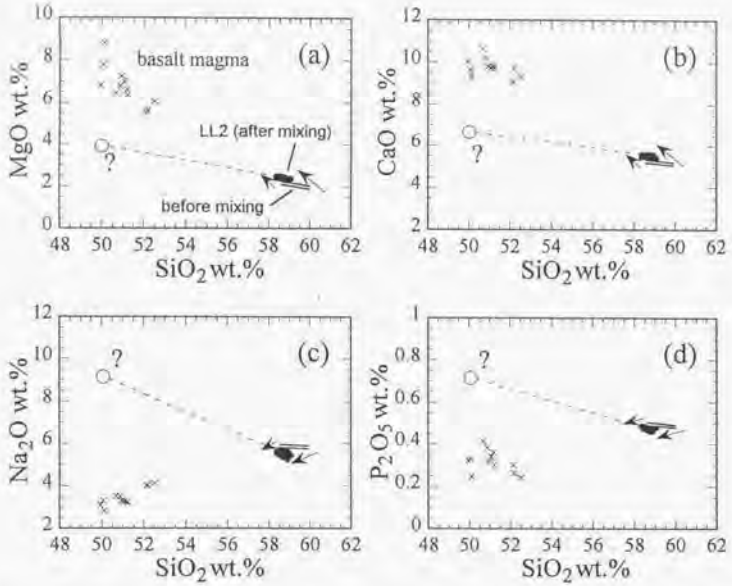

Figure 3-13. Whole-rock MgO, CaO, Na_2O, and P_2O_5 contents of the LL2 (solid circles) along with those of basaltic rocks from Rishiri Volcano (crosses), plotted against SiO_2 content. Double lines indicate assumed composition trend of felsic magma before the mixing with basaltic magma, which is obtained from the linear extrapolation from the composition trends of the LL1. Composition trends of the LL2 were produced by shifting of the double lines to the direction indicated by arrows, by mixing with the basalt magmas (crosses). Open circle denotes a *fictive* basaltic end-component magma on the linear extrapolation of the observed composition trend of the LL2. The data of basaltic rocks from Rishiri Volcano is after *Kobayashi et al.* (1987).

significantly lower than the MgO content of basaltic magmas erupted from Rishiri Volcano (crosses in Fig. 3-13).

Another possibility for the LL2 trend is the mixing of a basaltic magma with a felsic magma in which compositional variation had already formed (Fig. 3-14). If the basalt magma (solid circle) is mixed with the felsic magma which has compositional diversity (open band), the resulting composition trend (gray band) shifts from the original trend of the felsic magma. In this case, the basaltic end-component magma is not necessary on the linear extrapolation from the composition trend of the mixed magma. The composition of the basalt magma, composition trend of the felsic magma, and the relative amount of the basalt magma to the felsic magma determine the slope of the composition trend of the mixed magma. If the relative amount of basalt is greater for the felsic magma with higher SiO_2 content, the slope becomes steep in the case of Fig. 3-14 (dark gray band). This heterogeneous mixing is suggested for the LL2, wherein the abundance of high-Mg# olivine phenocrysts derived from basalt is twice in the SiO_2-rich sample compared to those in the SiO_2-poor sample.

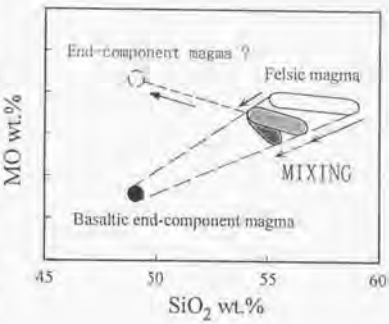

Figure 3-14. Schematic illustration of a variation diagram showing formation of composition trend by magma mixing. The basaltic end-component magma (solid circle) is not always on the liner extrapolation from the composition trend of the mixed magma (light gray band) when the felsic magma exhibits compositional variation before the mixing (open band). Fictive basalt end-component magma which is on the extrapolation from the composition trend of the mixed magma is shown by broken circle. If the basalt magma mixes with the felsic magma heterogencously, the slope of the mixed magma changes (dark gray band).

This hypothesis explains well the characteristics of the composition trends of the LL2. The composition trend of the LL1 is considered to reflect the trend of the original felsic magma before the magma mixing, because the crystals derived from the basaltic magma is scarce. The assumed composition trends of the felsic magma before the magma mixing, which is a linear extrapolation from the composition trends of the LL1, are shown in Fig. 3-13 (double lines). The gentle slopes in MgO and CaO composition trends are accounted by the mixing of a MgO and CaO-rich basalt magma (crosses in Fig. 3-13a and 3-13b) with a MgO and CaO-poor felsic magma exhibiting composition trends. Steep negative composition trends of Na_2O and P_2O_5 are also explained by heterogeneous mixing of the Na_2O and P_2O_5-poor basalt magma (crosses in Figs. 3-13c and 3-13d) with the Na_2O and P_2O_5-rich felsic magma having compositional diversity. Only if the basaltic end-component magma is on the linear extrapolation from the composition trend of the felsic magma before the mixing, resulting composition trend coincides with the trend before the mixing.

The fraction of the mixed basalt magma in the LL2 is roughly estimated, given that the basaltic end-component magma was homogeneous before the magma mixing. It is assumed that the most differentiated LL2 magma was produced by mixing of the basalt magma with the most differentiated LL1 magma, and that the relative abundance of the basalt magma in the most differentiated LL2 magma is twice as much as that of the least differentiated LL2 magma. If the SiO_2 content of the basalt is 50 wt.%, which is the minimum value of basaltic rocks observed in Rishiri Volcano, the most differentiated LL2 magma could be produced by mixing of the basalt and the felsic magma with the ratio 8 : 92, and the least differentiated LL2 magma was with the ratio 4 : 96. And if the SiO_2 content of the basalt is 52 wt.%, the most differentiated LL2 magma could be produced with the mixing ratio of 10 : 90, and the least differentiated LL2 magma was with the ratio of 5 : 95. The composition of the basalt end-component magma and the mixing ratio of the basaltic and felsic magmas cannot be determined exactly from the observation because of the narrow range in the compositional variation of the LL2.

3-6-2. Time scale from magma mixing to eruption

Mg-rich olivine phenocrysts in the LL2 are zoned in terms of Mg# (Fig. 3-10b). This

might be caused by Mg-Fe interdiffusion, resulting from the disequilibrium of olivine with the surrounding melt after magma mixing. By utilizing this diffusion profile, the time scale from the magma mixing in the magma chamber to the solidification at the surface after the eruption is estimated.

It is assumed that olivine crystal was initially homogeneous with Mg#83 with a diameter of 570 μm. Homogeneous composition is suggested from the flat zoning pattern in the central part of the crystal (Fig. 3-10b). The Fe-Mg exchange coefficient between olivine and silicate melt of 0.3 (*Roeder and Emslie,* 1970) and the whole-rock ferric-ferrous ratio after *Kobayashi et al.* (1987) are assumed. The LL2 magma can equilibrate with olivine with Mg#75, and this is adopted as a boundary condition. The Mg-Fe interdiffusion coefficient of $10^{-12.5}$ cm^2/sec is used at 1000 °C (estimated temperature for the LL2) after *Misener* (1974). Calculated diffusion profiles are shown in Fig. 3-15 for several time steps. The comparison of the calculated and actual profiles suggests that 1~2 years is plausible for the period from the magma mixing to the solidification of the host magma at the surface. If the interdiffusion coefficient of $10^{-11.5}$ cm^2/sec (after *Jurewicz and Watson,* 1988) and $10^{-13.5}$ cm^2/sec (after *Chakraborty,* 1997) is adopted, the time scale of 15~25 days and 4~7 years is obtained, respectively. The low interdiffusion coefficient of *Chakraborty* (1997) might come partly from low oxygen fugasity condition of his experiments (f_{O2}~10^{-12} bar). In the higher f_{O2} condition such as that of NNO buffer, the coefficient becomes much higher (*Jurewicz and Watson,* 1988) and thus the estimated time scale could be close to the value after *Misener* (1974).

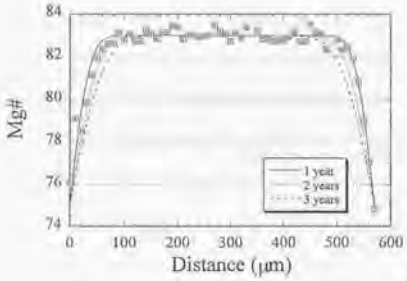

Figure 3-15. Calculated diffusion profile of Mg# for 1, 2, and 3 years, along with the observed line profile of Mg# in olivine phenocryst (ol 1-Ta19).

3-6-3. Mechanism of magma mixing

There are several mixing mechanisms of a basalt magma with a felsic magma before eruption. One possible mechanism is a forced mixing in a conduit during ascent of the magma to the surface (e.g., *Koyaguchi,* 1986). Felsic and basaltic magmas which are stratified stably in a magma chamber may mix effectively in the conduit. During ascent of the LL2 magma, the clear mantle of the plagioclase core (Fig. 3-6), as well as microphenocrysts were grown. Inside the clear mantle of the dissolved cored-type plagioclase, partial dissolution texture is observed (Fig. 3-6c) which was formed by changing of the melt composition surrounding the plagioclase by mixing with the basaltic magma. The compositional gap between the dissolution texture and the surrounding clear mantle suggests that these textures were produced at different crystallization stages. Thus the magma mixing occurred before ascent of the magma, most plausibly, in the magma chamber.

Another mechanism for magma mixing is a vigorous convection of the felsic magma in a magma chamber. When the basalt magma intrudes into the magma chamber, the felsic magma is superheated at the base and vigorous convection could occur (*Sparks et al.*, 1977). Convective current entrains the basal basalt magma and it may be stirred in the felsic magma. In the Tanetomi magma chamber the felsic magma had a compositional variation and it was stratified stably before the injection of the basalt magma. If vigorous convection occurred in the felsic magma, the basalt component would have been distributed homogeneously in the felsic magma, or greater amount of the basalt magma would have mixed with the less differentiated felsic magma because the basalt magma is likely to have mixed easily with the felsic magma at the portion just overlying the basaltic layer. However, the basalt component is heterogeneous in the LL2, and is rather present in the more differentiated composition as inferred from the abundance of the olivine phenocryst. The compositional variation of the LL2 is apparently preserved, which also suggests that the convection might not have occurred effectively.

Basaltic magma could also have mixed with the felsic magma as a fountain when it injected to the magma body. This may explain well the fact that compositional variation of the LL2 is preserved and that the basalt magma is mixed heterogeneously with the felsic magma. The forced convection enables effective mixing of the basalt magma with the felsic magma, without disturbing the overall stratification of the felsic magma in the magma chamber. *Snyder and Tait* (1996) showed by fluid mechanical experiments that a thermal convection caused by injection of a hot basalt magma could transport the basalt magma to the upper part of a magma chamber and lead to localized mixing with a felsic magma, even though the basalt magma is denser than the overlying felsic magma. Greater amount of the basalt component could have mixed with the more differentiated felsic magma if the fountain transported the basalt magma to the upper part of the felsic magma in the compositional stratification.

3-6-4. Trigger of the eruption of the Lower lava

Volcanic eruption occurs when a magma chamber undergoes a volume and pressure increase and the pressure rises sufficiently to fracture the wall rocks. In the case that a replenishment of magma is responsible for the eruption, the tapping of the magma chamber may be attained by a net volume increase of the injected magma and a volume increase caused by vapor exsolution in the magma chamber. The latter mechanism has been believed to be very important as well as the former mechanism in explosive eruptions (e.g., *Sparks et al.*, 1977). In this section the contribution of the latter mechanism in the LL2 of the Tanetomi lava is evaluated.

The vapor exsolution in the magma chamber could occur both in the intruded basaltic magma and in the felsic magma. Supersaturation of vapor phases occurs in the basaltic magma if it crystallizes extensively due to a temperature decrease caused by mixing with the lower-temperature felsic magma. Basaltic rocks from Rishiri Volcano are rich in alkalis. Therefore the injected basaltic magma is considered to have been rich in dissolved water at depth and the condition of water saturation might have been attained easily. It is assumed that the injected basalt magma had similar chemical composition to that of the Kutsugata lava. This is because basaltic magma with chemical and petrographical features similar to the Kutsugata lava erupted from Rishiri Volcano in several stages of volcanic activity, and basaltic rocks comprising the volcano are mostly of this type (*Kobayashi*, 1987; *Ishizuka*, 1999). The least differentiated Kutsugata magma (Fm-57 in Table 2-1) is estimated to have a water content of 4 wt.% and a temperature of 1110 °C. If this magma was cooled to 1000 °C, which is the estimated temperature of the Lower lava, significant amount of crystals with up to 25 wt.% would have been formed (after *Ghiorso and Sack*, 1995). At this temperature, however, the magma is still undersaturated with water (after *Moore et al.*, 1998). Thus the vapor exsolution of the injected basalt magma is not likely to have occurred in the Tanetomi magma chamber.

The vapor exsolution of the felsic magma could also occur by heating by the basaltic magma, because water solubility in the silicate melt has a negative temperature dependence (e.g., *Holtz et al.*, 1995; *Yamashita*, 1999). It is again assumed that the injected basalt magma was similar to that of the magma with the least differentiated composition in the Kutsugata lava (1110 °C), and that the felsic magma had a temperature of 1000 °C before the mixing. If the basalt magma mixed with the felsic magma with the mixing ratio of 10 : 90 which is the estimated maximum fraction of the basalt magma, the temperature of the mixed magma would increase to 1010 °C. Given that the felsic magma was saturated with water before the mixing, the temperature increase of 10 °C results in the exsolution of only 0.05 wt.% water according to the water solubility model of *Moore et al.* (1998). The fractional volume expansion arisen from the vapor exsolution is on the order of ~10^{-3} (*Yamashita*, 1999), which is much smaller than the net volume increase of the injected basalt magma (10^{-2}~10^{-1}) in this case.

From these, the tapping of the magma chamber is concluded to have been caused mainly by the forced injection of the basalt magma. Considering that the LL1 magma predated the eruption of the LL2 magma, the tapping of the magma chamber might have started soon after the injection of the basalt magma. The LL1 magma, which is mostly free from the crystals derived from the basaltic magma, discharged from the magma chamber before the fountain of the injected basalt magma affected the composition of the overall felsic magma. The "non-explosive" tapping process could result in the slow ascent of the magma and thus effective degassing from the magma during ascent, which gave rise to the effusive eruption of the Tanetomi lava.

3-7. Boundary Layer Fractionation of the Upper Lava Magma

The Upper lava forms a smooth composition trend, and the mineral assemblage is plagioclase, hornblende, and titanomagnetite. The compositional variation of the Upper lava is considered to have formed after the eruption of the Lower lava. If the variation of the Upper lava was established before discharge of the Lower lava, high-density Lower-lava magma should have been overlain by the low-density Upper-lava magma in the magma chamber just before the eruption, and thus the Upper lava should have predated the Lower lava. In this section, formation process of the variation of the Upper lava is discussed on the basis of the whole-rock composition trends.

The Upper lava is aphyric, generally less than 0.5 vol.% crystals (Table 3-4). The crystals in the Upper lava are the clear and Ab-rich plagioclases, hornblende, and titanomagnetite. One possible mechanism to form smooth composition trend of the Upper lava is two-component magma mixing. Because the LL1, UL1, and UL2 form relatively smooth composition trends (Fig. 3-2), the basic end-component magma might be the LL1 which remained in the magma chamber. Mixing of this magma with a more felsic magma (this might be an exotic magma or partial melt of the crust) could produce tight linear composition trend. However, composition trends such as CaO- SiO_2 and Sr-SiO_2 are significantly curved, though some elements form linear trends (Fig. 3-2). Therefore, the simple two-component magma mixing is not responsible for the formation of the Upper-lava variation. Mixing of more than three end component magmas is also unlikely, because such mechanism would produce compositional "area" in variation diagrams (e.g., *Freundt and Schmincke*, 1992) rather than composition "trend". All the Upper-lava magma could be the product of melting of the crust. If so, however, abundant restite crystals may be present (*Huppert and Sparks*, 1988). This is against the observation that the Upper-lava samples are fairly aphyric. Thus it is plausible to consider that the composition trend of the Upper lava was produced principally by crystal fractionation.

The fractionation mechanism is considered by estimating chemical compositions of

fractionated mineral phases, as well as their weight fractions, from the whole-rock composition trends after the method described in Appendix B. Though composition trends of overall Upper lava are slightly curved in some elements as stated above, those of each lava flow unit can be approximated to be linear. Therefore the compositional trends of 10 major elements are modeled for both the UL1 and UL2. Parent and daughter magmas are represented by the least and most differentiated samples in the individual lavas, respectively (Table 3-6). During differentiation of the Upper lava, plagioclase and hornblende should have fractionated dominantly because they are the phenocryst phases. Decrease in the TiO_2 and P_2O_5 contents with an increase of SiO_2 suggests significant fractionation of titanomagnetite and apatite. Therefore plagioclase, hornblende, titanomagnetite, and apatite are selected as the fractionated mineral phases. To reduce the parameters, chemical composition of only separated plagioclase is estimated, though hornblende and titanomagnetite should be treated as solid solutions. Major element composition of plagioclase is expressed as a function of An content. Those of titanomagnetite and hornblende are represented by the observed compositions in the Upper lava (Table 3-6).

Mass-balance equations of 10 elements are written by using above relations. The mass-balance equations of individual elements were weighted by dividing by the analytical error of the XRF analysis (*Kushiro,* 1994). Five unknown variables, An content of plagioclase and weight fractions of four fractionated phases are estimated by the following method. At a given An content, linear least-squares calculation was performed by the method of *Bryan et al.* (1969). Then, χ^2 surface was displayed as a function of the An content, and the value which minimize the χ^2 was adopted as the estimation. Weight fractions of mineral phases are determined uniquely when the An content is determined. Errors for the estimated parameters are obtained from covariance matrix calculated by curvature matrix of the χ^2 surface.

The results of the calculation are shown in Table 3-7, and the calculated daughter composition is listed in Table 3-6. The composition trend of the Upper lava requires extensive fractionation of plagioclase and hornblende. The modal proportion of the fractionated mineral phases do not change significantly from the UL1 to the UL2. The estimated An content of the fractionated plagioclase is as low as 40 throughout the evolution of the Upper-lava magma.

The clear-type plagioclase crystals are suggested to have been in equilibrium with the magma with the observed whole-rock composition. The An content of the clear-type plagioclase in the Upper lava is more than 50 (Fig. 3-8), therefore, fractionation of the clear-type plagioclase

Table 3-6. Parent, Daughter, and Calculated Compositions and Mineral Compositions of Crystal Fractionation Modeling

	Fractionated Minerals		Upper Lava 1			Upper Lava 2		
	Hornblende	Titano-magnetite	Parent (Kk-22)	Daughter (Kr-73)	Calculated	Parent (Kr-64)	Daughter (Kk-31)	Calculated
SiO_2	42.80	0.00	59.89	62.69	62.46	62.89	65.07	65.23
TiO_2	3.03	8.07	0.91	0.73	0.79	0.71	0.58	0.58
Al_2O_3	11.42	3.29	18.22	17.69	17.75	17.70	17.43	17.43
Fe_2O_3	14.39	86.12	6.35	5.22	5.19	5.16	4.13	4.13
MnO	0.32	0.46	0.15	0.14	0.15	0.13	0.13	0.13
MgO	13.81	2.05	1.97	1.52	1.71	1.49	1.12	1.11
CaO	11.09	0.00	5.13	4.37	4.28	4.33	3.56	3.55
Na_2O	2.81	0.00	5.55	5.66	5.64	5.59	5.85	5.72
K_2O	0.32	0.00	1.37	1.62	1.65	1.63	1.86	1.84
P_2O_5	0.00	0.00	0.46	0.36	0.38	0.36	0.26	0.26

Units are in wt.%. Sample names are shown in parenthesis. Kr-73 is locality No. 16 in Fig. 3-1. Major element compositions are normalized for the total weight to 100 %.

Table 3-7. Result of Least Squares Optimization of Crystal Fractionation Modeling along with Estimated Temperatures of the Main Magma and Interstitial Melt from Mushy Boundary for the UL1 and UL2

	UL1				UL2			
	wt.%	1σ	An	1σ	wt.%	1σ	An	1σ
Plagioclase	11.40	(1.11)	40.8	(4.6)	7.29	(0.32)	43.0	(2.2)
Hornblende	3.79	(0.94)	-	-	3.57	(0.27)	-	-
Titanomagnetite	1.75	(0.48)	-	-	1.19	(0.05)	-	-
Apatite	0.34	(0.12)	-	-	0.30	(0.04)	-	-
				Temperature				
Main magma		970 °C				950 °C		
Interstitial melt		905±20 °C				919±5 °C		

did not play an important role on the chemical differentiation of the Upper-lava magma. On the contrary, estimated An content of 40–43 is in good agreement with the An content of the Ab-rich plagioclase core (Fig. 3-9), showing that separation of the Ab-rich cores was dominant. The Ab-rich cores commonly show rounded outline and partial dissolution texture (Fig. 3-7e), suggesting that they were not in equilibrium with the magma with the observed whole-rock composition. Plausible crystallization site of the Ab-rich core is mushy boundary layer along the wall of the magma chamber. In the mush zone, temperature is lower than the main part of the magma body and thus crystals grew from more differentiated melt than the main magma. Differentiation of the main magma could proceed if interstitial melt coexisting with the low-temperature phases in the mush zone is extracted to mix with the main magma, which is induced by density contrast among the crystals, interstitial melt, and main magma (boundary layer fractionation).

Crystal aggregates composed of Ab-rich core plagioclase, hornblende, and titanomagnetite may represent a part of the crystal mush. When they were transported from the mush zone to the main magma body by convective plume of the interstitial melt for example, they could not equilibrate with the main magma and the Ab-rich plagioclase may have partially dissolved. Considering that the composition of the hornblende phenocrysts is similar in individual samples, all the hornblende phenocrysts are suggested to have derived from the mushy boundary layer. This is supported by the absence of crystal aggregates composed of clear-type plagioclase and hornblende phenocrysts.

The temperature condition in the mushy boundary layer at which the crystal-melt separation occurred is estimated by using the results of the crystal fractionation modeling. The composition trends of both the UL1 and UL2 can be explained by separation of plagioclase, hornblende, titanomagnetite, and apatite. Because the composition trends of individual lava flow units are linear, it is plausible to consider that the compositional variation was established by two-component mixing between the averaged interstitial melt from the mush zone and the least differentiated magma in each flow unit. The averaged interstitial melt should be in equilibrium with the fractionated plagioclase, hornblende, titanomagnetite, and apatite, and it is on the linear extrapolation (SiO_2-rich side) of the observed composition trend. The composition of the averaged melt and temperature condition can therefore be estimated from the An content of the fractionated plagioclase which obtained from the crystal fractionation modeling (Table 3-6), by utilizing the plagioclase-melt equilibria and water solubility model of *Moore et al.* (1998) as used above.

Given that the pressure at the depth of the magma chamber is 2 kbar, the temperature of 905±20 °C for the UL1 and that of 919±5 °C for the UL2 are obtained (Table 3-7). These temperatures are significantly lower than those estimated for the main part of the magma body (970 °C for the UL1 and 950 °C for the UL2 at 2 kbar), supporting the view that the crystal-melt sepa-

ration took place in the low-temperature mushy boundary layer. Though heat loss through the crust and the mixing of the fractionated interstitial melt from the mush zone lowered the temperature of the main magma and caused its differentiation, but at the same time, the liquidus temperature of any crystal phases in the main magma was significantly decreased. This mechanism kept the Tanetomi magma to be principally aphyric throughout the wide range of compositional evolution.

In the Lower-lava samples, crystal aggregates composed of hornblende, Ab-rich plagioclase, and magnetite are generally present. This suggests that the compositional evolution of the Lower-lava magma might have been also produced by boundary layer fractionation, other than the modification by the replenishment of the basalt magma. Though the compositional range is narrow and the composition might be slightly affected by the replenishment, crystal fractionation is modeled for the LL1, as done for the Upper lava. In this calculation, composition of the separated plagioclase is fixed to be An50. Composition of the fractionated phases listed in Table 3-6 is used. Parent and daughter magma compositions are the samples Bi-8 and Kr-74, respectively (Table 3-1). The composition trend of the LL1 is explained by the separation of the same mineral assemblage as that of the crystal aggregates: 1.4 wt.% plagioclase, 1.5 wt.% hornblende, 0.5 wt.% titanomagnetite, and 0.1 wt.% apatite. The fractionation of plagioclase is comparable to that of hornblende. The low degree of plagioclase fractionation relative to hornblende reflects the increase of whole-rock Al_2O_3 content with SiO_2 content.

The $^{87}Sr/^{86}Sr$ ratio of the UL2 is lower than that of the UL1 (Fig. 3-5), suggesting that the UL2 was not the derivative magma from the magma with the most differentiated composition in the UL1. If the most differentiated UL1 magma was the parental magma of the UL2, the $^{87}Sr/^{86}Sr$ ratio of the UL1 is expected to be similar to or higher than that of the UL1, given that the variation of the $^{87}Sr/^{86}Sr$ was originated from the assimilation of crustal materials with higher $^{87}Sr/^{86}Sr$ ratio than that of the Tanetomi magma. Therefore the compositional variation of the Upper lava represents their spatial variation in the magma chamber. If this is correct, the UL1 magma was overlain by the UL2 magma before the eruption.

3-8. Assimilation of Crustal Materials

The compositional variation of the major elements in the Upper lava was produced principally by crystal fractionation as discussed above. As in the case of the Kutsugata magma chamber, assimilation of the crustal material is suggested from the variation of the isotopic compositions (Fig. 3-5). The degree of assimilation and its relative contribution to the evolution of the Upper-lava magma is discussed in this section.

3-8-1. Assimilation of partial melt from the crust

Figure 3-16 shows the concentration of the samples Kr-56 and Kk-31 (the most differentiated samples in the UL1 and UL2) normalized by the value of the samples Kk-22 and Kr-64, respectively (the least differentiated samples in the UL1 and UL2). The concentrations of the trace elements of the daughter magma, which is expected from the crystal fractionation, are also calculated for both the UL1 and UL2 (Table 3-8) by using the result of the crystal fractionation modeling (Table 3-7). Mineral-melt partition coefficients determined in andesitic systems were used for the calculation, and are listed in Table 3-9.

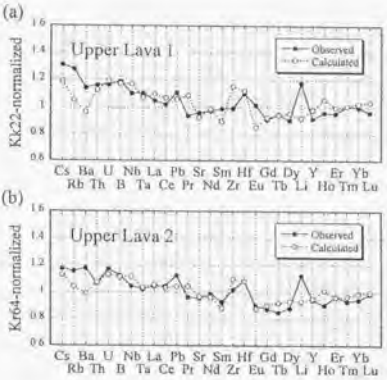

Figure 3-16. Concentration of trace elements of the most differentiated sample and that of the calculated daughter magma, normalized by the value of the least differentiated sample for the UL1 (a) and UL2 (b).

Table 3-8. Parent, Daughter, and Calculated Daughter Compositions for Crystal Fractionation Calculation

	Upper Lava 1			Upper Lava 2		
	Parent	Daughter		Parent	Daughter	
	Kk-22	Kr-56	Calculated	Kr-64	Kk-31	Calculated
Cs	1.48	1.94	1.76	1.97	2.32	2.22
Rb	34.5	44.2	36.3	45.0	52.1	46.8
Ba	310	355	299	365	430	360
Th	4.22	4.91	4.75	5.17	5.51	5.55
U	1.22	1.42	1.46	1.44	1.68	1.62
B	9.70	11.6	11.4	11.4	12.8	12.7
Nb	8.31	9.15	9.73	9.33	9.75	10.38
Ta	0.66	0.73	0.70	0.75	0.76	0.77
La	27.3	28.7	30.0	29.4	30.7	31.0
Ce	59.9	61.0	63.9	60.8	63.6	62.4
Pb	6.01	6.66	6.36	6.83	7.68	7.11
Pr	7.43	6.96	8.07	7.15	6.87	7.45
Sr	487	467	451	455	434	441
Nd	28.8	28.0	28.4	27.6	27.3	26.5
Sm	5.44	5.39	4.87	5.46	5.05	4.81
Zr	325	322	374	335	341	368
Hf	5.71	6.27	6.41	6.05	6.55	6.54
Eu	1.78	1.81	1.52	1.81	1.63	1.59
Gd	5.56	5.05	5.15	5.05	4.40	4.56
Tb	0.89	0.84	0.83	0.83	0.70	0.76
Dy	5.39	4.88	5.16	5.11	4.49	4.75
Li	14.6	17.3	13.5	17.7	19.8	16.4
Y	34.9	31.9	34.2	31.2	29.4	29.6
Ho	1.12	1.08	1.18	1.06	0.95	1.07
Er	3.10	2.96	3.09	2.86	2.76	2.74
Tm	0.49	0.49	0.49	0.47	0.44	0.46
Yb	3.56	3.56	3.66	3.39	3.19	3.35
Lu	0.53	0.51	0.55	0.51	0.50	0.51

Table 3-9. Mineral/Melt Partition Coefficients used for Crystal Fractionation Calculation

	Partition Coefficients							
	plagioclase	ref	hornblende	ref	Titanomagnetite	ref	Apatite	ref
Cs	0.12	1	0.01	3	0.01	3	0.7	13
Rb	0.97	1	0.40	3	0.15	4	0.4	13
Ba	1.66	1	0.30	3	0.10	3	0.45	13
Th	0.03	1	0.16	3	0.01	3	17.1	16
U	0.03	1	0.008	6	0.09	11	1.82	16
B	0.045	*	0.20	*	0.7	*	1.82	*
Nb	0.045	2	0.20	6	0.7	12	1.82	*
Ta	0.03	1	0.59	3	2.2	13	14.5	*
La	0.18	3	0.31	3	0.66	3	14.5	17
Ce	0.12	3	0.53	3	0.71	3	21.1	17
Pb	0.61	4	0.53	4	2.0	4	0.03	18
Pr	0.13	2	0.35	5	0.11	*	21.1	*
Sr	2.0	2	0.01	3	0.11	4	1.4	19
Nd	0.09	3	1.2	3	0.93	3	32.8	17
Sm	0.06	3	2.0	3	1.2	3	46.0	17
Zr	0.17	1	0.50	3	0.38	4	0.636	17
Hf	0.38	1	0.54	3	0.24	3	0.730	17
Eu	1.06	1	1.9	3	0.91	3	25.5	17
Gd	0.067	2	2.0	7	0.0055	14	43.9	17
Tb	0.03	1	2.0	3	1.3	3	34.8	*
Dy	0.034	2	2.0	7	0.58	15	34.8	17
Li	0.85	2	0.3	8	0.64	*	34.8	*
Y	0.038	2	1.47	9	0.64	4	34.8	*
Ho	0.048	5	2.0	10	0.0079	14	13.3	20
Er	0.019	2	2.34	9	0.44	*	22.7	17
Tm	0.036	5	2.1	*	0.44	*	22.7	*
Yb	0.10	3	2.1	3	0.44	3	15.4	17
Lu	0.10	3	2.1	3	0.30	3	13.8	17

Ref. source are: 1, *Villemant* (1988); 2, *Dunn and Sen* (1994); 3, *Bacon and Druitt* (1988); 4, *Ewart and Griffin* (1994); 5, *McKenzie and O'Nions* (1991); 6, *Brenan et al.* (1995); 7, *Fujimaki and Tatsumoto* (1984); 8, *Dostal et al.* (1983); 9, *Sisson* (1994); 10, *Green and Pearson* (1985); 11, *Lemarchand et al.* (1987); 12, *Green and Pearson* (1987); 13, *Mahood and Stimac* (1990), 14, *Nielsen et al.* (1992); 15, *Luhr and* Carmichael (1980); 16, *Luhr et al.* (1984); 17, *Fujimaki* (1986); 18, *Bea et al.* (1994); 19, *Watson and Green* (1981); 20, *Paster et al.* (1974); *, estimation from partition coefficients of similarly incompatible elements.

The concentration patterns of the UL1 and UL2 are basically explained by crystal fractionation, if uncertainties of the partition coefficients and the crystal fractionation calculations are considered. The concentrations of the highly incompatible trace elements such as Cs, Rb, and Ba and Li in the actual daughter magmas are higher than those of the calculated daughter magmas. These elements are considered to have come from the surrounding crust. The enrichment of Li relative to Y suggests that the assimilated material was closely related to H_2O-rich fluid. If the material was only the fluid phase, however, B is also expected to have been enriched in the assimilated material. Thus the material might have been melt phase wherein H_2O-fluid was dissolved, as is the case of the Kutsugata lava.

In the Upper lava, the isotopic ratios of $^{206}Pb/^{204}Pb$, $^{207}Pb/^{204}Pb$, and $^{208}Pb/^{204}Pb$ increase progressively with the whole-rock SiO_2 content, though the $^{87}Sr/^{86}Sr$ ratio of the UL1 is higher than that of the UL2. The variation of both the Sr and Pb isotopic compositions was caused by the assimilation. As discussed above, the UL2 magma is suggested to have overlain the UL1 magma in the magma chamber. The crustal materials are likely to have been assimilated from the floor of the magma chamber because they are considered to have low density than andesitic

magma. Sr and Pb derived from the crust could be transported to the main magma both by fractionated melt and aqueous fluid from the floor mush zone. If all the assimilated materials was transported by the fractionated melt, it is expected that the $^{87}Sr/^{86}Sr$ ratio would increase with the SiO_2 content, as the $^{206}Pb/^{204}Pb$, $^{207}Pb/^{204}Pb$, and $^{208}Pb/^{204}Pb$ ratios. The Pb contained by the fluid phase could have been transported to the upper part of the magma body because of high solubility, and affected the Pb isotopic composition of the UL2 magma. On the contrary the Sr in the H_2O-rich fluid might have partitioned to the melt phase during transportation because the compatibility of Sr to the fluid phases is much lower than that of Pb (*Kogiso and Tatsumi*, 1997). This may result in the higher $^{87}Sr/^{86}Sr$ ratio of the lower part of the magma chamber.

3-8-2 Degree of assimilation

The contribution of the assimilation of the crustal materials to the evolution of the Upper-lava magma is evaluated as done for the Kutsugata lava. The crust surrounding the magma chamber is assumed to have a composition of representative granite (Table 3-10). Rb and Ba are assumed again to have been completely incompatible in the granite. If the degree of melting of the granite is 1 %, the difference in Rb and Ba contents between observed and calculated daughter magmas can account for assimilation of ~0.2 wt.% for both the UL1 and UL2. Even if the degree of melting of 5 % is assumed, assimilation of the crustal material with <0.8 wt.% explains the enrichment of Rb and Ba in the observed daughter magmas. Therefore the assimilation did not much affect the compositional evolution of the major elements in the Upper-lava magmas, because the amount of the fractionated crystals is 17 wt.% for the UL1 and 12 wt.% for the UL2 (Table 3-7).

Table 3-10. Parameters and Results of the Modeling for Estimating the Degree of Assimilation

	Upper Lava 1		Upper Lava 2	
	Rb	Ba	Rb	Ba
		Observed and Calculated (ppm)		
Observed daughter magma	44.2	355	52.1	430
Calculated daughter magma	36.3	299	46.8	360
		Representative Granite (ppm)		
Granite* (whole rock)	245	440	245	440
		Partial Melt in Granite (ppm)		
Degree of melting				
1%	24500	44000	24500	44000
2%	12250	22000	12250	22000
5%	4900	8800	4900	8800
		Amounts of Assimilation (wt.%)		
Degree of melting				
1%	0.03	0.13	0.02	0.16
2%	0.06	0.25	0.04	0.32
5%	0.16	0.64	0.11	0.80

*Composition of representative granite is after *Johannes and Holtz* (1996).

3-9. Origin of the Tanetomi Magma

Petrological and mineralogical features suggest that the least differentiated rocks in the Tanetomi lava cannot be in equilibrium with mineral assemblage present in the mantle. The Tanetomi magma should have been, therefore, evolved before forming the observed compositional variation of the lava in the magma chamber at about 2 kbar. In this section, origin of the Tanetomi magma is considered, and it is shown that the Tanetomi magma could have been a derivative magma of the Kutsugata magma.

The Tanetomi lava erupted at the same stage of the volcanic activity as that of the Kutsugata lava, and therefore the Kutsugata magma is one plausible origin of the Tanetomi magma. This is supported by the following facts: (1) both the Kutsugata and Tanetomi lavas erupted from the western flank of Mt. Rishiri (Fig. 2-1); (2) the estimated pressure at the depth of the magma chamber is about 2 kbar for both the Kutsugata and Tanetomi magmas; and (3) the concentration pattern of incompatible trace elements of the Tanetomi lava is remarkably similar to that of the Kutsugata lava (Fig. 3-3).

The points (1) and (2) imply that the Tanetomi lava was differentiated in the magma chamber in which the Kutsugata magma was resided. The point (3) strongly suggests that the Tanetomi magma was produced principally by crystal fractionation from the Kutsugata magma. Positive anomalies of La, Pb, Zr, and Li, and negative anomalies of Nb and Ta are common in the Kutsugata and Tanetomi lavas. The concentrations of the incompatible elements are higher in the Tanetomi lava than in the Kutsugata lava, which is expected from the crystal fractionation from the Kutsugata magma. Successive increase of Pb and Li from the least differentiated Kutsugata magma to the most differentiated Tanetomi lava, most of which were derived from the surrounding crust, suggests that the evolution of the Kutsugata and Tanetomi magmas was continuous. Both the Kutsugata and Tanetomi magmas were aphyric in the magma chamber though phenocryst assemblage is different, which also supports the supposed origin of the Tanetomi lava.

3-10. Evolution of the "Kutsugata Magma System"

3-10-1. Crystal fractionation

Broad compositional gap is present between the most differentiated samples in the Kutsugata lava (Km-11 in Table 2-1) and the least differentiated samples in the Tanetomi lava (Kk-5 in Table 3-1) with up to 5 wt.% in SiO_2 content (Fig. 3-17). The crystal fractionation modeling using whole-rock major elements suggests that composition trend of the South lava II requires separation of plagioclase, olivine, and augite (Table 2-7). Fractionation of hornblende is also suggested from the variation of the incompatible trace elements (Fig. 2-23). On the other hand, composition trend of the Tanetomi lava is explained by fractionation of plagioclase, hornblende, titanomagnetite, and apatite. During the compositional evolution from the Kutsugata magma to the Tanetomi magma, fractionation phases, their proportions, and mineral compositions should have been significantly changed.

Possible compositional evolution between the observed whole-rock compositions of the Kutsugata and Tanetomi lavas is shown on Fig. 3-17, which depicted manually by utilizing the slopes of the composition trends of the both lavas. TiO_2 content increases in the Kutsugata lava, but it might start to decrease at the magma with slightly more differentiated composition than the South lava probably by fractionation of titanomagnetite. P_2O_5 content increases progressively with compositional evolution, and then separation of apatite suppresses enrichment of the P_2O_5 content in the magma. The P_2O_5 content might be the maximum at the composition of the

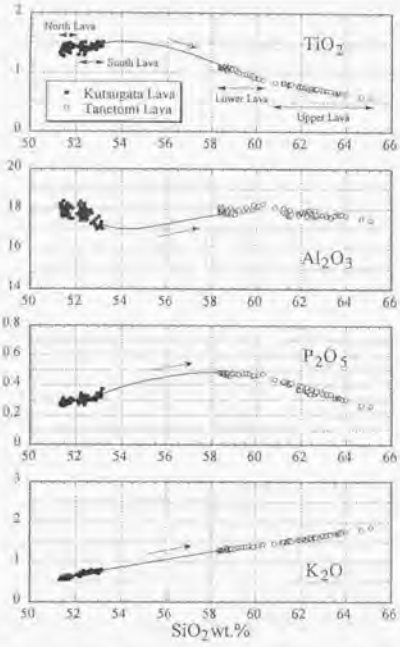

Figure 3-17. Whole-rock composition trend of the Kutsugata and Tanetomi lavas for some elements, along with the possible compositional evolution between the Kutsugata and Tanetomi lavas.

Lower lava. In the South lava, Al_2O_3 content decreases with an increase of SiO_2 content, whereas it increases with SiO_2 content in the Lower lava. Thus the Al_2O_3 content is considered to increase during the evolution in the compositional gap. During the evolution of the Kutsugata magma, fractionated mineral phases were olivine and plagioclase until the magma evolved to the composition of the South lava II. Then augite and hornblende became stable mafic phases instead of olivine in the boundary layer, and appearance of augite might have suppressed the crystallization of plagioclase as a Ca-bearing phase. Separation of titanomagnetite, augite, and hornblende has been dominant relative to the fractionation of plagioclase until the magma evolved to the composition of the Lower lava. In fact, crystal fractionation model suggests more significant fractionation of hornblende than plagioclase in the LL1, contrary to the case of the Upper lava. K_2O content increases progressively throughout the compositional evolution, because it is incompatible for all fractionated phases; olivine, plagioclase, hornblende, augite, titanomagnetite, and apatite. The variation of the fractionated mineral phases during evolution of the Kutsugata magma system was thus olivine + plagioclase → olivine + plagioclase + augite → olivine + plagioclase + augite + hornblende → plagioclase + augite + hornblende + titanomagnetite → plagioclase + hornblende + titanomagnetite + apatite. Figure 3-18 summarizes the estimated magmatic temperatures for both the Kutsugata and Tanetomi lavas plotted as a function of whole-rock SiO_2 content. Temperature decreases progressively from 1110 °C (the least differentiated Kutsugata magma) to 920 °C (the most differentiated Tanetomi magma).

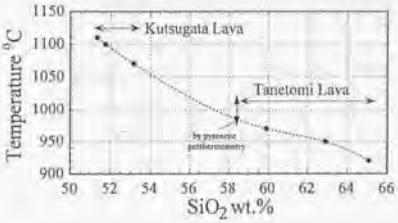

Figure 3-18. Temperature evolution of the main magma at the Kutsugata magma system. Solid circles are the estimations based on the crystal-melt thermodynamic equilibria. Estimation by pyroxene geothermometry is shown with arrow.

3-10-2. Crustal assimilation

In the magma chamber during residence of both the Kutsugata and Tanetomi magmas, assimilation of crustal materials is suggested to have occurred. Figure 3-19 shows the degree of assimilation as a function of the SiO_2 content, which is defined as the difference of Cs concentration of the actual samples from that calculated by crystal fractionation model, normalized by the concentration in the sample Fm-57 of the Kutsugata lava. Cs is used, because this mostly behaves as a completely incompatible element. The variation in Fig. 3-19 suggests that the crustal materials assimilated to the magma chamber progressively throughout the evolution of the Kutsugata magma system.

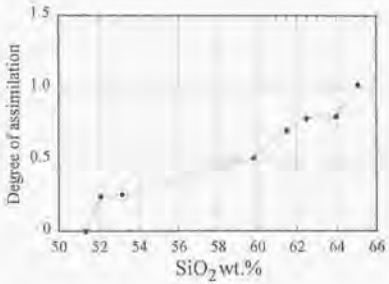

Figure 3-19. Normalized difference of the concentrations in the representative samples from those expected from the crystal fractionation, plotted against the whole-rock SiO_2 content. See text for the details.

Figure 3-20 shows the variation of the Sr, Nd, and Pb isotopic compositions with the whole-rock SiO_2 content. The $^{87}Sr/^{86}Sr$ ratio of the Tanetomi lava is significantly higher than that of the Kutsugata lava. In spite of the analytical uncertainty, the $^{87}Sr/^{86}Sr$ ratio in the Kutsugata lava tends to increase with the SiO_2 content. The $^{87}Sr/^{86}Sr$ of the Tanetomi lava seems to be on the extrapolation from the trend of the Kutsugata lava. This feature is also observed in the variation of the $^{143}Nd/^{144}Nd$ ratio. The ratio decreases progressively with the SiO_2 content, though the analytical uncertainty is large relative to the variation of the ratio. The $^{206}Pb/^{204}Pb$ and $^{208}Pb/^{204}Pb$ ratios in the Kutsugata lava vary abruptly with the SiO_2 content except for the most differentiated sample in the lava. The variation in the Tanetomi lava is not so large as that of the Kutsugata lava. This is consistent with the feature of the variation of the Pb concentration, such that the excess Pb which derived from the assimilated materials was higher in the Kutsugata lava than in the Tanetomi lava (Figs. 2-23 and 3-16). The $^{207}Pb/^{204}Pb$ ratio increases gradually throughout the evolution of the Kutsugata magma system, except for the one sample in the Kutsugata lava. The sample Km-11 was collected from sea cliff, and thus it might have affected by sea water.

The isotopic composition of Pb in the assimilated materials can be roughly calculated by utilizing the observed concentration of Pb, observed isotopic composition, and the calculated excess Pb derived from the assimilation, which is the difference of the observed Pb from that expected from the crystal fractionation. The ratio is estimated for both the Kutsugata and Tanetomi lavas. The sample Fm-57 and Kr-9 is used as a parental and daughter composition, respectively, in the Kutsugata lava. Similarly, the sample Kr-64 and Kk-31 is used as a parental and daughter composition for the UL2 of the Tanetomi lava (Table 3-11). The calculated isotopic composition of the assimilated materials is principally similar for both the Kutsugata and Tanetomi lavas, considering the uncertainty of the calculation such as the data of partition coefficient.

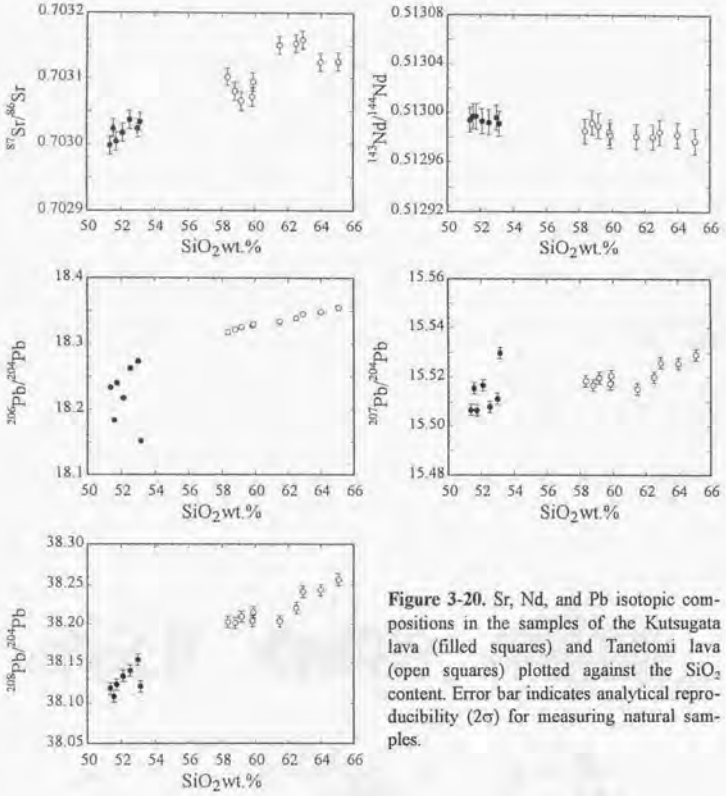

Figure 3-20. Sr, Nd, and Pb isotopic compositions in the samples of the Kutsugata lava (filled squares) and Tanetomi lava (open squares) plotted against the SiO_2 content. Error bar indicates analytical reproducibility (2σ) for measuring natural samples.

Table 3-11. Estimated Isotopic Compositions of Pb in the Assimilated Materials

	Kutsugata lava			Tanetomi lava		
	Fm-57	Kr-9	Crust	Kr-64	Kk-31	Crust
Pb, ppm	2.42	3.37	*0.36	6.83	7.68	*0.57
$^{206}Pb/^{204}Pb$	18.234	18.273	18.538	18.345	18.355	18.475
$^{207}Pb/^{204}Pb$	15.507	15.511	15.540	15.526	15.529	15.568
$^{208}Pb/^{204}Pb$	38.119	38.154	38.392	38.241	38.256	38.435

*Pb content in the "Crust" indicates the content of the excess Pb in the magmas which derived from the assimilated materials.

3-10-3. Evolution of the Kutsugata magma system

The eruption history of the Kutsugata magma system is summarized in Fig. 3-21. After injection of the primary Kutsugata magma into the magma chamber at about 2 kbar (Fig. 3-21a), it was differentiated by boundary layer fractionation. In the boundary layer, An-rich plagioclase and low-Ni olivine were crystallized (Fig. 3-21b). After the discharge of the magma as the North lava, the composition of the remaining magma was again evolved through boundary layer fractionation (Fig. 3-21c). Fractionation of augite and hornblende, probably present in the deep mush zone, started to control the compositional evolution of the main magma, in addition to olivine and plagioclase. The magma partly ascended from the magma chamber and erupted as the South lava (Fig. 3-21c). The compositional evolution of the remaining magma was proceeded from basaltic to andesitic compositions, without tapping of the magma chamber.

Before replenishment of the basaltic magma, the andesite magma is considered to have formed a series of compositional trend in the magma chamber. Plagioclase of the clear type was present in the main part of the magma body, and Ab-rich plagioclase, hornblende, and titanomagnetite were crystallized in the mushy boundary layer (Fig. 3-21d). Soon after the replenishment of the basaltic magma, tapping of the magma chamber occurred and the LL1 magma discharged before mixing with the basaltic magma (Fig. 3-21e). The remaining felsic magma mixed with the basalt magma (Fig. 3-21f), and the mixed magma erupted as the LL2 during a short interval (Fig. 3-21g). After the eruption of the Lower lava, compositional variation of the magma was again produced by boundary layer fractionation (Fig. 3-21h). Only in the least differentiated samples in the UL1, the An-rich plagioclase is very rarely present. This suggests that additional injection of basaltic magma might have occurred, which again triggered the eruption of the Upper-lava magma (Fig. 3-21i).

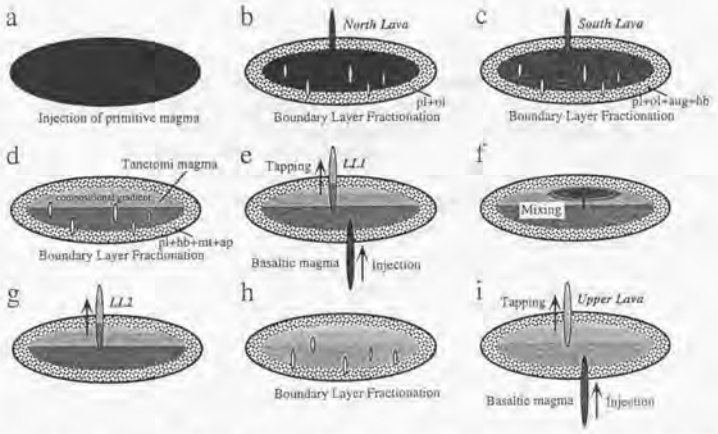

Figure 3-21. Summary of the evolution of the Kutsugata magma system, from the Kutsugata magma to the Tanetomi magma. See text for the details.

4. Modeling of Magmatic Differentiation

As demonstrated in the previous chapters, boundary layer fractionation may be a fundamental fractionation process in magmatic evolution, because a magma is cooled from the surrounding crust and crystallization primarily occurs along the chamber walls. Previous boundary layer fractionation models (*Langmuir,* 1989; *Nielsen and DeLong,* 1992; *O'Hara and Fry,* 1996) have shown that the compositional evolution of a magma by boundary layer fractionation can be fairly different from that of a homogeneous fractionation, wherein crystals formed homogeneously throughout the cooling magma chamber are separated from the magma. However, previous models are qualitative in that they do not include physical constraints such as the thermal structure of a boundary layer.

In this chapter, a boundary layer fractionation model for the thermal and compositional evolution in a cooling magma body is presented. In this model, the thermal structure of a boundary layer is determined by heat balance between the cooling magma and the surrounding wall rock. Spatial variations in phase assemblage, phase proportions, and chemical compositions are calculated by thermodynamic solution models (e.g., *Ghiorso and Sack,* 1995). The composition of a fractionated melt extracted from the mush zone is controlled by the compositional structure of the evolving boundary layer. This model enables to perform a realistic simulation of magmatic differentiation as a function of time and space.

4-1. Modeling

Consider a layer of crystal-free basaltic magma emplaced into the semi-infinite crust. The model assumes a sill-like magma body in which heat loss from the vertical walls of the reservoir is negligible. Heat transfer from the magma chamber is assumed to occur simply by conduction, because much geological evidence favors conductive cooling rather than convective cooling (*Helz et al.,* 1989; *Marsh,* 1989). This view is further examined in the Section 4-5. The temperature profiles in the crust both above and below the magma body are given by

$$\frac{\partial T_s}{\partial t} = \kappa_s \frac{\partial^2 T_s}{\partial x^2} + \frac{L_s}{c_s}\frac{\partial \phi_s}{\partial t}(T_s), \tag{4-1}$$

and that of the magma body by

$$\frac{\partial T_m}{\partial t} = \kappa_m \frac{\partial^2 T_m}{\partial x^2} + \frac{L_m(C,T_m)}{c_m}\frac{\partial \phi_m}{\partial t}(C,T_m), \tag{4-2}$$

where T is the temperature, κ is the thermal diffusivity, L is the latent heat of crystallization, c is the specific heat, ϕ is the crystallinity, C is the magma composition, and subscripts s and m denote crust and magma, respectively. Conservation of heat at the crust-magma interface is

$$\rho_s c_s \kappa_s \left.\frac{\partial T_s}{\partial x}\right|_{z=0,D} = \rho_m c_m \kappa_m \left.\frac{\partial T_m}{\partial x}\right|_{z=0,D} \qquad (4\text{-}3)$$

where ρ is the density.

The values for the physical parameters adopted here are: $\kappa_s = \kappa_m = 8 \times 10^{-3}$ cm^{2}s^{-1}, $c_s = c_m = 1.3$ J gm^{-1}K^{-1}, $\rho_s = 2.3$ gm cm^{-3}, $L_s = 300$ J gm^{-1} (*Huppert and Sparks*, 1988). The solidus of the crust is assumed to be 600 °C, but no movement of crustal melt is assumed. The liquidus volume change, $d\phi_l/dT$, is approximated to be -4.0×10^{-3} K^{-1}. The density, latent heat of crystallization, and crystallinity of the magma are obtained as a function of local magma composition and temperature by thermodynamic calculations as described below. The heat conduction equations are numerically solved by the Crank-Nicolson finite difference method. The number of computing grid cells is 400 within the magma chamber, and 200 for the crust both above and below the magma body.

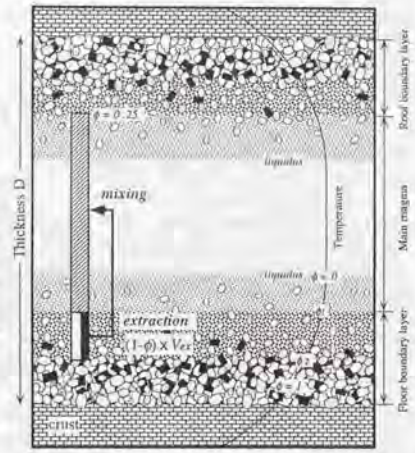

Figure 4-1. Schematic illustration of a magma chamber, showing the procedure of numerical model of boundary layer fractionation. The interstitial melt within the mush zone in which crystallinity ranges from ϕ_1 to ϕ_2 is extracted with a volume fraction V_{ex}, and is mixed homogeneously with the main magma ($\phi < \phi_1$ at the floor and $\phi < 0.25$ at the roof). Schematic temperature profile is also shown. See text for the details.

To examine compositional evolution of natural magmas, chemical composition is calculated in the multicomponent system. Analysis of series of drill holes in the Hawaiian lava lakes (e.g., *Helz and Thornber*, 1987; *Helz et al.*, 1989) shows that local thermodynamic equilibrium was attained even in the mush zone (*Tait and Jaupart*, 1996). Therefore, in the model developed here, it is assumed that equilibrium phase assemblages, proportions, and compositions are determined by local magma composition and temperature. For each individual model grid cell and at each time step, phase proportions and compositions are calculated by using the thermodynamic solution models for olivine of *Hirschmann* (1991), for plagioclase of *Elkins and Grove* (1990), for augite of *Sack and Ghiorso* (1994a and b), and for silicate melt of *Ghiorso and Sack* (1995). The volume fraction of mineral phases is calculated from their weight fractions after *Lange and Carmichael* (1990). Because NaSi-CaAl diffusion in plagioclase is very slow (*Grove et al.*, 1984) and because plagioclase crystals are zoned in terms of An content, calculations were performed with approximation of fractional crystallization in each grid cell. Though olivine is likely to be

homogenized in Mg# due to relatively large Fe-Mg interdiffusion rate (*Jurewicz and Watson*, 1988) and hence a calculation using batch crystallization is more plausible, this does not significantly affect the result because of small phase proportion of olivine compared with plagioclase. Although other phases, such as accessory minerals, may appear in the low-temperature deep mush zone, they do not affect the model because only the mush zone with crystallinity <50 vol.% is important as is described below. Crystallinity greater than 50 % is approximated to increase linearly with temperature up to 100 % at the assumed solidus of 900 °C. The latent heat of crystallization is obtained from *Berman* (1988) at individual time steps in the calculation, which, together with the liquidus volume change, constrains the heat conduction equation (4-2) below 50 % crystallinity. At a crystallinity larger than 50 %, latent heat is fixed to be 500 J gm^{-1}.

Because the Kutsugata magma is hydrous, water-saturation may be achieved within a mush zone. The vapor phase in one computing grid cell is transported to the overlying cell, and this is repeated until it is completely dissolved. Water solubility as a function of pressure, temperature, and melt composition is calculated from the model of *Moore et al.* (1998). The $Fe^{3+}/(Fe^{2+}+Fe^{3+})$ ratio is calculated after the method of *Sack et al.* (1980). The dissolution of water in silicate melt might have no effect on the redox state of the iron (*Moore et al.*, 1995).

In boundary layer fractionation, differentiated melt within the floor mush zone is extracted to mix with the overlying main magma (Fig. 4-1). This is approximated by assuming that the interstitial melt at the computing grids in which crystallinity falls within the range between ϕ_1 and ϕ_2 ($\phi_1 < \phi_2$; within the floor mush zone) is extracted with a volume fraction of V_{ex} relative to the total volume of interstitial melt at each grid, per 10 years (Fig. 4-1). This corresponds to the upward movement of interstitial melt as a convective plume, as suggested in Kilauea Iki lava lake (*Helz et al.*, 1989). Extraction of the interstitial melt from a deep mush zone may not be effective if deformation of an interconnected crystal network is required. This occurs at a critical crystallinity of 60-70 vol.% if the crystals are spherical, but at about 50 vol.% in the case of actual magmas (e.g., *Marsh*, 1988). Thus, the upper limit of ϕ_2 is 0.5. The roof boundary layer does not chemically affect the underlying main magma. The transported fractionated melt from the floor mush zone is assumed to mix homogeneously with the main magma, where crystallinity is less than ϕ_1 in the upper part, and less than 25 vol.% in the lower part (Fig. 4-1). A crystallinity of 25 vol.% is adopted as the limit for the main magma below the roof mush zone, because the fractionated melt may mix easily with a magma containing <25 vol.% crystals (e.g., *Marsh*, 1996). Though homogeneous mixing of the differentiated melt is contrary to the assumption of conductive cooling, it does not affect the argument discussed in this chapter, because the absolute time of magmatic evolution is not discussed by using this model. The initial input parameters for the model are chamber thickness (D), the pressure at

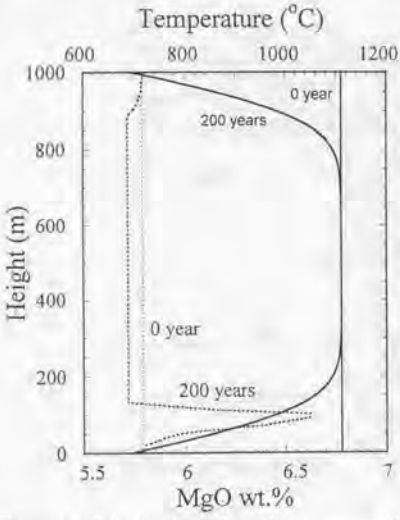

Figure 4-2. Calculated variations of temperature and MgO content of a magma across the magma chamber at 0 and 200 years, for $\phi_1 = 0.1$, $\phi_2 = 0.5$, and $V_{ex} = 0.05$.

the depth of the magma chamber (P), magma composition (C_{m0}), temperature of the magma (T_{m0}), temperature of the crust (T_{s0}), the values of ϕ_1 and ϕ_2, and the value of V_{ex}.

4-2. Application to the Kutsugata Lava

The model is applied to the North-lava magma to show that the observed composition trends are controlled by boundary layer fractionation. The feature of the boundary layer fractionation is also discussed by examining the effect of model parameters on the compositional evolution of magmas.

It is assumed that a layer of homogeneous basaltic parental magma of the North lava (Table 2-6) with thickness 1 km (D) is emplaced into the crust at 2 kbar (P). The oxygen fugacity of NNO buffer is assumed. The initial magma temperature is 1110 °C (T_{m0}) and the water content is 4 wt.%. The crust is assumed to be initially uniform in temperature at 200 °C (T_{s0}). Figure 4-2 shows typical temperature and composition profiles across the reservoir. The bulk MgO content increases in the lower part of the mush zone, and decreases in the main magma body, because of the transportation of differentiated melt. This profile is similar to that observed I analogue experiments using aqueous solutions (*Chen,* 1995), which were design to investigate the nature of convection in a floor boundary mushy layer by cooling from the bottom of the tank.

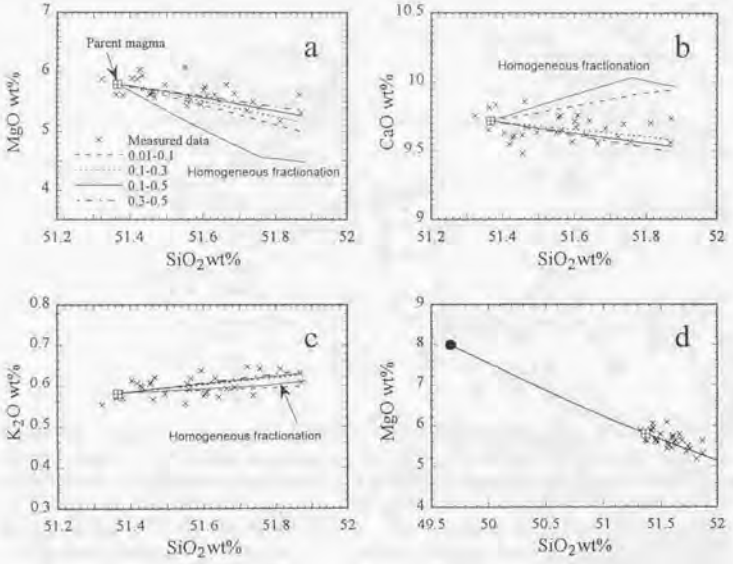

Figure 4-3. Comparison of measured data with the calculated composition trends by boundary layer fractionation for various ϕ_1 and ϕ_2, and those by homogeneous fractionation. The homogeneous fractionation model can not reproduce the observed trends. This holds true when the initial composition is more primitive than the least differentiated rocks of the Kutsugata lava (d).

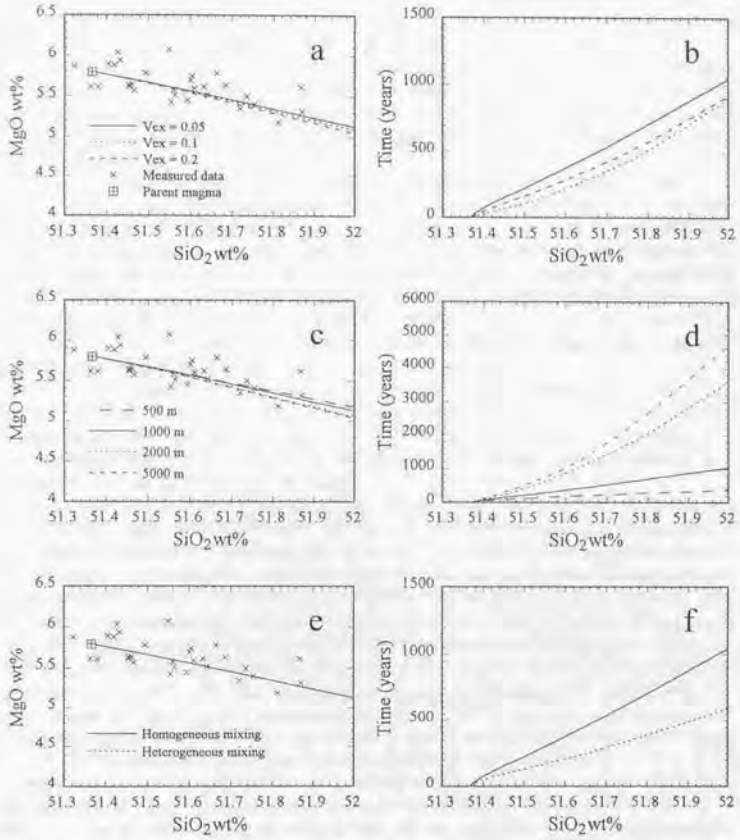

Figure 4-4. Comparison of the modeled composition trends and variation of time as a function of the SiO_2 content in the main magma ($\phi_1 = 0.1$, $\phi_2 = 0.5$), with various V_{ex} for chamber thickness of 1000 m and homogeneous mixing model of differentiated melt (a and b), with various chamber thickness for $V_{ex} = 0.05$ and homogeneous mixing model (c and d), and with different mixing models for $V_{ex} = 0.05$ and chamber thickness of 1000 m (e and f). In the heterogeneous mixing model, fractionated melt from the mush zone is mechanically mixed with the main magma so that a linear spatial compositional variation is formed in the main magma. The SiO_2 content in (e) and (f) represents the maximum value in the main magma.

The calculated composition trends of the main magma are shown in Fig. 4-3 for various values of ϕ_1 and ϕ_2, and $V_{ex} = 0.05$, together with that for homogeneous fractionation. Homogeneous fractionation does not reproduce the observed trends. This is because plagioclase does not appear as a liquidus phase until the temperature reaches about 1050 °C. When the melt is extracted from the relatively shallower interior of the mush zone ($\phi_1 = 0.01$, $\phi_2 = 0.1$ in Fig. 4-3), the modeled trends do not reproduce the observed MgO and CaO contents well. This result is consistent with the suggestion that the average crystallinity of the mush zone where the differentiated melt of the North-lava magma was derived is more than about 30 % ($\phi > 0.3$). The trends calculated with the values of $\phi_1 = 0.1$ and $\phi_2 = 0.5$ give the best fit for the observed ones in all major elements.

Settling of olivine crystals from the main magma may have occurred, simultaneous with boundary layer fractionation. Homogeneous olivine fractionation trend could be counterbalanced by boundary layer fractionation trend with high ϕ_1 and ϕ_2 (extraction of the fractionated melt from the deep mush zone), which would form observed composition trends. If the contribution of homogeneous olivine fractionation is considerable, the boundary layer fractionation trend needs to deviate significantly from the observed composition trend so as to offset the homogeneous fractionation trend. However, the boundary layer fractionation trend with high ϕ_1 and ϕ_2 ($\phi_1 = 0.3$ and $\phi_2 = 0.5$) does not deviate significantly from the observed trend, suggesting that the contribution of homogeneous olivine fractionation has been negligible.

These calculations assume that the magma with the parent composition (shown in Table 2-6) intruded the reservoir, but the initial magma could have been more primitive than this parent composition. Fractionation is again modeled by using a more primitive composition as a starting magma (filled circle in Fig. 4-3d). Boundary layer fractionation with the values of $\phi_1 = 0.1$ and $\phi_2 = 0.5$ can again reproduce the trends.

The calculated trends with $V_{ex} = 0.05$, 0.1, and 0.2 are shown in Fig. 4-4a. Within the compositional range of the North lava (0.6 wt.% in SiO_2), the variation of V_{ex} is not sensitive to the resulting compositional evolution, and the value of V_{ex} cannot be constrained from the observed trends. The values of V_{ex}, however, slightly affect the time scale of the differentiation at a given chamber thickness (Fig. 4-4b). Variation of the initial chamber thickness is mostly independent of the compositional evolution between 500 and 5000 m (Fig. 4-4c). On the contrary, it strongly correlates with the time scale in which the compositional variation is produced (Fig. 4-4d). These calculations assume that the differentiated melt from the mush zone is mixed homogeneously with the overlying main magma. In actual processes, however, differentiated melt may not mix perfectly and a spatial compositional gradient would be formed in the main magma body. The compositional evolution is also calculated and shown in Fig. 4-4e (heterogeneous mixing model). In this calculation, fractionated melt extracted with a volume fraction $V_{ex} = 0.05$ is mixed with the main magma at each time step so as to form a linear compositional gradient in the main magma body. The base of the main magma is assumed not to mix with the fractionated melt in this case, and the larger quantity of melt is mixed with the upper part of the main magma. Compositional evolution by heterogeneous mixing model cannot be distinguished from that of homogeneous mixing model. The time scale to produce the same range of compositional variation could be reduced compared with the homogeneous mixing case (Fig. 4-4f).

Figure 4-5 shows the Mg# of the fractionated olivine during differentiation, along with that of equilibrium olivine with the whole-rock composition. Though the magma can coexist with >Mg#85 olivine, it actually fractionates olivine with a much lower Mg# of less than 80, as stated above. The calculated Mg# is in good agreement with Mg#77.1±1.1, which is estimated from the compositional trend (Fig. B-1). The Mg# of olivine in equilibrium with differentiated melt is initially as low as 74, and gradually increases to 80. This reflects the fact that the bulk composition of the boundary layer tends to become more magnesian by releasing residual melt (Fig. 4-2), and so the composition of the differentiated melt also becomes magnesian.

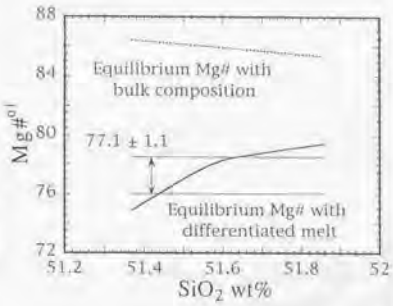

Figure 4-5. Mg# of olivine in equilibrium with bulk composition (broken line) and with differentiated melt (continuous line) shown against the whole-rock SiO_2 content. The range of 77.1±1.1 indicates the constraints derived from the natural observation (Fig. B-1a), which is in good agreement with calculated value.

4-3. Application to the Evaluation of Primary Magma Estimation

The pressure and temperature conditions of magma generation can be commonly deduced by finding the conditions at which a primary magma can coexist with mineral phases present in the mantle (e.g., *Tatsumi et al.*, 1983; *Bartels et al.*, 1991). However, basaltic magmas are typically differentiated to various extents due to fractional crystallization, so primary magma compositions must be estimated from derivative basalts. A common method for estimating a primary composition is to add equilibrium olivine to the least differentiated basalt compositions until a calculated composition can coexist with mantle olivine (Mg#89-92) ("olivine maximum fractionation model" e.g., *Tatsumi et al.*, 1983; *Albarède*, 1992; *Fram and Lesher*, 1997). However, the estimated composition would be different from the true primary composition if the magma fractionated phases other than olivine, for example, by boundary layer fractionation. The model presented above permits a quantitative evaluation of the compositional differences expected between these two differentiation mechanisms.

First, it is assumed that a primary magma generated in the mantle ascends to form a magma chamber, in which the magma is differentiated by either homogeneous fractionation (HF) or boundary layer fractionation (BLF). The initial parameters for calculating the BLF trend are D = 1000 m, P = 2 kbar, T_{s0} = 200 °C, ϕ_1 = 0.1, ϕ_2 = 0.5, and V_{ex} = 0.5. An experimentally produced partial melt of dry peridotite (Table 4-1: KLB-1 run 14; *Hirose and Kushiro*, 1993) is used as an

Table 4-1. Comparison of Actual Primary Composition with the Calculated Composition from Several Differentiated Magmas on the Boundary Layer Fractionation Trend by Olivine Maximum Fractionation Model

		SiO_2	TiO_2	Al_2O_3	FeO	MnO	MgO	CaO	Na_2O	K_2O
Actual primary magma*	(89)	51.33	1.09	19.09	6.38	0.23	8.14	8.85	4.60	0.27
Estimated primary magma	(88)	51.43	1.18	18.31	6.75	0.23	8.56	8.54	4.70	0.29
	(87)	51.48	1.26	17.56	7.10	0.24	9.01	8.26	4.77	0.31
	(86)	51.50	1.33	16.91	7.42	0.24	9.41	8.01	4.82	0.33
	(85)	51.51	1.41	16.24	7.76	0.24	9.84	7.76	4.87	0.35

Actual primary magma* is KLB-1 run 14 of *Hirose and Kushiro* (1993). Numbers in parentheses are equilibrium Mg# of olivine.

initial magma. This model primary magma is in equilibrium with Mg#89 olivine. The initial magma temperature is 1250 °C, which is the liquidus temperature at 2 kbar.

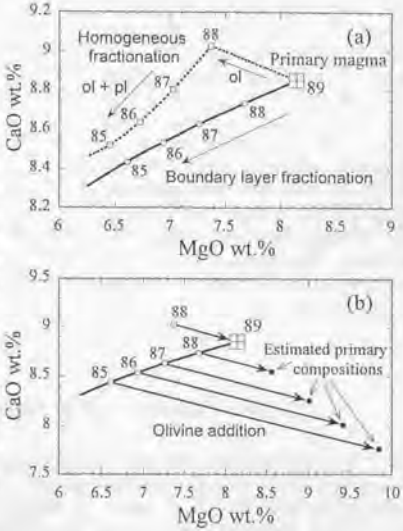

Figure 4-6. (a) Fractionation trends from a primary magma. The heavy continuous line shows the boundary layer fractionation (BLF) trend, and the heavy dashed line is for homogeneous fractionation (HF). Open circles and open squares show the composition of equilibrium olivine that coexists with melt along the trends. (b) The heavy arrows show calculated olivine addition lines for estimating a primary magma for a magma which differentiated by BLF. The solid circles show calculated primary magmas from the differentiated magmas on the BLF trend. If the magma is on the HF trend and only olivine is the crystallizing phase (open square), the olivine maximum fractionation model gives the actual primary magma composition.

The calculated composition trends for both fractionation models are shown on Fig. 4-6a. In the early stages of crystallization, the CaO content increases in the HF model with a decrease in MgO content because only olivine is crystallizing. In contrast, CaO decreases in the BLF model because plagioclase crystallizes and is separated, together with olivine. In the HF trend a sharp inflection is present at the point where plagioclase appears as a liquidus phase, after which CaO decreases with further decrease in MgO.

Now, consider the effect of calculating a primary magma composition by olivine addition when, in fact, the derivative magmas are products of BLF. The magma compositions that can coexist with Mg#89 olivine ("primary magma") are calculated for several differentiated magmas along the BLF trend by using the olivine maximum fractionation model (Fig. 4-6b, Table 4-1). The estimated "primary magma" compositions can deviate significantly from the true primary composition. The deviation becomes larger as the Mg# of the derivative magma decreases. Though 19 wt.% crystals are fractionated from the true primary magma to the differentiated magma in equilibrium with Mg#86 olivine through BLF, addition of only 6 wt.% olivine to this magma would be predicted to make the "primary magma". This results in the overestimation of incompatible elements, such as TiO_2 and K_2O, in the estimated composition using the olivine maximum fractionation model (Table 4-1). The estimation from the magma on the HF trend gives the true primary composition if olivine is the sole crystallizing phase. If the magma crystallizes along a cotectic involving olivine and plagioclase, the estimated composition also deviates from the true primary magma (although not shown in Fig. 4-6b).

The temperature and pressure conditions necessary to generate the fictive "primary

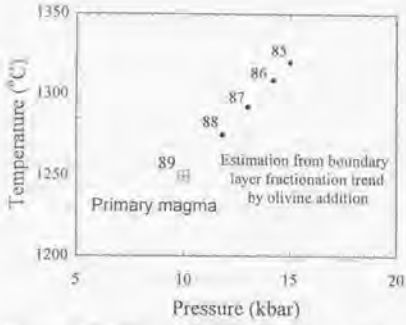

Figure 4-7. Differences between the actual conditions of generation of the primary magma, and conditions estimated from primary magmas by olivine addition to magmas along the BLF trend.

magmas" estimated by the olivine addition procedure are obtained from the experimental study of *Hirose and Kushiro* (1993) (Fig. 4-7). Though the actual primary magma is experimentally produced at 1250 °C and 10 kbar, the estimated "primary magma" starting with the magma in equilibrium with Mg#86 olivine would be produced around 1300 °C and 15 kbar. Thus, the olivine addition procedure causes a significant overestimation of the pressure and temperature conditions of magma generation in this case where the magma actually differentiated by boundary layer fractionation. An overestimation of the abundance of incompatible elements would also result in an underestimation of the degree of partial melting.

4-4. Primary Magma Composition of the Kutsugata Lava

The results of the evaluation of primary magma estimation demonstrate that the specification of differentiation mechanism from a primary magma to an erupted derivative magma is crucial to know the true primary magma composition precisely. In this section the primary magma composition of the Kutsugata lava is estimated using the boundary layer fractionation model and the constraint of trace elements. It is assumed that the primary Kutsugata magma generated in the mantle was stored in the magma chamber at 2 kbar, and that the observed composition trend of the lava was established by boundary layer fractionation. During ascent of the primary magma to the magma chamber, olivine might have crystallized because of a decrease in temperature due to the heat loss through the surrounding rocks and the thermal expansion of the magma. Such olivine crystals are, however, considered to have removed from the magma soon after the injection into the magma chamber (homogeneous fractionation; *Marsh*, 1996).

The primary magma is assumed to be in equilibrium with Mg#89 olivine. First, the primary magma composition is estimated for the case of no olivine crystallization and fractionation during the ascent. Many forward calculations are performed by boundary layer fractionation model from various starting compositions which can equilibrate with Mg#89 olivine. The primary composition is the starting composition which minimizes the errors in reproducing the observed composition trends of the Kutsugata lava in all major elements (Table 4-2; filled diamond with error bars in Fig. 4-8). Next, the effect of olivine crystallization and its fractionation is taken into account, and the range of possible primary magma (light curved line indicated by "possible range") is calculated from the magma compositions on the boundary layer fractionation trend (heavy curved line) by incremental addition of equilibrium olivine. The primary magma on the light curved line (filled circle, for example) would fractionate olivine crystals soon after the emplacement into the magma chamber and changes its bulk composition (filled square), and then the magma composition evolves on the boundary layer fractionation trend (heavy curved line). The extreme case is the composition (Table 4-2; open circle in Fig. 4-8) estimated by the olivine addition from the least differentiated rocks (open square with plus), in which the boundary layer

fractionation of the Kutsugata magma was started from the magma with the least differentiated rocks after the homogeneous olivine fractionation.

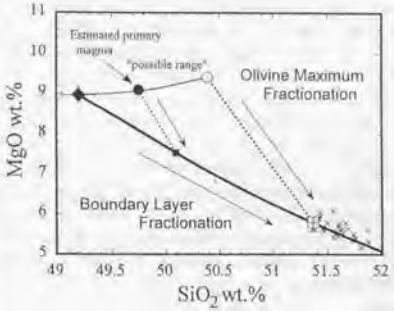

Figure 4-8. Estimated primary magma composition of the Kutsugata lava (filled circle) and calculated boundary layer fractionation trend on MgO-SiO_2 diagram. The measured data of the North lava are also shown by crosses. The filled diamond with standard errors indicate the primary magma composition by only boundary layer fractionation model. Open circle denotes primary magma composition estimated by only olivine maximum fractionation model from the least differentiated sample in the Kutsugata lava (open square with plus). The range of primary magma composition calculated by olivine maximum fractionation model from the magmas on the boundary layer fractionation trend is shown as light curved line ("possible range").

The primary magma composition on the "possible range" is specified uniquely by using incompatible trace elements of whole-rocks. In the MORB-normalized pattern, the positive anomaly of Li is observed (Figs. 2-4 and 4-9). This excess lithium could be derived from the surrounding crust during residence in the magma chamber and/or the wedge mantle during magma generation wherein Li might have transported by H_2O-rich fluid phase released from the subducting slab. Lithium in the slab could be released by devolatilization of hydrous mineral at shallow level, however, it is no longer partitioned into the fluid phase at depth greater than the critical level and is retained and transported by the subducting slab to the deeper level (*Moriguti and Nakamura*, 1998). The critical depth might be <250 km in the Izu arc, Japan, according to *Moriguti and Nakamura* (1998). Thus the positive Li anomaly might not be produced during magma generation beneath Rishiri Volcano, which located 300 km above the Wadati-Benioff zone.

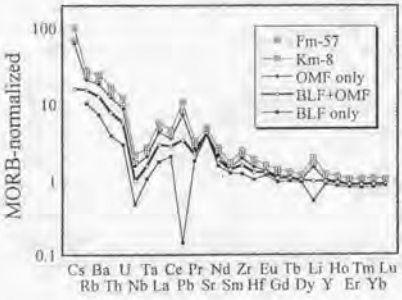

Figure 4-9. The MORB-normalized concentration of incompatible trace elements for the sample Fm-57 and Km-8, for the primary magmas estimated by olivine maximum fractionation model (OMF only) and by boundary layer fractionation model (BLF only), and for the plausible primary magma (BLF + OMF). The normalized concentration of Li is similar to that of Y in the plausible pri-

4. Modeling of Magmatic Differentiation

The composition of the primary magma is determined, given that the primary Kutsugata magma did not reside in crustal magma chambers other than the one located at 2 kbar and that the volume flux and composition of the crustal melt into the magma chamber was constant during boundary layer fractionation from the primitive magma to the Kutsugata magma. The normalized pattern of trace elements of magmas on the boundary layer fractionation trend can be calculated by using that of the Fm-57 and Km-8, assuming that the change of concentrations is proportional to the whole-rock SiO_2 content. This approximation may be valid because fractionation phase was olivine and plagioclase during boundary layer fractionation from the primary magma (filled diamond in Fig. 4-8) through the Fm-57 magma to the Km-8 magma. The Li/Y ratio of the magma is expected to be decreased as the whole-rock SiO_2 content decreases, because that of the sample Fm-57 is smaller than that of the Km-8. Therefore, the composition of the magma is found on the boundary layer fractionation trend, which satisfies the condition that the normalized Li is equivalent to that of Y. The SiO_2 content of this magma is 50.1 wt.% (filled square in Fig. 4-8). The plausible composition of the primary magma is obtained by incremental addition of equilibrium olivine to the magma until it coexists with Mg#89 olivine (filled circle in Fig. 4-8; Table 4-2). If the Kutsugata magma was differentiated only by boundary layer fractionation, the "primary magma" (filled diamond in Fig. 4-8; Table 4-2) exhibits negative Li anomaly. On the contrary, the positive Li anomaly is present in the "primary magma" (open circle in Fig. 4-8; Table 4-2) if the least differentiated Kutsugata magma was produced only by olivine maximum fractionation (Fig. 4-9). In the calculated normalized pattern of the estimated primary magma, the positive Pb and Sr anomalies are observed. This excess Pb and Sr may have been originated from subducting slab, as suggested by *Shibata and Nakamura* (1997).

The temperature and pressure conditions of magma generation are roughly estimated for the three "primary magmas" listed in Table 4-2 by using thermodynamic equilibria of olivine and silicate melt and that of augite and silicate melt. The generation condition is assumed such that the primary magma is saturated with both olivine and augite. The constraint of the saturation of orthopyroxene is not included. The result is given in Table 4-2. The plausible primary magma

Table 4-2. Comparison of Estimated Primary Magma Compositions and Magma Generation Conditions of the Kutsugata Lava by Different Fractionation Models

	Boundary Layer Fractionation		Olivine Maximum Fractionation
	BLF only	BLF + OMF	
	Primary Magma Composition (wt.%)		
SiO_2	49.20	49.75	50.39
TiO_2	0.93	1.05	1.22
Al_2O_3	19.21	18.16	16.57
Fe_2O_3	7.63	8.02	8.80
MnO	0.13	0.13	0.12
MgO	8.96	9.09	9.41
CaO	10.11	9.64	8.94
Na_2O	3.24	3.49	3.79
K_2O	0.40	0.45	0.52
P_2O_5	0.19	0.21	0.25
H_2O	2.52	2.87	3.32
	Generation Condition		
Pressure	11 kbar	13 kbar	16 kbar
Temperature	1275 °C	1290 °C	1320 °C

BLF denotes boundary layer fractionation and OMF indicates olivine maximum fractionation.

could be produced at 1290 °C and 13 kbar. The generation condition for the "primary magma" by olivine maximum fractionation model would give higher pressure and temperature estimation, similar to the result of the previous section (Fig. 4-7).

After the emplacement of the primary magma into the Kutsugata magma chamber, the liquidus temperature of the magma (filled square in Fig. 4-8) was 1180 °C for olivine, 1170 °C for plagioclase, and 1130 °C for augite (Note that plagioclase and augite appear as crystallization phases at temperature much lower than this "liquidus temperature" in actual liquid line of descent, because the liquidus temperature of one phase are calculated on the condition that any other phases are not present). The calculated liquidus temperature of plagioclase is much higher than that of the augite, and thus crystallization of augite is considered to have been suppressed by crystallization of plagioclase in the mushy boundary layer. This feature continued until the magma was differentiated to the North-lava composition. The boundary layer fractionation model shows that olivine was the sole liquidus phase in the mushy boundary layer until at a low temperature (from 1180 °C to 1100 °C), at which plagioclase with An87 appears as a crystallization phase. As discussed in the Section 2-6, increase of water content, suppression of crystallization of augite as a Ca-rich phase, and low temperature condition were satisfied in the boundary layer and therefore plagioclase with An-rich composition could have been crystallized.

4-5. Convective Vigor in the Kutsugata Magma Chamber

The nature of thermal convection in a crustal magma chamber is one of the most important problems in petrology. This is crucial for quantitative understanding of magma-chamber processes because cooling of the magma body, chemical differentiation of the magma, and degree of melting of the surrounding crust could be strongly controlled by the convection. If the thermal convection is essentially weak in a magma chamber, nucleation and growth of crystals primarily occur along the chamber walls and chemical differentiation of the magma results from the crystal-melt separation in the low-temperature boundary layer. If the convection is vigorous, on the contrary, crystals could occur in the main convecting magma even in the early stage of magmatic evolution. The compositional variation is thus controlled by crystal fractionation in the main magma as well as in the boundary layer. The strong heat flux through the roof crust promotes cooling of the magma body and could result in melting of the crustal materials, which may also affect the chemical evolution of the convecting main magma.

In spite of such a critical problem in petrology, the vigor of the thermal convection in magma bodies has been still controversial (e.g., *Marsh*, 1989; *Huppert and Turner*, 1991; *Marsh*, 1991). The studies of the nature of thermal convection have been mostly on experimental and theoretical analyses. *Worster et al.* (1990, 1993) demonstrated by application of the theoretical models developed by *Kerr et al.* (1990a, 1990b, 1990c) to a simple magmatic system that a kinetic undercooling at the mush-liquid interface is sufficient to drive vigorous convection in magma bodies. Recently *Hort et al.* (1999) carried out analogue experiments in which aqueous solution of isopropanol was cooled from the roof of the tank and suggested, on the contrary, that convection is essentially non-existent after the lost of initial superheat. Similar result was obtained from analogue experiment using paraffin by *Brandeis and Marsh* (1989).

Analogue experiments have a merit to elucidate some of the fundamental controls on convection and crystallization (e.g., *Hort et al.*, 1999), however, results of experiments could be dependent on the kind of aqueous solutions used, because aqueous solutions can never have all the same physical properties as actual magmas. Unlike simple aqueous solutions, magmas crystallize over a wide range of temperature (typically >200 °C) and are commonly multiply saturated. Furthermore length scale of crystals is negligible compared with that of the magma body (*Marsh*,

1996; *Hort et al.*, 1999). From these, it is necessary to extract direct information on the nature of thermal convection from the natural magmatic system. Analysis of series of drill holes in the Hawaiian lava lakes has provided excellent chance to investigate the role of thermal convection on the cooling of magma body. The measured evolution of the magmatic temperature and the roof crust were, however, fitted by any extreme theoretical models because of the large uncertainty of the data, and the vigor of the convection could not be constrained from the observation (*Hort*, 1997).

In this section, the convective vigor in a crustal magma chamber is estimated for the Kutsugata lava. To examine the nature of the thermal convection, the boundary layer fractionation model developed above is modified. Approach for incorporating the thermal convection into the model is different from that of the previous models; convective heat flux from the main magma is treated as a variable. This is because application of the well-known formula of convective heat flux (e.g., *Turner et al.*, 1986) to the multicomponent magmatic systems is not straightforward. The nature of the thermal convection is examined by comparing the observed thermal and compositional evolution of the magma chamber with the model calculations with various magnitude of convective heat flux.

4-5-1. Modeling

The mechanics of the model is principally similar to that presented above. Schematic illustration of the model is shown in Fig. 4-10. Heat transfer through the mushy boundary layer and the surrounding crust is assumed to occur by conduction. The heat conduction equation in the crust can be expressed as

$$\frac{\partial T_s}{\partial t} = \kappa_s \frac{\partial^2 T_s}{\partial x^2} + \frac{L_s}{c_s}\frac{\partial \phi_s}{\partial t} \tag{4-4}$$

and that of the mushy boundary layer as

$$\frac{\partial T_m}{\partial t} = \kappa_m \frac{\partial^2 T_m}{\partial x^2} + \frac{L_m(C_m, T_m)}{c_m}\frac{\partial \phi_m(C_m, T_m)}{\partial t} \tag{4-5}$$

where T is the temperature, κ is the thermal diffusivity, L is the latent heat of crystallization or melting, c is the specific heat, ϕ is the crystallinity, C is the magma composition, and subscripts s and m denote crust and magma, respectively. The bulk temperature of the convecting main magma evolves according to (e.g., *Kerr et al.*, 1990a)

$$c_l \cdot h \cdot \frac{dT_l}{dt} = -F_T - Q + L_l(C_l, T_l) \cdot h \frac{\partial \phi_l(C_l, T_l)}{\partial t} \tag{4-6}$$

where F_T is the convective heat flux through the roof boundary layer, Q is the heat source term to account for heat flux by transportation of the fractionated melt from the floor boundary layer, and subscript l denotes convecting main magma. Conservation of heat at the crust-magma interface is

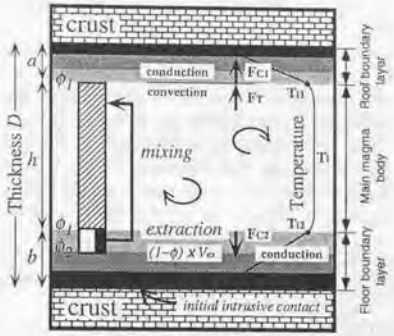

Figure 4-10. Schematic illustration of a magma chamber, showing the procedure of numerical model of boundary layer fractionation including thermal convection. The interstitial melt within the mush zone in which crystallinity ranges from ϕ_1 to ϕ_2 is extracted with a volume fraction V_{ex}, and is mixed homogeneously with the main magma ($\phi < \phi_1$). Schematic temperature profile is also shown. See text for the details.

$$\rho_s c_s \kappa_s \left.\frac{\partial T_s}{\partial x}\right|_{x=0,D} = \rho_m c_m \kappa_m \left.\frac{\partial T_m}{\partial x}\right|_{x=0,D} \tag{4-7}$$

where ρ is the density. At the interfaces between the roof boundary layer and main magma, conservation of heat requires that

$$\{c_m(T_l - T_{l1}) + L_m(C_m, T_m)\phi_1\}\frac{da}{dt} = F_{C1} - F_T \tag{4-8}$$

and that of between the floor boundary layer and main magma is

$$\{c_m(T_l - T_{l2}) + L_m(C_m, T_m)\phi_1\}\frac{db}{dt} = F_{C2} \tag{4-9}$$

where F_{C1} and F_{C2} are the conductive heat flux through the roof and floor boundary layers, respectively, T_{l1} and T_{l2} indicate temperature at the interface between roof boundary layer and main magma and between floor boundary layer and main magma, a is the thickness of the roof boundary layer, and b is the thickness of the floor boundary layer. The values for the physical parameters adopted are: $\kappa_s = \kappa_m = 8 \times 10^{-3}$ cm^{2}s^{-1}, $L_s = 300$ J g^{-1}, $c_s = c_m = c_l = 1.3$ J g^{-1}K^{-1}, $\rho_s = 2.3$ g cm^{-3} (*Huppert and Sparks,* 1988). Other parameters including L_m, L_l, and ρ_m are obtained from thermodynamic calculation. The heat conduction equations for the roof and floor boundary layers are solved by the Crank-Nicolson finite difference method after the Landau transformation.

The dimensional heat flux from a convecting liquid has been commonly expressed as

$$F_T = (2^{4/3}\lambda)\rho_l c_l \kappa_l \left(\frac{\alpha g}{\kappa_l \nu}\right)^{\frac{1}{3}} (T_l - T_i)^{\frac{4}{3}} \tag{4-10}$$

where g is the acceleration due to gravity, α is the coefficient of thermal expansion, ν is the kinematic viscosity, and λ is a constant (e.g., *Turner*, 1979; *Kerr et al.*, 1990a). The constant λ for the actual magma as a function of composition and temperature is, however, not clear. Furthermore the specification of the interface temperature T_i is difficult, though it is very sensitive to the magnitude of the convective heat flux. *Kerr et al.* (1990a) and *Hort et al.* (1999) assumed the crystallinity at the solidification front to be zero ("mush" model). This is valid for aqueous solutions used in analogue experiments, because crystals form an interconnected network attached to the roof boundary. This assumption is, however, not appropriate for natural magmas. In the region with low crystallinity within the mush zone, crystals are suspended in a liquid and are able to move freely with little hindrance (*Marsh*, 1996), thus this region may be involved in bulk convective motions ("slurry" model). The range of the crystallinity in the region which can take part in the convective current is controlled by the viscosity variation within the mush zone (e.g., *Davaille and Jaupart*, 1993a; 1993b), but the limit of the crystallinity might be dependent on the magmatic compositions. From these reasons, the magnitude of the convective heat flux is treated as a variable in this study.

As observed in Palisades Sill (*Shirley*, 1987), the relative rate of growth of the floor and roof boundary layers remains mostly constant throughout the solidification of magma bodies. This suggests that the right hand side of the equation (4-8) is approximately proportional to that of the equation (4-9), i.e., $F_{C1} - F_T \propto F_{C2}$ throughout the solidification. If the magnitude of F_{C1} is assumed to be equivalent to that of F_{C2}, the convective heat flux might be proportional to the conductive heat flux, i.e., $F_T \propto F_{C1}$. Therefore, the convective heat flux into the roof boundary layer is parameterized to be

$$F_T = \chi \cdot F_{C1} \tag{4-11}$$

The conductive cooling corresponds to $\chi \approx 0$. If χ is larger than 1, da/dt in the left hand side of the equation (4-8) becomes negative and thus the roof wall of the magma chamber would melt. Evidence for such extensive crustal melting is, however, not observed in the Kutsugata lava. The range of the value χ is assumed to be between 0 and 1 in this study.

Boundary layer fractionation is modeled such that the interstitial melt of the floor mush zone in which crystallinity falls within the range between ϕ_1 and ϕ_2 ($\phi_1 < \phi_2$) is extracted with a volume fraction of V_{ex} (relative to the total volume of interstitial melt at each point) per 10 years and mixes with the main magma ($\phi < \phi_1$) (Fig. 4-10). The differentiated melt is assumed not to exchange heat during transportation through the mush zone, and all the heat is transported to the main magma. Crystals occurred in the convective main magma are assumed to be suspended and are not settled on the floor. This assumption may be valid when the crystallinity is not high, considering the presence of phenocryst-bearing magmas. The initial input parameters for the modified model are, therefore, chamber thickness (D), the pressure at the depth of the magma chamber (P), magma composition (C_{m0}), temperature of the magma (T_{m0}), temperature of the crust (T_{e0}), the values of ϕ_1 and ϕ_2, the value of V_{ex}, and the value of χ.

4-5-2. Compositional evolution

It is again assumed that a layer of homogeneous parental magma of the North lava (Table 2-6) is emplaced into the crust at 2 kbar. The calculated composition trends of the main convecting magma are shown in Fig. 4-11 for $\phi_1 = 0.1$, $\phi_2 = 0.5$, $V_{ex} = 0.05$, and for various χ. The composition evolution is independent of the value of χ. This is because the composition of the differentiated melt from the mush zone is controlled only by the values of ϕ_1 and ϕ_2. Furthermore the thermal and compositional structure of the floor mush zone is not much affected by the thermal convection of the overlying main magma.

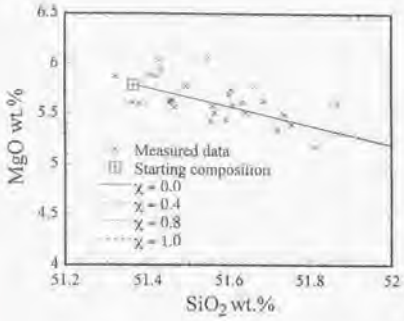

Figure 4-11. Calculated MgO-SiO_2 composition trends for various χ, at a given chamber thickness of 1000 m, ϕ_1=0.1, ϕ_2=0.5, and V_{ex}=0.05. The measured data for the North lava is also shown for comparison.

The evolution of the roof and floor boundary layers is displayed for various χ in Fig. 4-12. In the case of conductive cooling ($\chi = 0$), the growth of the roof and floor boundary layer is symmetrical. The evolution of the roof boundary layer tends to be suppressed as the convective vigor increases. The thickness of the roof boundary layer is generally less than that of the floor boundary layer in igneous intrusions as observed in Skaergaard intrusion and Palisades Sill (*McBirney*, 1995; *Shirley*, 1987), which has been considered to result partly from the convective heat flux through the roof crust. The roof boundary layer is typically 6~7 times as thick as the floor boundary layer (*Jaupart and Tait*, 1995). If this feature is caused only by the thermal convection, the value of χ is about 0.8~0.9. In actual magma reservoirs, however, blocks and aggregates of crystals from the roof mush zone could accumulate on the floor (*Marsh*, 1988). The light fractionated melt from the floor boundary layer may collect under the roof boundary layer and the liquidus temperature of crystal phases is depressed, which also suppress the evolution of the roof boundary layer. In addition, hydrothermal circulation could cool the roof of magma bodies more effectively than the floor. The value of χ is, therefore, considered to be smaller than 0.8~0.9.

Figure 4-13 shows the evolution of the composition, temperature, and crystallinity of the convecting main magma as a function of time. The variation of the value χ again does not affect the compositional evolution (Fig. 4-13a). The compositional evolution is controlled only by the value of V_{ex}, i.e., the volume flux of the fractionated melt from the floor mush zone at the given chamber thickness. As is easily expected, the temperature of the main magma decreases more abruptly as the convective vigor increases (Fig. 4-13b). The decrease of temperature of the main magma in the case of conductive cooling results from the mixing of the low-temperature fractionated melt with the main magma.

At a given time, the composition of the main magma does not vary with the value of χ, in contrast to the variation of the temperature with χ. This results in the features of the Fig. 4-13c that the main magma tends to have higher crystallinity with an increase of the value χ at the given time. The mixing of the fractionated melt from the mush zone suppresses the liquidus temperature in the main magma, but this is overcome by the effect of the temperature decrease of the main magma caused by both the heat loss through the surrounding crust and the mixing of the low-temperature fractionated melt. If the magma cools purely by heat conduction, the main magma remains to be aphyric during the wide range of compositional evolution.

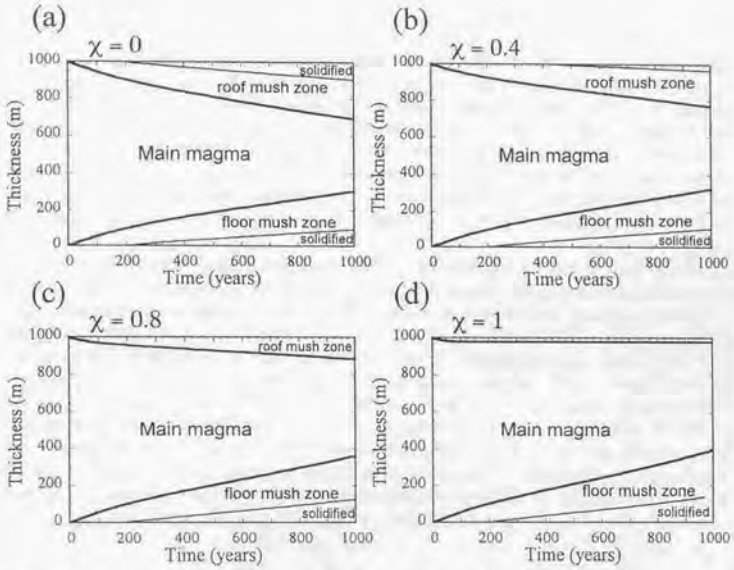

Figure 4-12. The evolution of the roof and floor boundary layers for $\chi = 0$, 0.4, 0.8, and 1.

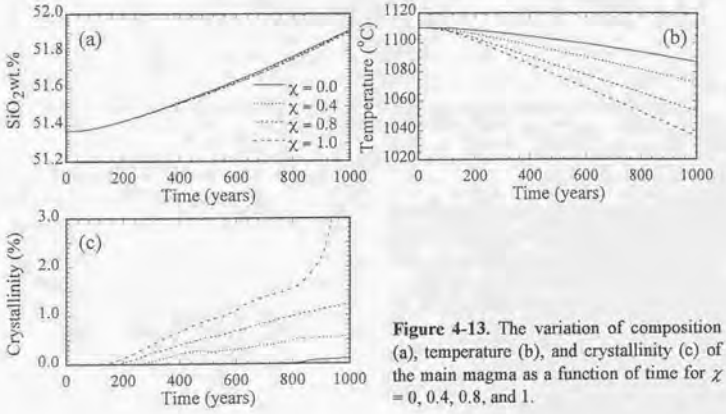

Figure 4-13. The variation of composition (a), temperature (b), and crystallinity (c) of the main magma as a function of time for χ = 0, 0.4, 0.8, and 1.

4-5-3. Thermal convection in the Kutsugata magma chamber

The role of the thermal convection on the cooling of the Kutsugata magma chamber is examined. Figure 4-14 shows the calculated temperature evolution of the main magma as a function of its SiO_2 content for various chamber thickness, 500, 1000, and 2000 m. The composition trend with > 52.0 wt.% in SiO_2 is not calculated, on the basis that fractionation of hornblende, in addition to olivine, plagioclase, and augite, is suggested during differentiation of the South-lava magma. The temperature of the main magma decreases more abruptly with an increase of χ, but the degree of the temperature decrease tends to be low as the thickness of the magma body increases. The temperature evolution of the conductive cooling model is similar in any chamber thickness. This is because both the temperature decrease and the compositional evolution of the main magma are caused only by the mixing of the fractionated melt transported from the floor mush zone.

In the figure, estimated temperature of the magmas with the composition of the sample Fm-17 (1110 °C) and Ta-26 (1100 °C) is also plotted. The error of the temperature estimation by thermodynamic calculations is commonly <10 °C, which is obtained from the comparison of the data from crystallization experiments (e.g., *Grove and Bryan*, 1983; *Kinzlar and Grove*, 1992) and calculated temperatures. If the value of χ is large, the modeled trend can never satisfy the observed temperature of the sample Ta-26 in any chamber thickness. The conductive cooling model ($\chi = 0$) explains the best the estimated temperature of the Ta-26 magma. Figure 4-15 also displays the results of the calculation for various V_{ex} at the given chamber thickness of 1000 m. The compositional evolution by the conductive cooling model is again close to the temperature of the Ta-26 magma, independent of the variation of the parameter V_{ex}. The main part of the magma body was suggested to have been aphyric throughout the evolution of the North-lava magma (Table 2-4), which also supports the low value of χ (Fig. 4-13c).

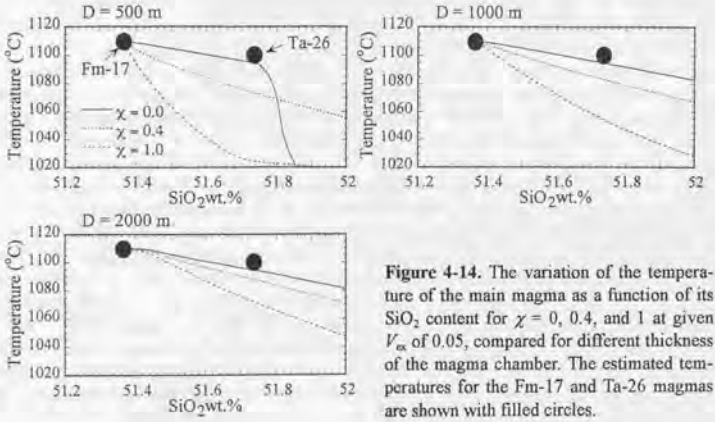

Figure 4-14. The variation of the temperature of the main magma as a function of its SiO_2 content for χ = 0, 0.4, and 1 at given V_{ex} of 0.05, compared for different thickness of the magma chamber. The estimated temperatures for the Fm-17 and Ta-26 magmas are shown with filled circles.

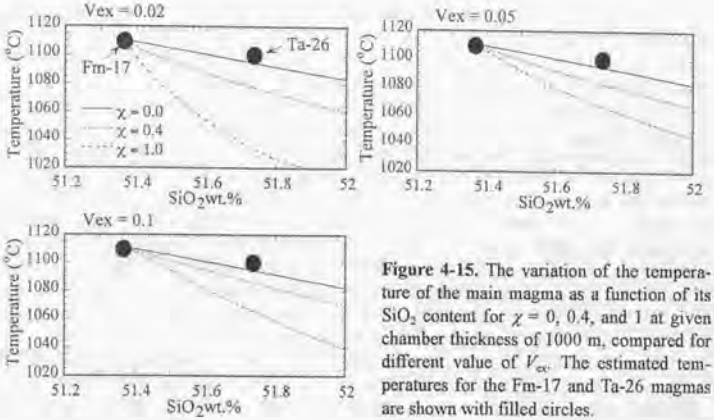

Figure 4-15. The variation of the temperature of the main magma as a function of its SiO_2 content for χ = 0, 0.4, and 1 at given chamber thickness of 1000 m, compared for different value of V_{ex}. The estimated temperatures for the Fm-17 and Ta-26 magmas are shown with filled circles.

The estimated temperature of 1100 °C for the Ta-26 magma is slightly above the calculated temperature of $\chi = 0$ in all diagrams. This may be derived from the assumption that the fractionated melt is extracted to the main magma without exchanging heat within the mush zone during transportation. In actual process, the low-temperature fractionated melt is likely to have been heated during transportation through the higher temperature portion within the mush zone, and the decrease of the temperature of the main magma by mixing of the fractionated melt might be suppressed.

The result of the modeling suggests that the cooling of the Kutsugata magma was dominated principally by heat conduction. On the other hand, the observation that the floor sequence of igneous intrusions is commonly 6~7 times thicker than the roof sequence (*Jaupart and Tait*, 1995) suggests significant convective cooling during their solidification, though it may have been partly derived from the other mechanisms as described above. Apart from the difference in magmatic composition, the most principal difference between these two cases is the depth of the magma body. The igneous intrusions, now exposed to the Earth's surface, were commonly injected to the crust at the shallow level (~500 bars), whereas the pressure at the depth of the Kutsugata magma chamber is about 2 kbar. The difference of the convective vigor might have resulted from the difference in temperature of the surrounding wall rocks. The heat release from the cooling magma is controlled by the heat transfer within the crust. The lower-temperature crust could enhance the cooling of the magma body more efficiently than the higher-temperature crust, if the magmatic temperature is similar. Efficient heat release through the crust could have been balanced by convective heat flux from the convecting main magma in the case of the igneous bodies intruded in the crust at the shallow level.

The physical properties of the Kutsugata magma favor thermal convection compared with the other magmas such as MORB, judging from the following two points; (1) fairly low magmatic viscosity and (2) large temperature difference between the main magma and the mush zone at the interface with the main magma (solidification front). The point (1) is suggested from the magmatic composition. The Kutsugata lava is high Na/K alkali basalt and the content of the dissolved water is estimated to have exceeded 4 wt.%. The pahoehoe lava morphology of the erupted Kutsugata magma also supports that the viscosity of the magma was quite low. The point (2) would be important as a driving force for thermal convection in magma chambers. Unlike

aqueous solutions, convective current in magmatic systems can involve a part of the roof mush zone, because crystals are suspended in the region with low crystallinity. At the low-crystallinity region within the mush zone of the Kutsugata magma chamber, olivine was the sole crystallizing phase during a significantly large cooling interval (1100~1050 °C) (Fig. 4-16a). In the case of MORB for example, on the other hand, plagioclase appears as a crystallization phase at much lower temperature interval from the temperature of the main magma than that of the Kutsugata magma (Fig. 4-16b), because of lowe water content. The liquidus volume change of plagioclase with decreasing temperature is much larger than that of olivine, and thus appearance of plagioclase results in abrupt increase of crystallinity with a decrease of magmatic temperature. Given that crystals in the mush zone with <10 % crystallinity are completely suspended in magmas, the region which spans the temperature interval of up to 90 °C could take part in the convective current in the Kutsugata magma (Fig. 4-16a). In the MORB, however, the region with temperature interval of only 35 °C can be involved in the convective motion (Fig. 4-16b). The magnitude of the Rayleigh number and the convective heat flux are determined by the temperature difference between the main magma and the solidification front, i.e., $T_l - T_i$ (see equation (7)). Therefore, the Kutsugata magma would have a high potential for vigorous convection compared with the MORB. This may hold true for the other magmas with lower water content than the Kutsugata magma. The result of this study, that the thermal convection was not dominant in the cooling of the Kutsugata magma chamber, might suggest that the thermal convection in a crustal magma chamber is essentially weak at the relatively deep level.

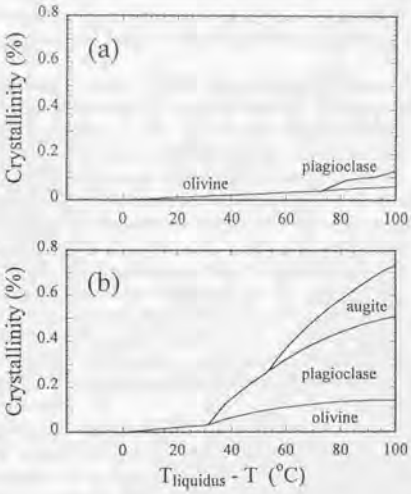

Figure 4-16. Calculated phase diagram for the sample Fm-17 of the Kutsugata lava (a) and the representative MORB (ALV-528 of *Grove and Bryan*, 1983) (b) at 2 kbar. The horizontal axis indicates the difference of the temperature from the liquidus (1110 °C for (a) and 1245 °C for (b)). These diagrams are shown in order to compare the variations of the crystallinity of the mush zone near the solidification front.

5. Discussion

How a hot magma differentiates during residence in a magma chamber by heat release through the cool surrounding crust is a major objective target of petrology. This problem potentially involves many processes, some of which are deeply coupled. Cooling of the magma results in a crystallization. A separation of the crystals from melt, caused by density difference between them, changes the magma composition because the crystals have different chemical compositions from the melt. The compositional evolution of the magma is controlled by the region where the crystal-melt separation takes place in a temperature gradient of the magma. The cooling from the surrounding crust produces the region which spans the interval between the solidus and the liquidus of the magma, i.e., mushy boundary layer, along the walls of the magma chamber. Thus the crystal-melt separation can primarily occur there (boundary layer fractionation). The boundary layer fractionation results in the separation of lower-temperature phases than the liquidus of the main magma. Thermal convection in the magma chamber could play important role on the compositional evolution of magmas, as well as thermal evolution, because it keeps the composition and temperature of the main magma homogeneous, and the magma can fractionates crystals which formed at the liquidus of the main magma (homogeneous fractionation). The temperature of the surrounding crust can exceed its solidus by heat release from the hot magma, and it melts partially. If the partial melt segregates from the crust and assimilates through the solidifying boundary layer of the magma chamber, the chemical composition of the main magma is modified. In addition to these processes, perturbations are caused in the magma chamber by replenishment and eruption of magmas.

The differentiation scheme of magmas in magma bodies depends on the presence or absence of phenocrysts upon intrusions. These phenocrysts can separate from the magma soon after the intrusion, and thus the chemical composition of the bulk magma changes instantly (punctuated fractionation; *Marsh*, 1996). On the other hand there might not have been still a general framework on the compositional evolution of magmas which are initially free from phenocrysts (including differentiation after the punctuated fractionation). Many petrological models from observations on erupted materials assume a homogeneous temperature throughout the cooling magma chambers. Phenocrysts are believed to represent those crystallized from the liquidus of the magma, and the composition of the magma always evolves by fractionation of the liquidus phases, that is, homogeneous fractionation. With few exceptions, geochemical models to calculate liquid lines of descent of magmas also assume homogeneous fractionation (e.g., *Nielsen*, 1988; *Ghiorso and Sack*, 1995). The assumption of homogeneous temperature is valid when the whole magma convects vigorously (e.g., *Huppert and Sparks*, 1988; *Worster et al.*, 1990). Mechanism of homogeneous fractionation in convecting magmas has been investigated in details (*Marsh and Maxey*, 1985; *Martin and Nokes*, 1989).

Crystallization along the marginal part of magma bodies and its relevance to the magmatic differentiation (boundary layer fractionation) was suggested from observations on igneous intrusions (*Campbell*, 1978; *McBirney and Noyes*, 1979) and volcanic rocks (*de Silva*, 1989; *Tait*, 1988), and from fluid dynamical investigations (*Turner*, 1980; *McBirney et al.*, 1985). The importance of this fractionation mechanism was shown by *Langmuir* (1989) and *Nielsen and Delong* (1992) by geochemical modeling, which predict that the compositional evolution of magmas by boundary layer fractionation could be fairly different from that by homogeneous fractionation. *Marsh* (1996) demonstrated, on the contrary, that the initially phenocryst-free magmas would not differentiate even when the magma is cooled from the surrounding wall rocks. He raised an example of the observation on Peneplain Sill, Antarctica (400 m thick), which exhibits fairly ho-

mogeneous compositions in major and trace elements throughout the sill except for silicic segregations present below the roof crust.

The absence of general framework on magmatic differentiation in cooling magma bodies is considered to have come partly from the following reasons. The igneous intrusions commonly show evidence for internal differentiation, as seen from the spatial variation of chemical composition throughout the bodies. However, the chemical composition in the intrusions can never constrain the mechanism of crystal fractionation, because the spatial variation of the chemical composition integrated all the processes during solidification, and the *in situ* information on the crystal-melt separation in early stages of the solidification is not recorded. On the other hand, most of the investigations on volcanic rocks have ignored the temperature gradient in magma chambers. Phenocrysts are assumed to represent the fractionated crystals. For example, a hypothesis of closed-system crystal fractionation is commonly tested by utilizing chemical compositions of observed phenocrysts and whole-rock composition trend.

This study investigated erupted materials by detailed petrological approach, and documented the boundary layer crystallization in a magma chamber. The mechanism of crystal fractionation through development of the mushy boundary layer is clarified on the basis of the whole-rock composition trend and origin of the crystals which specified by careful examination of their chemical zonings. These enable to elucidate the thermal and compositional evolution of cooling magma chamber from basaltic to dacitic composition. A new magma differentiation model including boundary layer fractionation and heat transportation was also developed.

It is shown below that the concept of boundary layer fractionation may generalize the magmatic evolution in crustal magma chambers. The study of the magma-chamber processes is also important as a tool to extract precise physicochemical information of the Earth's mantle, as described in the introductory chapter. This view is also summarized below. Finally, the problem of magmatic evolution which needs to be investigated further is described.

5-1. Compositional Evolution in Magma Chambers

This paper shows that boundary layer fractionation played a dominant role on the differentiation of both the basaltic and andesitic magmas from Rishiri Volcano. The boundary layer fractionation may be a principal mechanism in magmatic differentiation, because a magma is cooled from the surrounding crust by heat conduction and crystallization primarily occurs along the chamber walls. This is, however, against the observation on the Peneplain Sill which exhibits no remarkable differentiation (*Marsh*, 1996). Here, I propose that the critical factor for determining whether the magmatic differentiation occurs or not is the efficiency of the melt extraction from the mushy boundary layer (V_{ex} in the model; Fig. 4-1) and the range of crystallinity within the mush zone from which the melt is extracted (ϕ_1 and ϕ_2 in Fig. 4-1).

In the boundary layer fractionation, the interstitial melt can be extracted from the mush zone by the two mechanisms; compositional convection and compaction. The compositional convection is controlled by permeability, density difference between the main magma and the interstitial melt, melt viscosity, and porosity, whereas the compaction is by density difference between the crystals and interstitial melt, permeability, and viscosity of the melt and crystals. In the following discussion, efficiency of boundary layer fractionation is compared between hydrous alkali basalt represented by the Kutsugata magma (sample Fm-57) and anhydrous tholeiitic basalt represented by MORB (ALV-528 of *Grove and Bryan*, 1983).

Figure 5-1 compares the density of crystals and interstitial melt within the mush zone as a function of temperature difference from the liquidus, for the Kutsugata magma and the MORB. The variation of crystallinity with the temperature is also shown (see also Fig. 4-16). The

similar figure as a function of crystallinity within the mush zone is also shown in Fig. 5-2. The density of the interstitial melt and coexisting crystals in the mush zone at which crystallinity is 30 vol.% is shown in Table 5-1. Melt density in the Kutsugata magma decreases with increasing crystallinity in the mush zone, whereas it increases in the MORB. With decreasing temperature, the average density of crystals initially increases, and then it decreases abruptly in both magmas. This reflects that crystallization phase is only olivine at relatively high magmatic temperature, and then appearance of plagioclase depresses the average density of crystals. The increase of the density of olivine at high temperature results from the decrease of the Mg#. Note that the temperature decreases by only ~60 °C during 30 % crystallization in the MORB, whereas it decreases by up to 140 °C in the Kutsugata magma (Fig. 5-2).

Compositional convection never occurs in the MORB, because the density of the main magma is lower than that of the interstitial melt of the mush zone (Fig. 5-1). On the contrary, the compositional convection is possible to occur in the Kutsugata magma. The density difference between the crystals and melt is much larger in the Kutsugata magma than in the MORB (Fig. 5-2), suggesting that the compaction can occur efficiently in the mush zone of the Kutsugata magma, compared with the MORB.

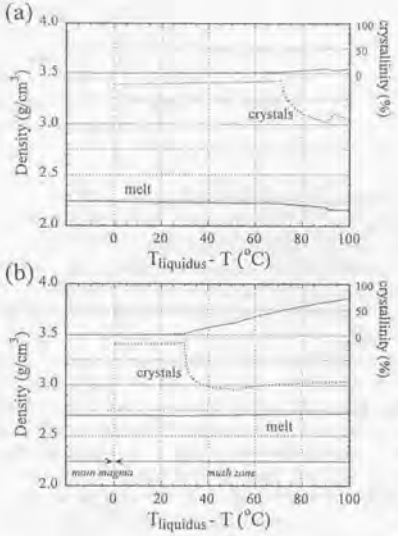

Figure 5-1. Variation of density of crystals and interstitial melt within the mush zone as a function of the temperature difference from the liquidus of the main magma, for (a) the Kutsugata magma (Fm-57) and (b) the MORB (ALV-528 of *Grove and Bryan*, 1983). Variation of the crystallinity is also shown. See Figure 4-16 for the phase relations.

Table 5-1. Comparison of Estimated Density of Melt and Coexisting Crystals between Kutsugata Magma and MORB

	Interstitial melt	Crystals		
Density, g cm-3		olivine	plagioclase	augite
Kutsugata Magma	2.16	3.48	2.72	-
MORB	2.73	3.47	2.73	3.33

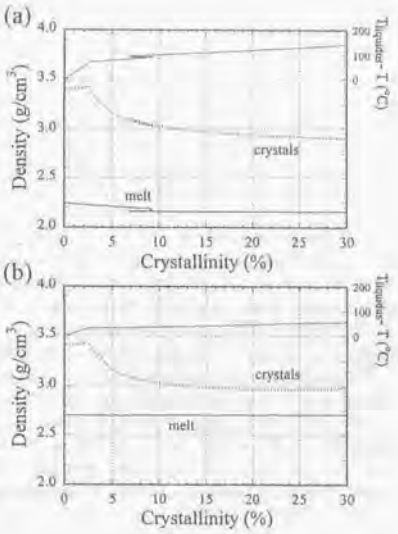

Figure 5-2. Variation of density of crystals and interstitial melt within the mush zone as a function of the crystallinity, for (a) the Kutsugata magma (Fm-57) and (b) the MORB (ALV-528 of *Grove and Bryan*, 1983). Variation of the temperature is also shown.

These results demonstrate that extraction of the interstitial melt from the mush zone is much more effectively occur in the Kutsugata magma than the MORB. Therefore the parameter V_{ex} is significantly high in the Kutsugata magma, relative to the MORB. The composition trend of the North lava in the Kutsugata lava is explained by the extraction of the interstitial melt from the floor mush zone in which crystallinity ranges from 10~50 vol.% ($\phi_1 = 0.1$, $\phi_2 = 0.5$). In the MORB, these crystallinities could be much lower than the Kutsugata magma, because the density contrast between the crystals and melt is significantly smaller than that of the Kutsugata lava. Although qualitative, the ϕ_2 may be lower than 0.1, judging from the density difference (Fig. 5-2). The composition of the fractionated melt which is originated from relatively low-crystallinity region of the mush zone (low ϕ_1 and ϕ_2) is much closer to the composition of the main magma than that of the melt extracted from the deep mush zone. The mixing of the fractionated melt from the low ϕ_1 and ϕ_2 region does not promote differentiation of the main magma so effective as the mixing of the melt from the high ϕ_1 and ϕ_2 region. In sum, the boundary layer fractionation occurs much more effectively in hydrous alkali basalt than anhydrous tholeiitic basalt. The viscosity of the alkali basalt is suggested to be much lower than that of the tholeiite because of alkali and water-rich composition, which further enhances the difference of the efficiency of the melt extraction between the two magmas.

The efficiency of the boundary layer fractionation in basaltic magma chambers is strongly controlled by the water content of magmas. Density of the melt decreases with increasing water content, which results in larger density contrast between the crystals and interstitial melt. Furthermore high water content of magmas significantly reduces the liquidus volume change at the given temperature interval. For example, the magma crystallizes with more than 70 % during cooling interval of 100 °C in the MORB (Fig. 4-16b), whereas the Kutsugata magma crystallizes with only 15 %. This suggests that the proportion of the mush zone ($0 < \phi < 1$) relative to the total thickness of the boundary layer is higher in the hydrous magma chamber at the

given thermal gradient in the boundary layer. Thus the proportion of the mush zone relative to the main magma is also high in the hydrous magma at the given chamber thickness, though the boundary layer of the anhydrous magma chamber might be somewhat thicker because of the large temperature difference between the main magma and the surrounding crust due to the high magmatic (liquidus) temperature.

These lines of suggestions explain well the absence of the internal differentiation of the Peneplain Sill. The magmatic composition of the sill is quartz tholeiite (Marsh, 1996). The water content of the Peneplain magma is considered to be much lower than that of the alkaline magma. The magmatic viscosity is also significantly higher. This might have resulted in ineffective crystal-melt separation within the growing mush zone, i.e., low values of the parameters V_{ex}, ϕ_1, and ϕ_2.

The internal cooling of the magma body is governed by the heat loss through the surrounding crust and the mixing of the low-temperature interstitial melt from the mush zone. At the same time the liquidus temperature of crystal phases in the main magma is suppressed by the mixing of the fractionated melt. Therefore the crystallinity of the main magma is determined by the balance between the temperature decrease and the depression of liquidus temperature. In the case of the Kutsugata magma system, the effect of the liquidus depression exceeds the temperature decrease of the main magma, which resulted in aphyric nature during the differentiation from basaltic to dacitic compositions. In the case of the other magmatic compositions such as MORB, however, the degree of the liquidus depression could be significantly suppressed. This is because the volume flux of the fractionated melt from the mush zone is not high (low V_{ex}). Furthermore the interstitial melt could not be extracted from the deep mush zone (high ϕ_1 and ϕ_2), and therefore the melt is not enriched in incompatible elements for promoting liquidus depression, as represented by H_2O. On the basis of these considerations, alkaline magmas are likely to remain aphyric during their evolutions because of the effective boundary layer fractionation, whereas low-H_2O magmas such as tholeiitic basalt tend to become porphyritic in the early stage of the evolution in cooling magma bodies. As discussed in the Section 4-5, however, the variation of the crystallinity with time does also depend on the magnitude of the thermal convection.

The efficiency of the extraction of the interstitial melt from the mush zone is dependent on the density relations among the crystals, interstitial melt, and main magma, and the viscosity variation within the mush zone. The parameters V_{ex}, ϕ_1, and ϕ_2 as a function of magmatic compositions might be calculated on the basis of the theoretical analyses, which is an important future work.

From these, alkali basalt differentiates easily in magma chambers. The interstitial melt from the mush zone is much more differentiated than the main magma. This promotes compositional evolution of the main magma and keeps the main magma aphyric. Phenocrysts may be rather produced during magma ascent, as discussed in the Chapter 2. In the tholeiitic basalt, on the other hand, the boundary layer fractionation is not effective. Fractionated crystals are close to the liquidus phase of the main magma. Because of the low degree of liquidus depression resulting from the boundary layer fractionation, crystals occur in the main magma in the early stage of the magmatic evolution. Low dissolved water results in the appearance of plagioclase at relatively high magmatic temperature, which promotes to become porphyritic nature of the main magma. Even in the main magma, the crystal-melt separation may not occur efficiently because of the small density contrast between the crystals and melt. Fractionation of high-density mafic mineral phases is suppressed if they form crystal clots with low-density plagioclase. Thus the tholeiitic basalt is less likely to evolve. In the case that the interstitial melt becomes denser than the coexisting crystals, the situation is slightly different, because the release of the interstitial melt can effectively occur in the roof mush zone.

One of the most important, but the most inaccessible parameters for long-term prediction of volcanic eruptions is the thickness of magma chambers. The size of the magma body is equivalent to the size of the heat source beneath the volcanoes. It is show below that the thick-

ness of the magma body can be predicted on the basis of the boundary layer fractionation model, if the magma chamber is sill-like body. If one investigates volcanic materials which erupted intermittently from the same magma reservoir, temperature of the main magma and depth of the magma chamber can be estimated from the petrological approach. The parameters ϕ_1 and ϕ_2 may also be obtained by utilizing composition trends of whole rocks. If the value of the V_{ex} is calculated by theoretical analysis, the remaining unknown parameters for controlling magmatic evolution is the time scale of magmatic evolution, thickness of the magma chamber, and convective heat flux. The magnitude of the thermal convection might be evaluated on the basis of the estimated magmatic temperatures and magmatic compositions, as done in the present study. Given that the parameter V_{ex} and the magnitude of the thermal convection are estimated, the thickness of the magma chamber is a function of the time scale of the differentiation. If the time scale is obtained by the historical records or precise dating of erupted materials, the size of the magma body can be estimated.

5-2. Modification of Primary Magma Composition

Primary magmas generated in the Earth's mantle exchange heat and materials during ascent to the surface. Crustal magma chamber is one of the most principal sites for modification of the primary magma composition, because the magma could reside there over relatively long periods of time. For example, the composition of the primary magma is easily lost by magma mixing if the primary magma emplaces to a magma chamber occupied by a felsic magma. Evidence for such magma mixing is frequently observed from erupted materials. Apart from the mixing with exotic magmas, the original magmatic composition could be modified in the magma reservoir by the following mechanisms; (1) fractionation of crystals which are initially contained by the magma upon intrusion (punctuated fractionation), (2) fractionation of crystals formed by heat loss through the surrounding crust during residence in the magma reservoir (boundary layer and homogeneous fractionations), and (3) assimilation of crustal materials during residence in the magma chamber.

5-2-1. Punctuated fractionation

During ascent of the primary magma to the crustal magma reservoir, crystals may occur by thermal interaction with the low-temperature wall rocks. Such crystals are considered to settle on the floor of the magma reservoir soon after the injection (*Marsh*, 1996). The effectiveness of this differentiation is controlled by the size of the crystals and density difference between the crystals and melt, because the removal of the crystals from the magma is determined by a balance between capture of the crystals by the downward-growing roof crust and settling velocity of the crystals.

The driving force for crystallization during magma ascent from the mantle deserves to consider. The magmatic temperature decreases by decompression of the magma due to thermal expansion. Liquidus temperature of crystal phases also decreases progressively during magma ascent until the magma is saturated with water at the shallow level (commonly <1 kbar). The effect of the decrease in magmatic temperature and liquidus temperature is evaluated for the experimentally-produced partial melt of peridotite of *Hirose and Kushiro* (1993) (Table 4-1). If the magma ascends adiabatically, the magmatic temperature decreases by about 2.5 °C/kbar (after *Lange and Carmichael*, 1990). On the other hand, liquidus temperature of olivine decreases by about 6 °C/kbar. This indicates that the magma cannot be crystallized, if the heat loss from the magma is negligible. The crystallization during magma ascent, therefore, requires significant heat

loss through the surrounding wall rocks. The cooling of the magma might occur easily because the magma is superheated and thus the latent heat of crystallization is absent. The geothermal gradient has been believed to be about 3~5 °C/kbar (*Philpotts*, 1990) and is larger than the adiabatic temperature decrease of 2.5 °C/kbar, thus driving force for the crystallization tends to increase slightly during ascent.

5-2-2. Crystal fractionation during residence in magma chambers

When hot basaltic magmas are emplaced into the crust and they contact cold solid rocks, a chilled margin forms because the heat flux from the magma cannot balance the very large initial conductive heat flux in the rock (e.g., *Huppert and Sparks*, 1989). However, the conductive heat flux through the crust decreases with time and the mushy boundary layer is produced along the chamber walls. Even when the main magma is in primitive composition, the mushy boundary layer could produce the melt of differentiated composition. Thus the mixing of the fractionated melt with the main magma results in the separation of low-temperature phases from the main magma, as discussed in the previous chapters. Homogeneous fractionation from the main magma may take place simultaneously with boundary layer fractionation, if the main magma is cooled and crystallization occurs significantly. It is not easy to restore the original magmatic composition before the crystal fractionation in crustal magma chambers, because the compositional evolution of the magma would not follow the liquid line of descent which is constrained by cotectic phase boundaries. Though local thermodynamic equilibrium may be attained in the mush zone, interstitial melt transported to the main magma integrates the local melt composition under the thermal gradient of the mush zone.

5-2-3. Assimilation from the crust

The crust surrounding the magma chamber melts when the temperature exceeds the solidus of the crust. Assimilation of the partial melt of the crust significantly affects the concentration of trace elements and isotopic compositions even when the amount of the assimilated materials is negligible relative to the total volume of the magma body. Therefore, trace element contents and isotopic compositions of the original magma could be modified easily during residence in the crustal magma chamber.

Because of relatively low temperature of the crust surrounding the Kutsugata magma chamber, the temperature at the crust-magma interface is considered to have been below the solidus of the main magma (Fig. 2-24), and the completely solidified region was developed at the marginal part of the magma chamber. The crustal materials were thus assimilated to the main magma through the "solid shell" and mush zone. There might have been many cracks across the "solid shell" because of volumetric change by solidification. The crustal materials may have been transported through the crack. In addition, it may be possible to fracture the shell by hydraulic fracturing if the connected partial melt in the surrounding crust attains a height that is enough to exceed the yield strength of the shell. Once the materials reached the mush zone where the temperature was above the solidus, they were transported to the main magma by compaction and compositional convection, similar to the interstitial melt.

If magmas intrude to the crust at deeper level, the melting of the crust occurs more extensively because of high temperature as expected from the geotherm (*Huppert and Sparks*, 1988), though the solidus temperature also increases. At the deep level, furthermore, the higher temperature of the surrounding crust results in the smaller temperature difference between the magma-crust contact and the solidus of the magma, which reduces the thickness of the "solid shell" at the marginal part of the magma body. The contact temperature could also exceed the solidus of the magma. In this case the mush zone is directly in contact with the crust. The partial

melt of the surrounding crust might be easily assimilated through the solidifying boundary layer of the cooling magma at the deep level, compared with the magma bodies at the shallow level. Thus the degree of assimilation of the crustal materials could be strongly dependent on the depth of the magma chamber.

5-3. Future Works

Further revision of the boundary layer fractionation model developed by this study enables to establish general framework of magmatic evolution in the crust. In terms of the crystal fractionation in magma chambers, the model is necessary to consider the homogeneous fractionation. If the thermal convection is vigorous in the main magma, the assumption of homogeneous magmatic composition and temperature is valid. If the convection is present but not so vigorous, however, the assumption is not appropriate. Incorporation of the crystal fractionation from the main magma needs further consideration. The model can calculate the crystallinity at a given magmatic temperature and composition, but the size and nucleation density of crystals is impossible to obtain though this is important for the crystal-melt separation. These may be expressed as a function of a cooling rate at the individual sites of the crystallization, as a gross approximation. As described above, the parameters V_{ex}, ϕ_1, and ϕ_2 need to be calculated as a function of magmatic composition and temperature, independently from the theoretical analyses, probably with two-dimensional model. The present model assumes the V_{ex} to be constant, but this parameter could be expressed as a function of the crystallinity in the mush zone at the individual calculation steps.

Towards the general understandings of the crust-magma system, thermodynamic modeling of the crust surrounding the magma chamber is necessary. This enables to calculate the degree of partial melting at a given local temperature and composition of the crust. On the basis of the modeling of the crust, segregation of the partial melt and its assimilation through the solidifying magma chamber must be examined.

Simultaneously with the theoretical modeling, further information of magmatic evolution needs to be obtained from natural observation, for magmas with various chemical compositions, for those from various tectonic settings, and for those derived from various depths of magma chambers. From the Kutsugata and Tanetomi lavas, several important factors which control the magmatic evolution are identified. These factors could vary with magmas. The variation of the factors estimated from the observations must always constrain the theoretical model.

The general understandings of magmatic evolution are necessary in order to use volcanic rocks as a tool to extract information of the deep level of the Earth. As done by the present study, modification of magmatic composition by crystal fractionation in the magma chamber can be evaluated by detailed petrological approach, mainly constrained from major element and compatible trace element, and modification by crustal assimilation is evaluated by the information of the variation of isotopic composition and incompatible trace element. This study used the Li/Y ratio for discriminating the "punctuated fractionation" and boundary layer fractionation, on the basis that the Li might not be derived from the subducting slab. Similar tools for discriminating the individual processes involved in the magmatic evolution from magma generation to the eruption must be found for the extraction of the more precise information of the deep source mantle.

6. Conclusions

(1) Boundary layer crystallization in a basaltic magma chamber is documented from an erupted magma. Extremely An-rich plagioclase, which was not derived from exotic magma or the surrounding crust, is too An-rich to have crystallized from liquids on the main liquid line of descent. The plagioclase with An-rich composition formed in the mushy boundary layer of the magma chamber where the low-temperature and high water content were achieved by transportation of H_2O-rich fluid from the solidifying margin.

(2) Boundary layer fractionation is documented for the magma chamber of both the basaltic and andesitic compositions. Estimated chemical compositions of fractionated minerals during differentiation of the Kutsugata and Tanetomi magmas coincide with the observed compositions of the crystals derived from the mushy boundary layer. The low-density interstitial melt was extracted from the floor mush zone by such mechanisms as compositional convection and compaction. The fractionated melt was mixed with the overlying main magma, causing differentiation of the Kutsugata and Tanetomi magmas.

(3) Tanetomi magma is shown to have been a derivative magma of the Kutsugata magma. Both the Kutsugata and Tanetomi lavas erupted from the western flank of the Rishiri Volcano at the same stage of volcanic activity. The estimated pressure at the depth of the magma chamber is about 2 kbar for both lavas. Concentration patterns of incompatible trace elements also support that the Kutsugata magma could have been the parental magma of the Tanetomi magma. Magmatic temperature decreased progressively from 1110 °C to 920 °C during the evolution from basaltic to dacitic compositions. Boundary layer fractionation kept the main magma to be aphyric during the wide range of compositional evolution.

(4) Assimilation of the crustal material into the magma chamber took place simultaneously with the boundary layer fractionation during evolution of the Kutsugata magma system. The material might be a partial melt of granitic rocks, wherein a significant amount of H_2O-rich fluid was dissolved. The assimilation produced the marked variation of Sr and Pb isotopic compositions throughout the evolution from basaltic to dacitic compositions, though the amount of the crustal materials assimilated to the magma was negligible.

(5) Significant amounts of large phenocrysts up to 5 mm is shown to have crystallized during magma ascent. The Kutsugata magma is inferred to have been rich in dissolved H_2O (>4 wt.%) in the magma chamber, and liquidus temperatures of phenocryst phases were significantly suppressed. Large undercooling caused by decompression and degassing of the magma was the driving force for significant crystallization during ascent because of the increase in liquidus temperature due to vapor exsolution. Low ascent rate of the Kutsugata magma, which is suggested by pahoehoe lava morphology and no association of pyroclastics, gave sufficient time for crystallization. Furthermore, the large degree of superheating of plagioclase in the magma chamber caused plagioclase crystallization with low-population density and large-crystal size, which characterizes the porphyritic nature of the Kutsugata lava.

(6) Factors responsible for effusive eruption of the Tanetomi lava triggered by injection of a basaltic magma are quantitatively evaluated. A vapor exsolution caused by a magma mixing in a magma chamber, which has been considered to play an important role on triggering explo-

sive eruptions, was negligible in the eruption of the Tanetomi magma. The effect of the net volume increase by the replenishment is one order of magnitude greater than that of the volume increase by vapor exsolution, and this was responsible for the tapping of the magma chamber.

(7) A boundary layer fractionation model for the thermal and compositional evolution of a basaltic magma chamber is presented. The model utilizes a multicomponent thermodynamic approach for relating the compositional structure with the thermal structure of a cooling magma body. The magma composition in the main magma body evolves by transportation of a fractionated interstitial melt from the mushy boundary layer. The consideration of both the thermal and compositional evolution of the magma body enables a realistic simulation of magmatic differentiation as a function of time and space.

(8) Compositional evolution of a magma by boundary layer fractionation is controlled by the range of the crystallinity within the mush zone from which fractionated interstitial melt is extracted. The scale of the magma chamber and the volume flux of the transported interstitial melt do not affect the resulting compositional evolution of the main magma.

(9) Primary magma composition of the Kutsugata lava is estimated by utilizing the boundary layer fractionation model and the constraints from incompatible trace elements. It is also shown that the olivine maximum fractionation model, the common procedure for estimating the primary magma composition from volcanic rocks, gives an estimation which is significantly different from the true primary magma composition if the magma actually differentiated by boundary layer fractionation. This can cause significant errors in estimating the conditions at which the primary magma was generated.

(10) Thermal convection in the Kutsugata magma chamber is suggested to have been essentially weak, and the magma was cooled principally by heat conduction. This result is independent of the model parameters such as those for the boundary layer fractionation and the size of the magma chamber. The convective vigor in a crustal magma chamber might be generally weak, considering that the physical properties of the Kutsugata magma favors vigorous convection compared with the other magmas of different composition.

(11) The efficiency of the boundary layer fractionation in a basaltic magma chamber is suggested to be governed by the content of dissolved water. The boundary layer fractionation occurs effectively in hydrous magmas, which significantly promotes compositional evolution of the main magma. In anhydrous magmas, on the other hand, the boundary layer fractionation is not effective and the main magma tends to become porphyritic in the early stage of the evolution. Because of the small density contrast between crystals and melt, compositional evolution is less likely to occur than the hydrous magmas.

(12) The present study demonstrates that the detailed investigation of erupted materials with limited compositional diversity provides useful information for constraining *in situ* magmatic evolution, and integration of these differential information enables to elucidate thermal and compositional evolution of a magma chamber over long periods of time. Such information is not obtained from the study of igneous intrusions. A result is powerful constraints on modeling of igneous differentiation processes, one of the main goal of petrology.

Appendix

A. Eliminating the Effect of Post-Eruption Processes

Segregation bodies are frequently present in thick flows of the Kutsugata lava. These bodies are several mm to more than 10 cm thick, depending on the thickness of the lavas, and are rich in vesicles and opaque minerals. They are considered to be formed *in situ* during the consolidation process and have different whole-rock chemical compositions from the host basalt, thus affecting bulk composition of the host to a certain extent (*Yoshida et al.*, 1981). The effect of the segregation process on whole-rock chemical compositions must be examined, especially for thick lavas with abundant segregation bodies, to estimate the true compositional trend of the Kutsugata magma. Samples were collected from horizons where segregation bodies are rare, but these samples could be close to such a body in three dimensions.

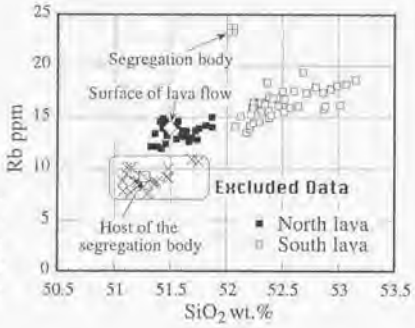

Figure A-1. SiO_2-Rb diagram for the whole-rock samples to show data excluded from this study. Data for samples from a segregation body, its host, and surface of the same lava flow unit are also shown.

Figure A-1 shows the SiO_2-Rb diagram, where compositions of samples from a segregation body, the adjacent host of the body, and the surface of the same flow unit are plotted in addition to those of all analyzed samples. The host and segregation body plot an opposite sides of the surface of the lava flows, which is considered to preserve the magmatic composition of the erupted stage. The adjacent host-rock samples with significantly lower Rb concentration are indicated by crosses and are excluded in this paper. No data are excluded in the South lava, because most samples were collected from the surface of lavas along the coast, and from the mountainside where each flow unit is thin and segregation bodies are not developed.

B. Crystal Fractionation Model

In the fractionation model considered here, chemical compositions of fractionated mineral phases, as well as their weight fraction, are estimated by utilizing composition trends of 10 major elements, Ni, and Sr. The major-element compositions of olivine and plagioclase can be expressed by Mg# and An content, respectively, ignoring trace elements such as MgO and FeO contents in plagioclase and CaO in olivine. Trace elements in augite cannot be ignored, therefore,

augite composition is expressed by the following procedure. Compositions of the representative augite core with Mg#82.5; SiO_2: 51.6 wt.%, TiO_2: 0.3 wt.%, Al_2O_3: 2.7 wt.%, FeO: 6.1 wt.%, MnO: 0.2 wt.%, MgO: 16.2 wt.%, CaO: 20.9 wt.%, and Na_2O: 0.3 wt.%, are used. Then, Mg# is varied by fixing cation ratios of elements other than Mg and Fe.

The Mg# of augite is known to be a function of that of olivine (*Kawasaki and Ito*, 1994), and it is calculated by using the Mg-Fe distribution coefficients obtained from the average Mg# of augite and olivine phenocrysts in the Kutsugata lava ($Mg\#^{aug}=0.661 \cdot Mg\#^{ol}+31.49$; Fig. 2-18). Systematic correlation between Mg# and Ni content is observed in unzoned olivine phenocrysts of the Kutsugata lava ($Ni(ppm)=110 \cdot Mg\#^{ol}-7750$; Fig. 2-15), and this relation is used for the modeling of Ni concentration. Partitioning of Sr between plagioclase and silicate melt is assumed after *Blundy and Wood* (1991).

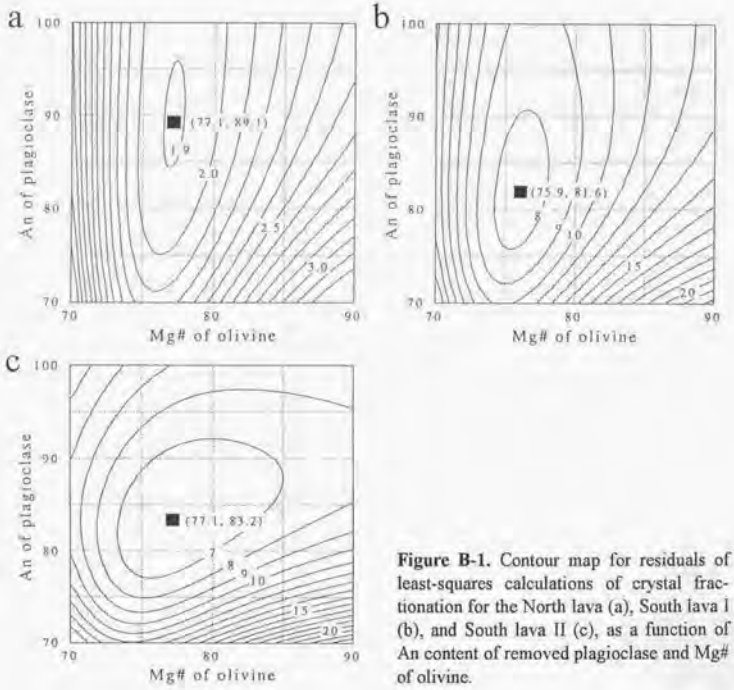

Figure B-1. Contour map for residuals of least-squares calculations of crystal fractionation for the North lava (a), South lava I (b), and South lava II (c), as a function of An content of removed plagioclase and Mg# of olivine.

Mass-balance equations of 12 elements can be written by using the above relations. The standard deviations of the parent magma composition (Table 2-6) are larger than the analytical errors of XRF analysis in all elements, suggesting that the variance of the five averaged data reflects the actual heterogeneity of magmas in addition to the analytical errors. Therefore, the mass-balance equations of individual elements were weighted by dividing by the standard deviations of the parent magma composition. Five unknown parameters, Mg# of olivine, An content of

plagioclase, weight fractions of olivine, plagioclase, and augite are estimated by the following method. At given $Mg\#^{ol}$ and An, linear least-squares calculations were performed by the method of *Bryan et al.* (1969). Then, χ^2 surface was displayed in $Mg\#^{ol}$-An space, and the values of An and Mg# which minimize the error were adopted as estimations (Fig. B-1). Weight fractions of mineral phases are determined uniquely when the An and Mg# are determined. Errors for the estimated parameters are obtained from covariance matrix calculated by curvature matrix of the χ^2 surface. The residual contours for the North lava (Fig. B-1a) are elongated to the ordinate direction, indicating that the Mg# of olivine is successfully estimated, independent of larger uncertainty of the An content. The slope of the contours is gentle in the South lava (Figs. B-1b and B-1c), indicating that the estimated values have relatively large uncertainties. The value of probability Q, which is a quantitative measure for the goodness-of-fit, is 0.967 for the modeling of the North lava (Table 2-7), suggesting fairly successful estimation. That of the South lava I and South lava II is somewhat smaller (Table 2-7).

Acknowledgments

This work was completed during my stay at the Institute for Study of the Earth's Interior, Okayama University at Misasa. I am deeply grateful to Kazuhito Ozawa, Hiroko Nagahara, and Eizo Nakamura for scientific guidance, constructive discussions, and encouragements. I would like to thank Ikuo Kushiro, Hiroaki Sato, Michael J. Walter, Hikaru Iwamori, Shigeru Yamashita, Ryoji Tanaka, and Hideaki Miyamoto for much support and useful discussions.

I would like to express my thanks to Akio Makishima, Takuya Moriguti, Katsura Kobayashi, and Tetsuya Yokoyama for their scientific advice and discussion. I am indebted to Hiroyuki Takei, Chie Sakaguchi, and Tomohiro Usui for useful suggestion and encouragement. Nobuko Takeuchi is also thanked for much technical support and encouragement. I am also grateful to Dean C. Presnall, David H. Green, Eiichi Takahashi, Setsuya Nakada, Takehiro Koyaguchi, Michihiko Nakamura, and Toru Sugawara for useful discussions. I thank Yoshihiro Ishizuka for helpful advice and discussions on Rishiri Volcano. I am thankful to Hideto Yoshida for EPMA analysis at the Geological Institute, University of Tokyo.

I am indebted to Stephen R. Tait and anonymous reviewers of *Journal of Petrology* [*Kuritani*, 1998], Charles R. Bacon, James G. Brophy, and Bruce D. Marsh, reviewers of *Journal of Volcanology and Geothermal Research* [*Kuritani*, 1999a], anonymous reviewers of *Geophysical Research Letters* [*Kuritani*, 1999b], and Randall T. Cygan, John Eichelberger, and Roger Nielsen, reviewers of *Journal of Geophysical Research* [*Kuritani*, 1999c], for valuable and constructive comments to improving my papers. This work was supported by the Japanese Society for the Promotion of Sciences for Japan Junior Scientists.

References

Abe, A., 1934. Geologic report of Rishiri Volcano, Kitami distinct, Hokkaido. *Graduated Thesis of Hokkaido University* (Manuscript, in Japanese).

Albarède, F., 1992. How deep do common basaltic magmas form and differentiate? *Journal of Geophysical Research* 97, 10,997-11,009.

Anderson, A. T., 1984. Probable relations between plagioclase zoning and magma dynamics, Fuego Volcano, Guatemala. *American Mineralogist* 69, 660-676.

Aoki, K., 1971. Petrology of mafic inclusions from Itinome-gata, Japan. *Contributions to Mineralogy and Petrology* 30, 314-331.

Arculus, R. J. and Wills, K. J. A., 1980. The petrology of plutonic blocks and inclusions from the Lesser Antilles island arc. *Journal of Petrology* 21, 743-799.

Bacon, C. R. and Druitt, T. H., 1988. Compositional evolution of the zoned calcalkaline magma chamber of Mt. Mazama, Crater Lake, Oregon. *Contributions to Mineralogy and Petrology* 98, 224-256.

Bartels, K. S., Kinzler, R. J. and Grove, T. L., 1991. High pressure phase relations of primitive high-alumina basalts from Medicine Lake volcano, northern California. *Contributions to Mineralogy and Petrology* 108, 253-270.

Bau, M., 1991. Rare-earth element mobility during hydrothermal and metamorphic fluid-rock interaction and the significance of the oxidation state of europium. *Chemical Geology* 93, 219-230.

Bea, F., Pereira, M. D. and Stroh, A., 1994. Mineral/leucosome trace-element partitioning in a peraluminous migmatite (a laser ablation-ICP-MS study). *Chemical Geology* 117, 291-312.

Bence, A. E. and Albee, A. L., 1968. Empirical correction factors for the electron microanalysis of silicates and oxides. *Journal of Geology* 76, 382-403.

Berman, R. G., 1988. Internally-consistent thermodynamic data for minerals in system Na_2O-K_2O-CaO-MgO-FeO-Fe_2O_3-Al_2O_3-SiO_2-TiO_2-H_2O-CO_2. *Journal of Petrology* 29, 445-522.

Bindeman, I. N., Davis, A. M. and Drake, M. J., 1998, Ion microprobe study of plagioclase-basalt partition experiments at natural concentration levels of trace elements. *Geochimica et Cosmochimica Acta* 62, 1175-1193.

Blundy, J. D. and Wood, B. J., 1991. Crystal-chemical controls on the partitioning of Sr and Ba between plagioclase feldspar, silicate melts, and hydrothermal solutions. *Geochimica et Cosmochimica Acta* 55, 193-209.

Blundy, J. D. and Wood, B. J., 1994. Prediction of crystal-melt partition coefficients from elastic moduli. *Nature* 372, 452-454.

Bottinga, Y. and Weill, D. F., 1972. The viscosity of magmatic silicate liquids: a model for calculation. *American Journal of Science* 272, 438-475.

Brandeis, G. and Jaupart, C., 1986. On the interaction between convection and crystallization in cooling magma chambers. *Earth and Planetary Science Letters* 82, 345-361.

Brandeis, G. and Marsh, B. D., 1989. The convective liquidus in a solidifying magma chamber: a fluid dynamic investigation. *Nature* 329, 613-616.

Brenan, J. M., Shaw, H. F., Ryerson, F. J. and Phinney, D. L., 1995. Experimental determination of trace-element partitioning between pargasite and a synthetic hydrous andesitic melt. *Earth and Planetary Science Letters* 135, 1-11.

Brophy, J. G., 1986. The Cold Bay volcanic center, Aleutian volcanic arc. *Contributions to Mineralogy and Petrology* 93, 368-380.

Brophy, J. G., 1991. Composition gaps, critical crystallinity, and fractional crystallization in oro-

genic (calc-alkaline) magmatic systems. *Contributions to Mineralogy and Petrology* 109, 173-182.

Brophy, J. G., Dorais, M. J., Donnelly-Nolan, J. and Singer, B. S., 1996. Plagioclase zonation styles in hornblende gabbro inclusions from Little Glass Mountain, Medicine Lake volcano, California: implications for fractionation mechanisms and the formation of composition gaps. *Contributions to Mineralogy and Petrology* 126, 121-136.

Bryan, W. B., Finger, L. W. and Chayes, F., 1969. Estimating proportions in petrographic mixing equations by least-squares approximation. *Science* 163, 926-927.

Campbell, I. H., 1978. Some problems with the cumulus theory. *Lithos* 11, 311-323.

Chakraborty, S., 1997. Rates and mechanisms of Fe-Mg interdiffusion in olivine at 980 °-1300 °C. *Journal of Geophysical Research* 102, 12,317-12,331.

Chen, C. F., 1995. Experimental study of convection in a mushy layer during directional solidification. *Journal of Fluid Mechanics* 293, 81-98.

Chen, C. F. and Turner, J. S., 1980. Crystallization in a double-diffusive system. *Journal of Geophysical Research* 85, 2573-2593.

Clark, A. M. and Long, J. V., 1971. The anisotropic diffusion of nickel in olivine. In: *Thomas Graham Memorial Symposium on Diffusion Processes*. Gordon and Breach, London, pp. 511-521.

Corrigan, G. M., 1982. Supercooling and the crystallization of plagioclase, olivine, and clinopyroxene from basaltic magmas. *Mineralogical Magazine* 46, 31-42.

Crawford, A. J., Falloon, T. J. and Eggins, S., 1987. The origin of island arc high-alumina basalts. *Contributions to Mineralogy and Petrology* 97, 417-430.

Davaille, A. and Jaupart, C., 1993a. Thermal convection is lava lakes. *Geophysical Research Letters* 20, 1827-1830.

Davaille, A. and Jaupart, C., 1993b. Transient high-Rayleigh-number thermal convection with large viscosity variations. *Journal of Fluid Mechanics* 253, 141-166.

Deer, W. A., Howie, R. A. and Zussman, J., 1978. Single-Chain Silicates. In: *Rock-Forming Minerals*. Longman Group, London, 668 pp.

de Silva, S. L., 1989. The origin and significance of crystal rich inclusions in pumices from two Chilean ignimbrites. *Geological Magazine* 126, 159-175.

Donaldson, C. H., 1976. An experimental investigation of olivine morphology. *Contributions to Mineralogy and Petrology* 57, 187-213.

Donaldson, C. H., 1979. An experimental investigation of the delay in nucleation of olivine in mafic magmas. *Contributions to Mineralogy and Petrology* 69, 21-32.

Dostal, J., Dupuy, C., Carron, J. P., le Guen de Kerneizan, M. and Maury, R. C., 1983. Partition coefficients of trace elements: application to volcanic rocks of St. Vincent, West Indies. *Geochimica et Cosmochimica Acta* 37, 525-533.

Druitt, T. H. and Bacon, C. R., 1989. Petrology of the zoned calcalkaline magma chamber of Mount Mazama, Crater Lake, Oregon. *Contributions to Mineralogy and Petrology* 101, 245-259.

Dungan, M. A. and Rhodes, J. M., 1978. Residual glasses and melt inclusions in basalts from DSDP Legs 45 and 46: Evidence for magma mixing. *Contributions to Mineralogy and Petrology* 67, 417-431.

Dunn, T. and Sen, C., 1994. Mineral/matrix partition coefficients for orthopyroxene, plagioclase, and olivine in basaltic to andesitic systems: A combined analytical and experimental study. *Geochimica et Cosmochimica Acta* 58, 717-733.

Eichelberger, J. C., 1980. Vesiculation of mafic magma during replenishment of silicic magma reservoirs. *Nature* 288, 446-450.

Eichelberger, J. C., Carrigan, C. R., Westrich, H. R. and Price, R. H., 1986. Non-explosive silicic volcanism. *Nature* 323, 598-602.

Elkins, L. T. and Grove, T. L., 1990. Ternary feldspar experiments and thermodynamic models.

American Mineralogist 75, 544-559.

Ewart, A. and Griffin, W. L., 1994. Application of proton-microprobe data to trace-element partitioning in volcanic rocks. *Chemical Geology* 117, 251-284.

Feeley, T. C. and Dungan, M. A., 1996. Compositional and dynamic controls on mafic-silicic magma interactions at continental arc volcanoes: Evidence from Cordón El Guadal, Tatara-San Pedro complex, Chile. *Journal of Petrology* 37, 1547-1577.

Fram, M. S. and Longhi, J., 1992. Phase equilibria of dikes associated with Proterozoic anorthosite complexes. *American Mineralogist* 77, 605-616.

Fram, M. S. and Lesher, C. E., 1997. Generation and polybaric differentiation of east Greenland early Tertiary flood basalts. *Journal of Petrology* 38, 231-275.

Freundt, A. and Schmincke, H-U., 1992. Mixing of rhyolite, trachyte and basalt magma erupted from a vertically and laterally zoned reservoir, composite flow P1, Gran Canaria. *Contributions to Mineralogy and Petrology* 112, 1-19.

Frey, F. A., 1969. Rare earth abundances in a high-temperature peridotite intrusion. *Geochimica et Cosmochimica Acta* 33, 1429-1447.

Fujimaki, H., 1986. Partition coefficients of Hf, Zr, and REE between zircon, apatite, and liquid. *Contributions to Mineralogy and Petrology* 94, 42-45.

Fujimaki, H. and Tatsumoto, M., 1984. Partition coefficients of Hf, Zr and REE between phenocrysts and groundmass. *Journal of Geophysical Research* 89, B662-B672.

Geschwind, C. H. and Rutherford, M. J., 1995. Crystallization of microlites during magma ascent: the fluid mechanics of 1980-1986 eruptions at Mount St Helens. *Bulletin of Volcanology* 57, 356-370.

Ghiorso, M. S. and Sack, R. O., 1995. Chemical mass transfer in magmatic processes IV. A revised and internally consistent thermodynamic model for the interpolation and extrapolation of liquid-solid equilibria in magmatic systems at elevated temperatures and pressures. *Contributions to Mineralogy and Petrology* 119, 197-212.

Green, T. H. and Pearson, N. J., 1985. Experimental determination of REE partition coefficients between amphibole and basaltic to andesitic liquids at high pressure. *Geochimica et Cosmochimica Acta* 49, 1465-1468.

Green, T. H. and Pearson, N. J., 1987. An experimental study of Nb and Ta partitioning between Ti-rich minerals and silicate liquids at high pressure and temperature. *Geochimica et Cosmochimica Acta* 51, 55-62.

Grove, T. L. and Bryan, W. B., 1983. Fractionation of pyroxene-phyric MORB at low pressure: an experimental study. *Contributions to Mineralogy and Petrology* 84, 293-309.

Grove, T. L., Baker M. B. and Kinzler, R. J., 1984. Coupled CaAl-NaSi diffusion in plagioclase feldspar: Experiments and applications to cooling rate speedometry. *Geochimica et Cosmochimica Acta* 48, 2113-2121.

Grove, T. L., Kinzler, R. J. and Bryan, W. B., 1992. Fractionation of mid-ocean ridge basalt (MORB). In: *Mantle Flow and Melt Generation at Mid-Ocean Ridges*. Morgan, J. P., Blackman, D. K. and Sinton, J. M. (eds.), Geophysical Monograph 71. American Geophysical Union, pp. 281-310.

Hart, S. R. and Dunn, T., 1993. Experimental cpx/melt partitioning of 24 trace elements. *Contributions to Mineralogy and Petrology* 113, 1-8.

Helz, R. T., 1980. Crystallization history of Kilauea Iki lava lake as seen in drill core recovered in 1967-1979. *Bulletin of Volcanology* 43, 675-701.

Helz, R. T. and Thornber, C. R., 1987. Geothermometry of Kilauea Iki lava lake, Hawaii. *Bulletin of Volcanology* 49, 651-668.

Helz, R. T., Kirschenbaum, H. and Marinenko, J. W., 1989. Diapiric transfer of melt in Kilauea Iki lava lake, Hawaii: A quick, efficient process of igneous differentiation. *Geological Society of America Bulletin* 101, 578-594.

Hirose, K. and Kushiro, I., 1993. Partial melting of dry peridotites at high pressures: determina-

tion of compositions of melts segregated from peridotite using aggregates of diamond. *Earth and Planetary Science Letters* 114, 477-489.

Hirschmann, M., 1991. Thermodynamics of multicomponent olivines and the solution properties of $(Ni,Mg,Fe)_2SiO_4$ and $(Ca,Mg,Fe)_2SiO_4$ olivines. *American Mineralogist* 76, 1232-1248.

Holtz, F., Behrens, H., Dingwell, D. B. and Johannes, W., 1995. H_2O solubility in haplogranitic melts: compositional, pressure, and temperature dependence. *American Mineralogist* 80, 94-108.

Hort, M., 1997. Cooling and crystallization in sheet-like magma bodies revisited. *Journal of Volcanology and Geothermal Research* 76, 297-317.

Hort, M., Marsh, B. D., Resmini, R. G. and Smith, M. K., 1999. Convection and crystallization in a liquid cooled from above: an experimental and theoretical study. *Journal of Petrology* 40, 1271-1300.

Housh, T. B. and Luhr, J. F., 1991. Plagioclase-melt equilibria in hydrous systems. *American Mineralogist* 76, 477-492.

Huppert, H. and Sparks, R. S. J., 1988. The generation of granitic magmas by intrusion of basalt into continental crust. *Journal of Petrology* 29, 599-624.

Huppert, H. and Sparks, R. S. J., 1989. Chilled margins in igneous rocks. *Earth and Planetary Science Letters* 92, 397-405.

Huppert, H. and Turner, J. S., 1991. Comments on 'On convective style and vigor in sheet-like magma chambers' by Bruce D. Marsh. *Journal of Petrology* 32, 851-854.

Irving, A. J. and Frey, F. A., 1984. Trace element abundances in megacrysts and their host basalts: constraints on partition coefficients and megacryst genesis. *Geochimica et Cosmochimica Acta* 48, 1201-1221.

Ishikawa, T. and Nakamura, E., 1994. Origin of the slab component in arc lavas from across-arc variation of B and Pb isotopes. *Nature* 370, 205-208.

Ishizuka, Y., 1999. Eruptive history of Rishiri Volcano, Northern Hokkaido, Japan. *Bulletin of the Volcanological Society of Japan* 44, 23-40 (in Japanese).

Ishizuka, Y. and Nakagawa, M., 1994. K-Ar ages of dacitic lava domes of Rishiri Volcano, northern Hokkaido. *Journal of Mineralogy, Petrology, and Economic Geology* 89, 360-364 (in Japanese).

Ishizuka, Y. and Nakagawa, M., 1999. Petrological evolution of Rishiri volcano, northern Hokkaido, Japan. *Journal of Mineralogy, Petrology, and Economic Geology* 94, 279-294 (in Japanese).

Jaupart, C. and Tait, S. R., 1995. Dynamics of differentiation in magma reservoirs. *Journal of Geophysical Research* 100, 17,615-17,636.

Johannes, W. and Holtz, F., 1996. *Petrogenesis and experimental petrology of granitic rocks*. Springer-Verlag, Berlin, 335 p.

Jurewicz, A. J. G. and Watson, E. B., 1988. Cation in olivine, Part 2: diffusion in olivine xenocrysts, with applications to petrology and mineral physics. *Contributions to Mineralogy and Petrology* 99, 186-201.

Kaneko, K. and Koyaguchi, T., 1996. The evolution of the magma system in the crust. Part 5: relationship among temperature, saturation water content, and effective fusion temperature of crustal materials. *Abstract of Fall Meeting of the Volcanological Society of Japan*, p. 30 (in Japanese).

Katsui, Y., 1953. Petro-chemical study on the lavas from Volcano Rishiri, Hokkaido, Japan. *Journal of Faculty of Science, Hokkaido University* 8, 245-258.

Kawamoto, T., 1992. Dusty and honeycomb plagioclase: indicators of processes in the Uchino stratified magma chamber, Izu Peninsula, Japan. *Journal of Volcanology and Geothermal Research* 49, 191-208.

Kawasaki, T. and Ito, E., 1994. An experimental determination of the exchange reaction of Fe^{2+}

and Mg^{2+} between olivine and Ca-rich clinopyroxene. *American Mineralogist* 79, 461-477.

Kerr, R. C., Woods, A. W., Worster, M. G. and Huppert, H. E., 1990a. Solidification of an alloy cooled from above Part 1. Equilibrium growth. *Journal of Fluid Mechanics* 216, 323-342.

Kerr, R. C., Woods, A. W., Worster, M. G. and Huppert, H. E., 1990b. Solidification of an alloy cooled from above. Part 2. Non-equilibrium interfacial kinetics. *Journal of Fluid Mechanics* 217, 331-348.

Kerr, R. C., Woods, A. W., Worster, M. G. and Huppert, H. E., 1990c. Solidification of an alloy cooled from above. Part 3. Compositional stratification within the solid. *Journal of Fluid Mechanics* 218, 337-354.

Kinzler, R. J. and Grove, T. L., 1992. Primary magmas of mid-ocean ridge basalts 1. Experiments and methods. *Journal of Geophysical Research* 97, 6885-6906.

Kirkpatrick, R. J., 1981. Kinetics and crystallization of igneous rocks. *Reviews of Mineralogy* 8, 321-398.

Kobayashi, T., 1987. Geology of Rishiri Volcano. *Journal of Geological Society of Japan* 93, 749-760 (in Japanese).

Kobayashi, T., Yoshida, T., Fukuoka, T. and Aoki, K., 1987. Geochemical research of Rishiri Volcano, Hokkaido. *Research Report of Laboratory of Nuclear Science, Tohoku University* 20, 216-232 (in Japanese).

Kogiso, T., Tatsumi, Y. and Nakano, S., 1997. Trace element transport during dehydration processes in the subducted oceanic crust: 1. Experiments and implications for the ocean of ocean island basalts. *Earth and Planetary Science Letters* 148, 193-205.

Koyaguchi, T., 1986. Evidence for two-stage mixing in magmatic inclusions and rhyolitic lava dome on Niijima island, Japan. *Journal of Volcanology and Geothermal Research* 29, 71-98.

Kuritani, T., 1998. Boundary layer crystallization in a basaltic magma chamber: evidence from Rishiri Volcano, northern Japan. *Journal of Petrology* 39, 1619-1640.

Kuritani, T., 1999a. Phenocryst crystallization during ascent of alkali basalt magma at Rishiri Volcano, northern Japan. *Journal of Volcanology and Geothermal Research* 88, 77-97.

Kuritani, T., 1999b. Thermal and compositional evolution of a cooling magma chamber by boundary layer fractionation: model and its application for primary magma estimation. *Geophysical Research Letters* 26, 2029-2032.

Kuritani, T., 1999c. Boundary layer fractionation constrained by differential information from the Kutsugata lava flow, Rishiri Volcano, Japan. *Journal of Geophysical Research* 104, 29,401-29,417.

Kushiro, I., 1994. Analysis of major and minor elements in silicate rocks with X-ray fluorescence. In: *Evolution of the Crust in Island Arcs*. Grant report for the Ministry of Education of Japan, pp. 1-22 (in Japanese).

Lange, R. L. and Carmichael, I. S. E., 1990. Thermodynamic properties of silicate liquids with emphasis on density, thermal expansion and compressibility. In: *Modern methods of igneous petrology: understanding magmatic processes*. Nicholls, J. and Russell, J. K. (eds.), pp. 25-64, Mineralogical Society of America, Washington, D. C..

Langmuir, C. H., 1989. Geochemical consequences of in situ crystallization. *Nature* 340, 199-205.

Lemarchand, F., Benoit, V. and Calais, G., 1987. Trace element distribution coefficients in alkaline series. *Geochimica et Cosmochimica Acta* 51, 1071-1081.

L'Heureux, I. and Fowler, A. D. 1994. A nonlinear dynamical model of oscillatory zoning in plagioclase. *American Mineralogist* 79, 885-891.

Lindsley, D. H., 1983. Pyroxene thermometry. *American Mineralogist* 68, 477-493.

Lipman, P. W., Banks, N. G. and Rhodes, J. M., 1985. Degassing-induced crystallization of ba-

saltic magma and effects on lava rheology. *Nature* 317, 604-607.

Lofgren, G. E., 1974. An experimental study of plagioclase crystal morphology: isothermal crystallization. *American Mineralogist* 59, 127-138.

Lofgren, G. E., 1980. Experimental studies on the dynamic crystallization of silicate melts. In: *Physics of Magmatic Processes*. Hargraves, R. B. (ed.), Princeton University Press, Princeton, NJ, pp. 487-551.

Luhr, J. F. and Carmichael, I. S. E., 1980. The Colima Volcanic Complex, Mexico I. Post-caldera andesites from Volcan Colima. *Contributions to Mineralogy and Petrology* 71, 343-372.

Luhr, J. F., Carmichael, I. S. E. and Varekamp, J. C., 1984. The 1982 eruptions of El Chichon Volcano, Chiapas, Mexico: mineralogy and petrology of the anhydrite-bearing pumices. *Journal of Volcanology and Geothermal Research* 23, 69-108.

Mahood, G. A. and Baker, D. R., 1986. Experimental constraints on depths of fractionation of mildly alkalic basalts and associated felsic rocks: Pantelleria, Strait of Sicily. *Contributions to Mineralogy and Petrology* 93, 251-264.

Mahood, G. A. and Stimac, J. A., 1990. Trace-element partitioning in pantellerites and trachytes. *Geochimica et Cosmochimica Acta* 54, 2257-2276.

Makishima, A. and Nakamura, E., 1997. Suppression of matrix effects in ICP-MS by high power operation of ICP: Application to precise determination of Rb, Sr, Y, Cs, Ba, REE, Pb, Th and U at ng g^{-1} levels in milligram silicate samples. *Geostandards Newsletter* 21, 307-319.

Makishima, A., Nakamura, E. and Nakano, T., 1997. Determination of boron in silicate samples by direct aspiration of sample HF solutions into ICP-MS. *Analytical Chemistry* 69, 3754-3759.

Makishima, A., Nakamura, E. and Nakano, T., 1999. Determination of zirconium, niobium, hafnium and tantalum at ng g-1 levels in geological materials by direct nebulation of sample HF solution into FI-ICP-MS. *Geostandards Newsletter* 23, 7-20.

Mangan, M. T. and Marsh, B. D., 1992. Solidification front fractionation in phenocryst-free sheet-like magma bodies. *Journal of Geology* 100, 605-620.

Marsh, B. D., 1988. Crystal capture, sorting, and retention in convecting magma. *Geological Society of America Bulletin* 100, 1720-1737.

Marsh, B. D., 1989. On the convective style and vigor in sheet-like magma chambers. *Journal of Petrology* 30, 479-530.

Marsh, B. D., 1991. Reply. *Journal of Petrology* 32, 855-860.

Marsh, B. D., 1996. Solidification fronts and magmatic evolution. *Mineralogical Magazine* 60, 5-40.

Marsh, B. D. and Maxey, M. R., 1985. On the distribution and separation of crystals in convecting magma. *Journal of Volcanology and Geothermal Research* 24, 95-150.

Martin, D. and Nokes, R., 1989. A fluid-dynamical study of crystal settling in convecting magmas. *Journal of Petrology* 30, 1471-1500.

Matsui, K., Issiki, N., Hata, M., Yamaguchi, S., Yoshii, M., Ono, K., Satoh, H. and Sawamura, K., 1967. *Explanatory text of the geological map of Japan, Rishirito*, scale 1:50000. Hokkaido development agency (in Japanese).

McBirney, A. R., 1995. Mechanisms of differentiation in the Skaergaard Intrusion. *Journal of Geological Society of London* 152, 421-435.

McBirney, A. R. and Noyes, R. M., 1979. Crystallization and layering of the Skaergaard Intrusion. *Journal of Petrology* 20, 487-554.

McBirney, A. R., Baker, B. H. and Nilson, R. H., 1985. Liquid fractionation. Part I: Basic principles and experimental simulations. *Journal of Volcanology and Geothermal Research* 24, 1-24.

McKenzie, D. and O'Nions, R. K., 1991. Partial melt distributions from inversion of rare earth

element concentrations. *Journal of Petrology* 32, 1021-1091.

Misener, D. J., 1974. Cationic diffusion in olivine to 1400 °C and 35 kbar. In: *Geochemical Transport and Kinetics*. Hofmann, A. W., Giletti, B. J., Yorder, H. S. Jr. and Yund, R. A. (eds.), Carnegie Inst., Washington, vol. 634, 117-129.

Miura, H. and Takaoka, S., 1993. Significance of the radiocarbon age and the identification of the fossil wood under lava flows erupted from Rishiri Volcano, Hokkaido, Japan. *Quaternary Research* 32, 107-114 (in Japanese).

Moore, G., Righter, K. and Carmichael, I. S. E., 1995. The effect of dissolved water on the oxidation state of iron in natural silicate liquids. *Contributions to Mineralogy and Petrology* 120, 170-179.

Moore, G., Vennemann, T. and Carmichael, I. S. E., 1998. An empirical model for the solubility of H_2O in magmas to 3 kilobars. *American Mineralogist* 83, 36-42.

Moriguti, T. and Nakamura, E., 1998. Across-arc variation of Li isotopes in lavas and implications for crust/mantle recycling at subdiction zones. *Earth and Planetary Science Letters* 163, 167-174.

Nakamura, M. and Shimakita, S., 1998. Dissolution origin and syn-entrapment compositional change of melt inclusion in plagioclase. *Earth and Planetary Science Letters* 161, 119-133.

Nakamura, Y. and Kushiro, I., 1970. Compositional relations of coexisting orthopyroxene, pigeonite and augite in a tholeiitic andesite from Hakone volcano. *Contributions to Mineralogy and Petrology* 26, 265-275.

Naney, M. T., 1983. Phase equilibria of rock-forming feromagnesian silicates in granitic systems. *American Journal of Science* 283, 993-1033.

Nash, W. P. and Crecraft, H. R., 1985. Partition coefficients for trace elements in silicic magmas. *Geochimica et Cosmochimica Acta* 49, 2309-2322.

Nielsen, R. L., 1988. A model for the simulation of combined major and trace element liquid lines of descent. *Geochimica et Cosmochimica Acta* 52, 27-38.

Nielsen, R. L. and Delong, S. E., 1992. A numerical approach to boundary layer fractionation: application to differentiation in natural magma systems. *Contributions to Mineralogy and Petrology* 110, 355-369.

Nielsen, R. L., Gallahan, W. E. and Newberger, F., 1992. Experimentally determined mineral-melt partition coefficients for Sc, Y and REE for olivine, orthopyroxene, pigeonite, magnetite and ilmenite. *Contributions to Mineralogy and Petrology* 110, 488-499.

O'Hara, M. J. and Fry, N., 1996. Geochemical effects of small packet crystallization in large magma chambers –Further resolution of the highly compatible element paradox. *Journal of Petrology* 37, 891-925.

Ozawa, K., Meyer, P. S. and Bloomer, S. H., 1991. Mineralogy and textures of iron-titanium oxide gabbros and associated olivine gabbros from Hole 735B. *Proceedings of the Ocean Drilling Program, Scientific Results* 118, 41-73.

Pallister, J. S., Hoblitt, R. P. and Reyes, A. G., 1992. A basalt trigger for the 1991 eruptions of Pinatubo volcano? *Nature* 356, 426-428.

Panjasawatwong, Y., Danyushevsky, L. V., Crawford, A. J. and Harris, K. L., 1995. An experimental study of the effects of melt composition on plagioclase-melt equilibria at 5 and 10 kbar: implications for the origin of magmatic high-An plagioclase. *Contributions to Mineralogy and Petrology* 118, 420-432.

Paster, T. P, Schauwecher, D. S. and Haskin, L. A., 1974. The behavior of some trace elements during solidification of the Skaergaard layered series. *Geochimica et Cosmochimica Acta* 38, 1549-1577.

Pearce, T. H. and Kolisnik, A. M., 1990. Observations of plagioclase zoning using interference imaging. *Earth-Science Reviews* 29, 9-26.

Philpotts, A. R., 1990. *Principle of Igneous and Metamorphic Petrology*. Prentice Hall, New

Jersey, 498 pp.

Philpotts, A. R., Caroll, M. and Hill, J. M., 1996. Crystal-mush compaction and the origin of pegmatitic segregation sheets in a thick flood-basalt flow in the Mesozoic Hartford Basin, Connecticut. *Journal of Petrology* 37, 811-836.

Phinney, W. C., 1992. Partition coefficients for iron between plagioclase and basalt as a function of oxygen fugacity: Implications for Archean and lunar anorthosites. *Geochimica et Cosmochimica Acta* 56, 1885-1895.

Press, W. H., Teukolsky, S. A., Vetterling, W. T. and Flannery, B. P., 1992. *Numerical Recipes in C, The Art of Scientific Computing*, second ed, Cambridge Univ. Press, Cambridge.

Puffer, J. H. and Horter, D. L., 1993. Origin of pegmatitic segregation veins within flood basalts. *Geological Society of America Bulletin* 96, 1131-1139.

Roeder, P. L. and Emslie, R. F., 1970. Olivine-liquid equilibrium. *Contributions to Mineralogy and Petrology* 29, 275-289.

Sack, R. O., Carmichael, I. S. E., Rivers, M. and Ghiorso, M. S., 1980. Ferric-ferrous equilibria in natural silicate liquids at 1 bar. *Contributions to Mineralogy and Petrology* 75, 369-376.

Sack, R. O., Walker, D. and Carmichael, I. S. E., 1987. Experimental petrology of alkalic lavas: constraints on cotectics of multiple saturation in natural basic liquids. *Contributions to Mineralogy and Petrology* 96, 1-23.

Sack, R. O. and Ghiorso, M. S., 1994a. Thermodynamics of multicomponent pyroxenes: I. Formulation of a general model. *Contributions to Mineralogy and Petrology* 116, 277-286.

Sack, R. O. and Ghiorso, M. S., 1994b. Thermodynamics of multicomponent pyroxenes: III. Calibration of $Fe^{2+}(Mg)_{-1}$, $TiAl_2(MgSi_2)_{-1}$, $TiFe^{3+}_2(MgSi_2)_{-1}$, $AlFe^{3+}(MgSi)_{-1}$, $NaAl(CaMg)_{-1}$, $Al_2(MgSi)_{-1}$ and $Ca(Mg)_{-1}$ exchange reactions between pyroxenes and silicate melts. *Contributions to Mineralogy and Petrology* 118, 271-296.

Sakuyama, M. and Kushiro, I., 1979. Vesiculation of hydrous andesitic melt and transport of alkalies by separated vapor phase. *Contributions to Mineralogy and Petrology* 71, 61-66.

Sato, H., 1989. Mg-Fe partitioning between plagioclase and liquids in basalts of Hole 504B, ODP Leg 111: a study of melting at 1 atm. *Proceedings of the Ocean Drilling Program, Scientific Results* 111, 17-26.

Sato, H., 1995. Textural difference between pahoehoe and aa lavas of Izu-Oshima volcano, Japan - an experimental study on population density of plagioclase. *Journal of Volcanology and Geothermal Research* 66, 101-113.

Schnetzler, C. C. and Philpotts, J. A., 1970. Partition coefficients of rare earth elements between igneous matrix material and rock-forming mineral phenocrysts - II. *Geochimica et Cosmochimica Acta* 34, 331-340.

Shaw, H. R., 1972. Viscosities of magmatic silicate liquids: an empirical method of prediction. *American Journal of Science* 272, 870-893.

Shibata, T. and Nakamura, E., 1997. Across-arc variations of isotope and trace element compositions from Quaternary basaltic volcanic rocks in northeastern Japan: implications for interaction between subducted oceanic slab and mantle wedge. *Journal of Geophysical Research* 102, 8051-8064.

Shibata, T., Makishima, A. and Nakamura, E., 1989. Trace neodymium isotope analysis and its application to geological problems. *Abstract of Annual Meeting of the Geochemical Society of Japan*, p.73, Tokyo, Japan (in Japanese).

Shirley, D. N., 1987. Differentiation and compaction in the Palisades Sill, New Jersey. *Journal of Petrology* 28, 835-865.

Singer, B. S., Pearce, T. H., Kolisnik, A. M. and Myers, J. D., 1993. Plagioclase zoning in mid-Pleistocene lavas from Seguam volcanic center, central Aleutian arc, Alaska. *American Mineralogist* 78, 143-157.

Sisson, T. W., 1994. Hornblende-melt trace-element partitioning measured by ion microprobe. *Chemical Geology* 117, 331-344.

Sisson, T. W. and Grove, T. L., 1993. Experimental investigations of the role of H_2O in calc-alkaline differentiation and subduction zone magmatism. *Contributions to Mineralogy and Petrology* 113, 143-166.

Skulski, T., Minarik, W. and Watson, E. B., 1994. High-pressure experimental trace-element partitioning between clinopyroxene and basaltic melts. *Chemical Geology* 117, 127-147.

Smith, R. K. and Lofgren, G. E., 1983. An analytical and experimental study of zoning in plagioclase. *Lithos* 16, 153-168.

Snyder, D. and Tait, S., 1996. Magma mixing by convective entrainment. *Nature* 379, 529-531.

Sparks, R. S. J., Sigurdsson, H. and Wilson, L., 1977. Magma mixing: a mechanism for triggering acid explosive eruptions. *Nature* 267, 315-318.

Stix, J. and Gorton, M. P., 1990. Variations in trace element partition coefficients in sanidine in the Cerro Toledo Rhyolite, Jemez Mountains, New Mexico: Effects of composition, temperature and volatiles. *Geochimica et Cosmochimica Acta* 54, 2697-2708.

Sun, S.–S. and McDonough, W. F., 1989. Chemical and isotopic systematics of oceanic basalts: implications for mantle composition and processes. In: *Magmatism in the Ocean Basins*. Saunders. A. D. and Norry, M. J. (eds.), Geological Society Special Publications 42, 313-345.

Tait, S. R., 1988. Samples from the crystallizing boundary layer of a zoned magma chamber. *Contributions to Mineralogy and Petrology* 100, 470-483.

Tait, S. R. and Jaupart, C., 1992. Compositional convection in a reactive crystalline mush and melt differentiation. *Journal of Geophysical Research* 97, 6735-6756.

Tait, S. R. and Jaupart, C., 1996. The production of chemically stratified and adcumulate plutonic igneous rocks. *Mineralogical Magazine* 60, 99-114.

Tatsumi, Y., Sakuyama, M., Fukuyama, H. and Kushiro, I., 1983. Generation of arc basalt magmas and thermal structure of the mantle wedge in subduction zones. *Journal of Geophysical Research* 88, 5815-1825.

Tatsumi, Y., Hamilton, D. L. and Nesbitt, R. W., 1986. Chemical characteristics of fluid phase related from a subducted lithosphere and origin of arc magmas: evidence from high-pressure experiments and natural rocks. *Journal of Volcanology and Geothermal Research* 29, 293-309.

Thy, P., 1991. High and low pressure phase equilibria of a mildly alkalic lava from the 1965 Surtsey eruption: Experimental results. *Lithos* 26, 223-243.

Tsuchiyama, A., 1985. Dissolution kinetics of plagioclase in the melt of the system diopside-albite-anorthite, and origin of dusty plagioclase in andesites. *Contributions to Mineralogy and Petrology* 89, 1-16.

Turner, J. S., 1979. *Buoyancy Effects in Fluids*. Cambridge University Press.

Turner, J. S., 1980. A fluid-dynamical model of differentiation and layering in magma chambers. *Nature* 285, 213-215.

Turner, J. S., Huppert, H. E. and Sparks, R. S. J., 1986. Komatiites II: Experimental and theoretical investigations of post-emplacement cooling and crystallization. *Journal of Petrology* 27, 397-437.

Villemant, B., 1988. Trace element evolution in the Plegrean Fields, Central Italy: fractional crystallization and selective enrichment. *Contributions to Mineralogy and Petrology* 98, 169-183.

Watson, E. B. and Green, T. H., 1981. Apatite/liquid partition coefficients for the rare earth elements and strontium. *Earth and Planetary Science Letters* 56, 405-421.

Watts, R. B., de Silva, S. L., Jimenez de Rios, G. and Croudace, I., 1999. Effusive eruption of viscous silicic magma triggered and driven by recharge: a case study of the Cerro Chascon-Runtu Jarita dome complex in southwest Bolivia. *Bulletin of Volcanology* 60,

241-264.

Worster, M. G., Huppert, H. E. and Sparks, R. S. J., 1990. Convection and crystallization in magma cooled from above. *Earth and Planetary Science Letters* 101, 78-89.

Worster, M. G., Huppert, H. E. and Sparks, R. S. J., 1993. The crystallization of lava lakes. *Journal of Geophysical Research* 98, 15,891-15,901.

Yamashita, S., 1999. Experimental study of the effect of temperature on water solubility in natural rhyolite melt to 100 MPa. *Journal of Petrology* 40, 1497-1507.

Yoshida, T., Yamaguchi, T. and Kawasaki, Y., 1981. Internal structure of Kutsugata lava flow, Rishiri Volcano. *Journal of Japanese Association of Mineralogists, Petrologists and Economic Geologists* 76, 181-194 (in Japanese).

Yoshikawa, M. and Nakamura, E., 1993. Precise isotope determination of trace amounts of Sr in magnesium-rich samples. *Journal of Mineralogy, Petrology, and Economic Geology* 88, 548-561 (in Japanese).

Yoshikawa, M. and Nakamura, E., Geochemical evolution of the Horoman peridotite complex: implications for melt extraction, metasomatism and compositional layering in the mantle. *Journal of Geophysical Research*, in press.

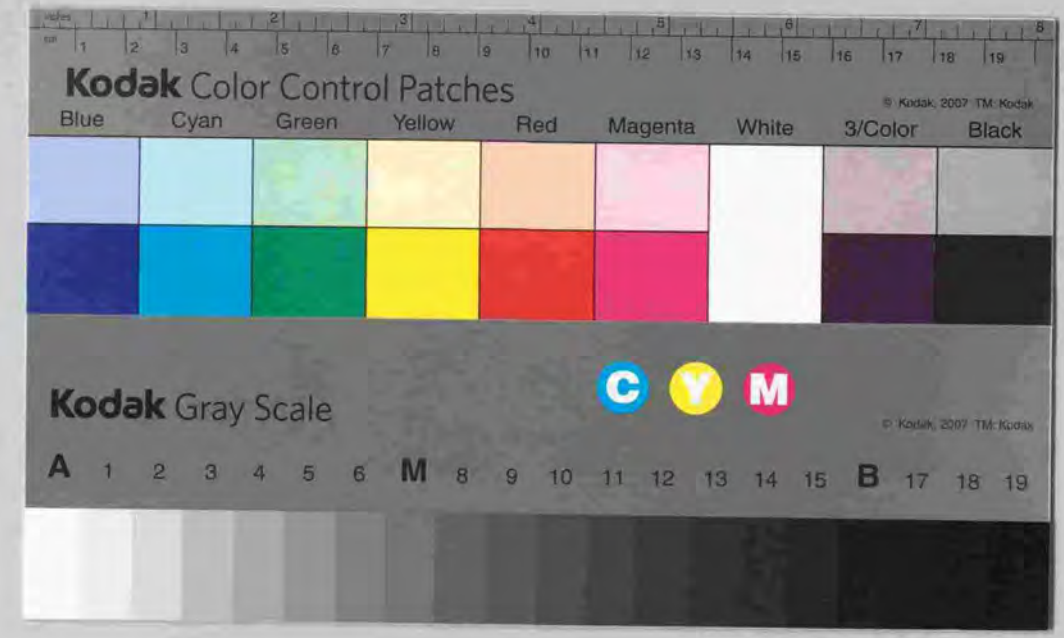
Kodak Color Control Patches
© Kodak, 2007 TM: Kodak
Blue
Cyan
Green
Yellow
Red
Magenta
White
3/Color
Black
Kodak Gray Scale
C
Y
M
© Kodak, 2007 TM: Kodak
A 1 2 3 4 5 6 M 8 9 10 11 12 13 14 15 B 17 18 19